PROBING ISOLATED ICE
AND
GAS-PHASE CHEMISTRY
IN
ASTROPHYSICAL ENVIRONMENTS

Andrew Michael Burkhardt
Novi, Michigan

M.S. Astronomy
University of Virginia, 2015

B.S. Astronomy and Astrophysics with Honors, Physics
University of Michigan, 2013

A Dissertation Presented to the Graduate Faculty of the

University of Virginia

in Candidacy for the Degree of

Doctor of Philosophy

Department of Astronomy
University of Virginia
May 2018

Abstract

With the advent of modern astrophysical observatories such as the Atacama Large Millimeter/submillimeter Array (ALMA), the Karl J. Jansky Very Large Array (VLA), and the Robert C. Byrd Green Bank Telescope (GBT), the field of astrochemistry is now capable of probing into the heart of many of the most chemically-rich and complex astrophysical sources, such as massive star forming regions, protoplanetary disks, and evolved stars. However, as new sensitivities and spatial resolutions are achieved, the synthesis of many competing physical and chemical processes across the dynamic history of these sources make it difficult to disentangle the underlying chemistry. It is a worthwhile endeavor, then, to study the earlier stages of star formation where many of these processes, instead, occur in relative isolation. Here, we perform two experiments to probe the gas-phase and solid-phase chemistry in prototypical environments.

To start, we examine how carbon-chain gas-phase chemistry evolves in isolation within the dark cloud Taurus Molecular Cloud (TMC-1). Here, we performed a deep spectral survey of TMC-1 with the GBT across 1.8 GHz of bandwidth between 18 and 24 GHz to find new, exotic carbon-chain molecules. First, we report the detection of 7 new isotopologues of the large cyanopolyynes, HC_5N and HC_7N, and, by comparing the relative isotopic ratios, conclude that cyanopolyynes may not have a consistent formation route across the molecular family. Next, we discuss the first radio detection of an aromatic molecule, benzonitrile (c-C_6H_5CN), which may prove to both be a key proxy for benzene and a crucial chemical link between small carbon chain and the ubiquitous polycyclic aromatic hydrocarbons (PAHs). Finally, we describe the detection of HC_5O and the tentative detection of HC_7O, whose previously undiscovered molecular family appears to have a formation chemistry that varies significantly from the cyanopolyynes.

In the second half of this manuscript, we study how shocks can impact the chemistry in astrophysical environments and be used as a probe for the relatively unconstrained interstellar solid-phase chemical reservoir. First, we discuss the results from interferometric observations of key shock tracing molecules within the prototypical chemically-active outflow, L1157. Here, we find that shocks affect the abundance of molecules by either primarily sputtering ice-produced species into the gas phase, inducing post-shock gas-phase chemistry, or disrupting the abundance of gas-phase species through the extreme physical conditions in shocks. Second, we reproduce the majority of the predictions made from these observations by adapting the three-phase gas-grain chemical network model, textscnautilus, to include relevant shock physical conditions and processes. Furthermore, this model can make relevant, testable predictions on the temporal evolution of numerous shock-relevant molecules in molecular outflows. And so, with work presented here, we have shown that the underlying chemistry in the interstellar medium can be efficiently and effectively constrained by studying relatively simple and isolated astrophysical environments in great detail.

To Christina

Committee Members:

Anthony J. Remijan
Eric Herbst
Zhi-Yun Li
Robert E. Johnson

Acknowledgements

One question that I have been asked countless times is how I ended up getting interested in the field of astronomy. While many people can point to a specific event or class, the type of science associated with space has fascinated me for as long as I can remember. But, if I were a betting person, I would put my wager on my Grandpa, Bob Malarkey, who babysat my cousin, Kyle, my brother, Adam, and me for the first five years of our lives. Spending his career traveling across the country to build the first room-sized computers for companies and government organizations, he was my first exposure to someone with that curiosity of how the world works that comes with a technical mindset. And as he passed away on the day of my first talk at a scientific conference, I truly wish I could share with him all the amazing things I have come to learn about the universe since then. And so to him, I offer my first gratitude.

I would like to next thank my family, who have always been some of my greatest supporters throughout my many stages of academic endeavors. To Amie, I would like to thank you for enough love and compassion to fuel a small town. To Jeff, as you have been a staple in our family for so long now, I would like to thank you for inspiring confidence in a young, scrawny, awkward, nerdy, little kid by being so invested in my well-being. I would like to thank my brother Adam who, from Diddy Kong Racers to auditorium techies to college roommates, has shown me a strength and persistence that I am constantly in awe of. While always very supportive for all of my extracurricular activities, I would like to especially thank my dad, Greg, for solidifying my passion for looking up to the skies with our trips down to Cape Canaveral and late nights at home trying to spot the ISS flyby overhead. And to my mom, Lori, who has been my greatest cheerleader, I would like to thank you for the countless late nights you were forced to stay up late as your ten years old kept trying to ask just one more question: "But what if..."

In addition, I would also like to thank Nathan, Ryan, and Ben for being such wonderful friends since our early days in middle school. It has been amazing to see how far you have all come into your own, from a world-famous ant blogger to Google programmer turned full-time climate-change fighter to someone who I can only assume will take up the mantle of Falcon after Sam Wilson becomes Captain America. It's been inspiring to see how cool you all actually are.

While astronomy has always been something I was interested in, my passion for the molecular side of the world struck me by surprise upon taking three semesters of general and AP chemistry with the illustrious "Dancin' Jimmy Hanson," whose one-of-kind lectures and self-motivation driven classes have been some of the most fruitful courses I have ever taken.

When I entered my undergraduate career at Michigan, I knew I wanted to do astronomy, but what type of research beyond that was unclear. I was allowed opportunities to experience a variety of research projects but challenged to find something I could spend potentially the rest of my life working on. To the advisors of these first research projects, N-body simulations of the formation of populations of galaxies with Professor Gus Evrard and Dr. Elena Rasia, X-Ray emission from black holes with Professor Elena Gallo, and the optical detection and characterization of orbital debris with Professor Patrick Seitzer, I thank you for giving me exposure to such a wide range of skills and expertise. In particular, I would like to thank Pat for taking me on my first observational trip, which solidified my enthusiasm for collecting actual of photons. However, it wasn't until I began working with Professor Ted Bergin on astrochemistry towards the end of my junior year where I saw the stars align. To Ted, I want to thank you for support, guidance, and patience even up to today when we meet at conferences (or my job interviews!). The way you conduct your research and strive to improve the community around you is something I have attempted to emulate to this day. I would also like to thank Dr. Justin Neil and Dr. Ruud Visser for their research mentoring on my projects with Ted. While at Michigan, I have several compadrés among the Student Astronomical Society, where cloudy skies would often turn Public Nights into board games parties. In particular, I would like to thank Mary, Andrew, Aaron, Nico, Evan, and Matt B. for getting me through all the late nights of homework.

Upon my arrival to Charlottesville just under five years ago, I was rapidly inundated with TA duties, courses, and Defense Against the Dark Arts (i.e. learning interferometry black magic) for the first couple years of my graduate career. And as such, it would be criminal to not thank my fellow astronomy graduate students whom without I would certainly not have survived. In particular, I would like to thank Sandabillion, Son, The Reverend Dr. Patrick King Esquire III, Brain, AM, PM, L-Bitts, Treymond, BDN, and the Pauli Exclusion Principle for making the journey enjoyable and a lot less lonely.

In terms of research at UVa, I was quickly ~~drafted~~ recruited by Dr. Anthony "Tony" Remijan to join his motley crew of observational astrochemists. While widespread and stochastic, at times, I would like to thank the Kingdom of Remijanistan for assisting in the fight against non-rigorous detections, namely Ryan, Joanna, Klaus, Tom, Brandon, and Ceci. I would like to especially thank Dr. Chris Shingledecker for trying his hardest spread the gospel of Fortran and Julia to me and without whom the entire last chapter of this thesis would not have been possible. You are the kind of person that I brag to others that I have the pleasure of knowing you. To Dr. Brett McGuire, I would like to thank for teaching me, among so much else, to not let perfect get in the way of good enough and for being a constant source of inspiration and sounding board of ideas. And to Tony, I would like to thank for the incredible mentoring the past few years. You have taught me to be bold in my claims, but not to take anything scientifically for granted without being able to back it up. It has been a great constant reminder to know that you were willing to go at-bat for me since day one.

While much of my research has focused on observational work, I was lucky enough to be offered to spend time working with Professor Eric Herbst's theoretical astrochemistry

group for a portion of my graduate career. I would like to thank the many past and present members of the Herbst group for welcoming an astronomer into your circle and helping me learn the ropes from you all, including Romane, Ugo, Kinsuk, Ilsa, Jessica, Alec, Nico, and Sean. In particular, Eric himself deserves particular thanks for reaching out to me at the end of my second year and being an excellent source of wisdom and expertise over the years. I would also like to take this time to thank the other two members of my committee Zhi-Yun Li and Bob Johnson for helping me cross the finish line.

Bringing this back home, I would be remiss not to mention the immense help I received from my cat, Saturn. Since we got her a few weeks after moving to Charlottesville, she has been my trusty sidekick during the countless late nights working at home by sleeping in my lap (where she currently is as of this being written).

And finally, I would like to especially thank my wife, Christina. Your love and support has been immeasurable all throughout undergraduate and graduate school. From assuring I took care of myself to watching you become quite the excellent counselor, chef, and crafter to having my best friend constantly at my side, your companionship has made this journey, not just possible, but an amazing experience. As we move on to the next stage of our life in Boston, there is no one else I would rather go on this adventure with.

A. M. Burkhardt

Charlottesville, VA

Contents

List of Figures

List of Tables

Part I

Introduction

Chapter 1

Background & Summary

Many of the biggest scientific questions remaining today relate back to understanding the origins of the world around us: from the Origin of our Universe (58), to the origin of what makes up 95% of the Universe (194), to the origins of life (18; 233). Directly related to this is another outstanding question in astronomy and chemistry: what is the origin of Earth's environment that enabled the formation of life? While significant progress has been made to answer this question, one major step in the formation of life that has yet to be fully understood is how the prebiotic molecules, the building blocks to DNA and RNA, are formed from the elemental ashes produced in the deaths of stars. The initial conditions, or the elemental abundances produced in supernova remnants and stellar atmospheres, can be observationally constrained through observations of diffuse clouds (82). Meanwhile, the discovery of amino acids within comets and meteorites (4; 68), which are thought to be formed out of the primordial material of the solar system, proves that there was a high degree of chemical complexity during the formation of planetary bodies. The field of astrochemistry is vital to answer this question as it seeks to reveal the composition, structure, and dynamics of the molecules that could create and support life and the environments it forms in.

To date, around 200 molecules have been detected in the interstellar medium or circumstellar shells. To study the origin of these species, three major regimes of astrochemistry have arisen:

- Observational: Here, the emission from molecules are detected and, through the study of their abundance and the conditions in which they form, used as probes to determine the underlying chemical and physical processes that produce them.
- Laboratory: Here, analogs to interstellar conditions are created in order to measure the significance of a variety of chemical and physical reactions and processes on the overall chemistry of a astrophysical source. In addition, the spectra of molecules need to be measured in order to be accurately detected in space.
- Theoretical: Here, the experimental constraints acquired by both of these other regimes are combined to attempt to reproduce the data, to the best ability of our chemical and physical understanding to date. Also, where observational and experimental methods are unable to measure a certain value or parameter, theories of physical and quantum chemistry can be used to estimate the likely values.

It is through the synthesis of these three branches of astrochemistry that it is truly possible to unveil the mystery of our molecular origins, as each branch provides new constraints

and insights for one another to exploit. Here, we will focus on the observational and theoretical regimes, while acknowledging the importance of the third, undiscussed branch.

While the first molecules detected in the interstellar medium (ISM) occurred in the 1930's and 1940's (CH (210), CN (163), and CH^+ (65)), the field of astrochemistry first truly exploded with the advent of new field of radio astronomy in the late 1960's and early 1970's with the first detection of polyatomic molecules (e.g. NH_3 (42), H_2O (43), and H_2CO (207)) and the second most abundant molecule in the Universe after H_2 (CO (235)).

Soon after, the first astrochemical models were developed for the purposes of explaining the presence of these new species, as well as predict other molecules that would be promising for future detection (102). Compared to these initial models, which contained $\sim$100 gas-phase reactions and $\sim$35 individual species, modern astrochemical theory has undergone substantial evolution, now containing $\sim 10^4$'s of reactions and $\geq$500 species (77; 155; 199), and the addition of many chemical and physical processes. One of the most important inclusions to these models was the incorporation of chemistry occurring on the surface of or within ice-mantles covering interstellar dust grains (75; 77; 96; 179; 200; 221). For many of the most complex species detected, the production efficiencies of the solid-phase formation routes are significant higher than those in the gas phase (77; 99). However, there is a high degree on uncertainty in the rates and efficiencies among ice-chemistry networks and laboratory studies (56). And as a result, there has been much study to theoretically, observationally, and experimentally determine the significance of ice versus gas-phase chemistry in astrophysical environments (57; 79; 199).

As discussed earlier, to observationally constrain these two regimes of astrochemistry, the spectral signatures from interstellar molecules can be used to identify the presence of specific molecules. Initially, the electronic transitions of molecules, typically found around the visible part of the electromagnetic spectrum, in either emission within interstellar gas or in absorption in stellar atmospheres were used to detect the first molecules. However, the feasibility of this technique is only possible for the smallest of molecules, requires significant external energy input to excite the molecules into these states, and can have a high degree of degeneracy. With the rise of radio receiver technology, it became possible to detect the rotational transitions of molecules in the radio, millimeter, and sub-millimeter regimes. These transitions are highly unique for each species and require the lowest energetic changes between states, which has facilitated the detection of the vast majority of known interstellar molecules through the use of observatories such as the NRAO 140 ft (208), the Karl J. Jansky Very Large Array (VLA) (177), the Robert C. Byrd Green Bank Telescope (GBT) (181), the Atacama Large Millimeter/submillimeter Array (ALMA) (241), the Institut de RadioAstronomie Millimétrique (IRAM) (85), and the NOrthern Extended Millimeter Array (NOEMA) (41; 89), and the Nobeyama Radio Observatory (3). In addition, the ro-vibrational transition of gas-phase molecules have also been studied in much detail in the infrared (20), but is again limited to smaller and more energetically excited molecules.

However, one downside of rotational spectroscopy is it is only able to effectively probe molecules that can freely rotate (i.e. not frozen onto dust grains). Instead, the infrared vibrational transitions of the ices must be observed in absorption behind a bright back-

ground source, commonly unassociated with the targeted molecules. In addition, many of these vibrational transitions are very broad and degenerate with similar species, making the identification of individual species in the ice substantially more difficult than through rotational spectroscopy. As such, the chemical inventory of detected solid-phase interstellar molecules is significantly smaller than its gas-phase counterpart (<20; (27)). This discrepancy, along with the uncertainties in the underlying ice-chemistry within laboratory experiments and astrochemical models, leads to the need for the chemistry to be studied in a wide variety of astrophysical environments with different dominances of gas-phase and ice-mantle chemistry.

The primary source of astrophysical detections of molecules (especially the most complex) has been in regions undergoing active star formation. And furthermore, the observable chemistry dramatically changes throughout prestellar evolution. In the earliest stages, the environment is characterized by a cold ($T \lesssim 10$ K), dense ($n_{\rm H_2} \sim 10^4$ cm^{-3}) relatively quiescent dark clouds known also as prestellar globules or cores (21; 83; 121). The cold temperatures and lack of other significant desorption mechanisms result in the gas-phase chemistry proceeding in relative isolation to the solid-phase chemistry. This means the detected gas-phase species in these sources are dominated by unsaturated molecules, or species whose available carbon valence electrons are not all bonded to atoms so that the chain contains more double and triple carbon-carbon bonds. The classic example of this saturation is the conversion of gas-phase CO to CH_3OH (39), but is seen for many other carbon-chain "backbones" observed towards darks clouds (21; 83; 121).

Eventually, as the material in these dark clouds continue to amass, the gravitational pull of the cloud will overcome the thermal pressure of the gas, resulting in a free-fall collapse of the material. This collapse causes the density and visual extinction to significantly increase until the system becomes pressure balanced again. Upon this stage, the very dense gas ($\gtrsim 10^6$ cm^{-3}) will begin to heat up as it enters the "hot core" or "hot corino" stage (for high and low mass star-forming regions, respectively). During this heat up, many of the species that were locked within the ices on grains are thermally liberated into the gas phase, where they can be observed to enhance the spectra of hot cores with a high degree of chemical complexity (99). In addition, the mobility of molecules on the grain rises and unique surface chemistry can be induced (75). These sources have been found to be some of the most chemically-rich astrophysical sources known and are the source of many of the most complex molecules first detected in the ISM.

As the central core continues to accrete more matter, the pre-stellar core will form into a protostar. In order to conserve angular momentum in this accretion process, much material will be flattened out into a protostellar disk, while a smaller amount will be launched relatively perpendicular to the disk in outflows and jets. These outflows have been seen to display a high degree of chemical complexity (15; 33; 138), due to, in part, the non-thermal desorption of species from the ice due to ejected material shocking into the surrounding nascent cloud. Meanwhile, in these disks, material begins to coalesce and many molecules will begin to freeze back out onto the grains as the high densities in the disk shield the inner parts of the disk from the various destruction processes associated of residing next to a protostar. As the protostar evolves, this disk will evolve into a protoplanetary disk

(PPD), where the seeds of planets and comets form from the ice-rich dust grains deep in the disk. Due to the high optical-depth of these disks and the degree of freeze-out, the discovery of COMs in PPDs has only been achieved recently (232; 246) and further detection of more complex species looks increasingly difficult. However, the chemistry detected does appear to be consistent with cometary studies within our own solar system, which aligns with the theory that comets can be considered chemical time capsules from the initial formation of the solar system (67).

As it clear to see, as one tries to follow the chemistry from the earliest stages to the point just prior to what we can test here in the solar system, the physical and chemical processes become increasingly convolved and complex. While significant studies of the most chemically-rich sources have been very fruitful to understand the formation of the observed molecules (13; 53; 174), the prominence of high degrees of line blending and the current and recent dynamical history of the source can often prevent us from disentangling the competing physico-chemical processes occurring simultaneously. With the already high degree of uncertainty present in many astrochemical models and stellar formation, it begs the question of to what degree the studies can provide us with answers without a better fundamental understanding of the underlying chemistry.

However, one key element here is that we know that the chemical complexity exists far prior to the formation of planets and comets. Or even more so, we know that it is possible to find astrophysical sources that have only a smaller number of these competing processes by looking to the earlier stages of star formation. As such, what will be discussed here are a pair of "experiments" to test some fundamental astrochemical processes that are prevalent in a variety of astrophysical environments by studying the simplest of sources they exist in. Our thesis, here is that: We can constrain the fundamental underlying chemistry by utilizing isolated, simple astrophysical sources as "laboratories."

In the first laboratory, we will seek to understanding the build up of gas-phase carbon chemistry by studying the gas-phase chemistry isolated within dark clouds. Second, we will probe the relatively unconstrained ice-chemistry reservoir in protostellar environments and understanding impacts of astrophysical shocks on the chemical make up of a source through the study of isolated low-mass molecular outflows.

The organization of the rest of this manuscript is as follows: In Part II, we discuss performing a deep spectral survey of the Taurus Molecular Cloud with the Green Bank Telescope in order to constrain carbon-chain chemistry in dark clouds. Within here, we discuss the detection of isotopologues of HC_5N and HC_7N, the first aromatic molecule discovered with radio astronomy - benzonitrile (c-C_6H_5CN) - and a new molecular family: HC_5O and HC_7O. In Part III, we discuss recent efforts to study the effects of shock-chemistry by studying the prototypical shocked outflow, L1157, both with interferometric observations and gas-grain chemical modeling.

Part II

Constraining Cold, Gas-Phase Carbon-Chain Chemistry: Deep GBT Spectral Surveys of TMC-1

Preface and Future Directions

While attempting to constrain the complexities of forming large organic molecules in star forming regions, it is crucial to understand what the initial ingredients one is starting with. As such, much study has gone into developing a robust chemical inventory in the first stages of star formation, and in particular dark clouds (83; 121; 135; 191). First detected with optical telescopes, these objects appears as dark globules in the foreground against the galactic stellar background. Due to relatively high densities ($n_{\mathrm{H_2}}$ $\sim$$10^4$ cm^{-3}), the interstellar dust within these clouds absorbs a large fraction of intervening photons, resulting in a high degree of visual extinction. These dark clouds are characterized by being cold ($T \sim$ 10 K) and quiescent, not undergoing any active gravitational collapse or significant physical evolution. As such, they are observationally characterized to have extremely narrow molecular line widths ($\sim$0.3 km s^{-1}), as the overall Doppler broadening of the molecules is small (32; 157).

Because of the unique physical conditions within these sources, the subsequent chemistry is also unique. The cold temperatures means that the majority of the chemistry on the ice on dust grains and in the gas-phase are mostly isolated, with very few efficient mechanisms to cause desorption (21; 103). Because saturation (i.e. the subsequent addition of hydrogen atoms to molecules containing double or triple bonds) is highly efficient on ice (e.g. CO converting to CH_3OH), the resulting gas-phase chemistry is dominated by unsaturated species. In addition, the large A_V results in very few external UV-photons being capable of penetrating the clouds to induce photodissociation. This facilitates the formation of exotic species that would normally rapidly dissociate in other physical conditions, such as diffuse clouds. For example, gas-phase reactions, such as carbon insertion, can be highly efficient at low temperatures and densities, resulting in the efficient production of unsaturated hydrocarbons and other carbon-chain molecules (103).

In particular, the Taurus Molecular Cloud (TMC-1, see Figure 1.1) has been extensively studied both observationally and theoretically. Through numerous dedicated spectral surveys (e.g. (83; 121)), approximately 20% of all known interstellar molecules were first detected in TMC-1, including several members of various unique molecular families such as carbenes (154), polyynes (11; 116; 189; 206), and unsaturated hydrocarbons (37). Due to this high degree of chemical complexity and the physical conditions being well approximated as constant over time, many astrochemical models use this source as a primary reference point and the initial conditions for more complex physical models (109; 146; 204; 229). One major way these models are tested for accuracy is by their ability to simultaneously reproduce the observed abundances towards sources like TMC-1 on a timescale that is appropriate for the age of the source. Because these models can treat the abundances of far

Figure 1.1: Optical photographic image of the night sky around TMC-1, seen top left as a dark cloud in front of the stellar background. The Pleiades open cluster can also be seen in the bottom right. *Credit: B. A. McGuire*

more molecules than can be detected, including many intermediate products, it is crucial that the inventory of observed molecular abundances covers as many species as possible.

In particular, studying the effects of carbon-chain chemistry in these sources can be very insightful to understanding the chemistry in more evolved sources. Because the species in the gas can proceed in relative isolation with respect to the frozen out solid-phase, it is possible to more easily disentangle the underlying chemistry due to the smaller number of competing physical processes. Nearly every one of the largest detected molecules (>7 atoms) contain multiple carbons, with a large majority containing 3 or more. Since the carbon-chains in these molecules are effectively the molecule's backbone, understanding how carbon-chain molecules can be formed in a controlled setting can provide crucial insights into how these larger, saturated species are formed elsewhere. Therefore, it is a worthwhile endeavor to observationally constrain the chemical reservoirs in these sources to determine the underlying gas-phase chemistry as it occurs in isolation

Building upon the highly impactful 8.8-50 GHz spectral survey of TMC-1 by Kaifu et al.

(121), we performed a deep spectral survey of TMC-1 in order to detect even weaker spectral features, and hypothetically less-abundant, previously-undetected molecules. Utilizing the advanced sensitivity and spectral resolution of the Robert C. Byrd Green Bank Telescope (GBT), our survey achieved a RMS noise level of just a few mK across $\sim$1.8 GHz of bandwidth between 18 and 24 GHz Here, we discuss three groups of new molecular detections that resulted from these observations. In Chapter 2, we discuss the detection of 8 new isotopologues (molecules that differ only in isotopic composition) of HC_5N and HC_7N and how comparing their abundances may allow us to constrain what formation route(s) could be dominant for their molecular family (cyanopolyynes) (32). Chapter 3 examines the detection of the first aromatic molecule found with radio astronomy, benzonitrile (c-C_6H_5CN), which will be a key species to trace the formation of benzene and polycyclic aromatic hydrocarbons (PAHs) (161). Finally, Chapter 4 explains the detection of a new molecular family, HC_nO, with the discovery of HC_5O and the tentative (and later confirmed) detection of HC_7O and how this family's chemistry deviates from what is seen in similar carbon-chain families (157).

Going forward, observations are currently underway to expand out this survey to take advantage of the wide range of spectral capabilities of the GBT. Currently, over 100 hours of observations have been taken non-contiguously between 8-40 GHz toward TMC-1. With these observations, we plan to achieve similar or better spectral sensitivity to our previous TMC-1 survey. This will allow for the detection of many new molecules; some potential species of interest will be discussed below.

Due to the extremely large bandwidth covered and the low line density in TMC-1, this survey will also allow for an excellent dataset to utilize velocity stacking techniques, or the co-adding of multiple spectral transitions from the same species along the same velocity bins of the spectral lines. Through this co-adding, the signal-to-noise ratio can be increased by the square root of the number of lines co-added, while sacrificing the ability to compare the relative line ratios to one other. This technique has been used previously in this source to suggest the presence of many of the molecules discussed in this manuscript (e.g. HC_7N isotopologues (135) and benzonitrile (125)). Because the spectral lines are narrow and sufficiently spaced enough in TMC-1, the chance to find interloping lines is fairly small. While this technique could be used for many proposed species, in particular, we hope to utilize this technique to detect many of the discussed simple aromatic or cyclic species that were not detected in Chapter 3. These would provide key additional handles on constraining the formation of the first aromatic molecules.

Another result from this survey we aim to achieve is to better fill out the inventory of detected isotopologues. The obvious detection of the final undetected isotopomer, $H^{13}CC_6N$, has already been tentatively confirmed in observations so far. In addition, the deep observations may be able to probe the isotopologues of some of the potential precursor species to the cyanopolynes, such as the C_nH family or other abundant hydrocarbons neutral and ion species. If these molecules have a similar isotopic composition and structure to what we see for HC_5N or HC_7N, it would provide additional evidence for the formation of large cyanopolyynes. Furthermore, utilizing velocity-stacking, it is possible we may be able to detect the low-abundance isotopologues such as $HC_7\,{}^{15}N$ and the ^{13}C

or D-substituted versions of HC_9N.

Building off of the results of Chapter 4, this survey will provide us with the proper frequency coverage to target strong transitions of the non-detected HC_nO species. Our gas-grain chemical models from that work greatly over predicts the abundance of HC_4O, however, indicating that there is likely either a missing destruction pathway or an overestimate in the formation efficiency for this molecule. Providing actual measured abundances for HC_3O, HC_4O, and HC_6O, or at least significantly improved upper limits, will greatly improve the model's ability to converge on what is producing this deviation from the observations.

In addition to this survey, several other future projects are planned to proceed further on this work. First, initial results from the expanded GBT survey suggest that different species in TMC-1 may, in fact, have different source sizes within the telescope's beam. This would imply that the physical distribution of these molecules may not be the same for all species. As such, we will propose for observations with the Karl G. Jansky Very Large Array (VLA) to see if it is possible to physically map the morphology of the molecular emission in TMC-1. This may prove to be a difficult task, however, as it is possible that a large fraction of the widely distributed material would be resolved out by the interferometer, decreasing the amount of flux we will be able to detect. But, if these morphologies are both detectable and distinct, this would provide greater insights to the underlying chemistry in dark clouds by challenging the common isotropic, isothermal assumptions used in astrochemical models of TMC-1.

Furthermore, another avenue of future work is to develop a limited gas-phase chemical network that would be capable of considering the relative abundances of different isotopomers of large carbon-chain molecules. Because any network with any single sufficiently large molecule would require a significant increase in the number of species and reactions, the total scope of the network would likely focus on a small number of families of molecules (e.g. formation of cyanopolyyne). Some initial work has been performed on the development of simple isotope networks (146; 198), but these types of networks are still relatively understudied.

CHAPTER 2

DETECTION OF HC_5N AND HC_7N ISOTOPOLOGUES IN TMC-1 WITH THE GREEN BANK TELESCOPE

The following chapter is primarily reproduced from Burkhardt, A. M.; Herbst, E.; Kalenskii, S. V.; McCarthy, M. C.; Remijan, A. J.; McGuire, B. A. Monthly Notices of the RAS ***2018****, 474, 5068-5075.*

We report the first interstellar detection of DC_7N and six ^{13}C-bearing isotopologues of HC_7N toward the dark cloud TMC-1 through observations with the Green Bank Telescope, and confirm the recent detection of $HC_5{}^{15}N$. For the average of the ^{13}C isotopomers, DC_7N, and $HC_5{}^{15}N$, we derive column densities of $1.9(2)\times10^{11}$, $2.5(9)\times10^{11}$, and $1.5(4)\times10^{11}$ cm^{-2}, respectively. The resulting isotopic ratios are consistent with previous values derived from similar species in the source, and we discuss the implications for the formation chemistry of the observed cyanopolyynes. Within our uncertainties, no significant ^{13}C isotopomer variation is found for HC_7N, limiting the significance CN could have in its production. The results further show that, for all observed isotopes, HC_5N may be isotopically depleted relative to HC_3N and HC_7N, suggesting that reactions starting from smaller cyanopolyynes may not be efficient to form HC_nN. This leads to the conclusion that the dominant production route may be the reaction between hydrocarbon ions and nitrogen atoms.

2.1 Introduction

Carbon-chain molecules are a critically important family within the interstellar medium (ISM); they represent ∼40% of all detected species and play a major role in the formation of more complex chemistry. Carbon chains with interstellar detections include: carbenes (154), polyynes (11; 116; 189; 206), unsaturated hydrocarbons (37), and the newly detected HC_nO family (157). Furthermore, it has been suggested that they may be important precursors to the formation of polycyclic aromatic hydrocarbons (PAHs) (93), which are likely to be routine targets of observation when the James Webb Space Telescope is launched in 2019 (127).

Reactions of unsaturated carbon-chain molecules (i.e. species whose available carbon valence electrons are not all bonded to atoms so that the chain contains more double and

triple carbon-carbon bonds) are often efficient in the ISM, but have many product channels for which branching ratios are not known. Because of the lack of available laboratory measurements of the dominant reaction mechanisms and rate coefficients for these branching fractions, the ability to directly investigate these pathways through interstellar observations is therefore appealing. One way to probe the underlying chemistry is through the study of the isotopologues (molecules that differ only in isotopic composition (e.g. HCCCN vs H^{13}CCCN)) and isotopomers (molecules that contain the same isotopic composition, but differ in the isotope positions (e.g. H^{13}CCCN vs HCC^{13}CN)) of a species. For many molecules, specific relative isotopic fractions or isotopomer configurations can possibly constrain the dominant production method or precursors.

TMC-1, one of the prototypical dark cloud cold cores, has been the subject of intense astrochemical study. Observationally, it has been the source of many new molecular detections, including a large fraction of the known unsaturated carbon-chains (121; 152; 157; 189; 206). Furthermore, TMC-1 is dynamically stable, characterized by narrow line widths ($\sim$0.3 km s^{-1}), cold excitation temperatures (5-10 K), and a low line density ($\sim$1 line per 200 km s^{-1} for reasonable integration times with the GBT), making it ideal for the unambiguous detection of new molecules. Finally, because of its simple physical history, it is an ideal source to test chemical network models (96; 103; 147; 199).

Cyanopolyynes, a family of linear molecules of the form HC$_n$N (where n = 3, 5, 7, etc., henceforth) with alternating single and triple-bonded carbon atoms, have been detected in cold dark clouds (29), the expanding envelopes of evolved stars (12), and even external galaxies (151). It has been shown that, unlike many carbon-chains, the ^{12}C/^{13}C ratio for HC$_5$N is constant even into subsequent stages of star formation through observations of warm carbon-chain chemistry in the low-mass star-forming region L1527 (6; 218). This finding implies that the formation of cyanopolyynes may occur primarily under dark cloud conditions. These species then remain as relics in subsequent stages of star formation, and have a unique underlying chemistry compared with other carbon-chain molecules. However, recent observations of a more evolved core, L134N, suggest that other formation pathways may dominate at later times (215).

Of particular interest, Loomis et al. (141) recently discussed the non-detection of HC$_{11}$N, which deviates from the log-linear abundance vs molecular size trend seen for smaller cyanopolyynes (11; 31; 175; 189). Although this trend was previously thought to arise from a consistent set of gas-phase reactions that add carbons directly to smaller HC$_n$N species (31; 72; 190; 236), it was proposed by Loomis et al. (141) that cyclisation processes may need to be considered to accurately explain this deviation. It is clear, therefore, that the chemistry of this family of species is not fully understood, especially at larger molecular sizes, and further study is needed.

For the cyanopolyyne family, Takano et al. (214) and Taniguchi et al. (216) discussed the potential prominence of three formation routes, among others, for a given molecule (HC$_n$N), which could each result in different ^{12}C/^{13}C fractionations. Each of these numbered mechanisms is discussed below, and, for clarity, sources of carbon atoms which could result in ^{13}C fractionation are traced from reactants to products in example reactions in red.

Mechanism 1 - The reaction between hydrocarbon molecules and the CN radical, including

$$C_{n-1}H_2 + CN \rightarrow HC_{n-1}CN + H. \tag{2.1}$$

Here, the difference between the isotopic fractions of the CN carbon atom and the carbene C_nH_2 carbon atoms results in asymmetric fractionation along the chain (72; 101).
Mechanism 2 - Reactions of the next-smallest cyanopolyyne (e.g. HC_5N vs HC_3N) with hydrocarbons, such as

$$C_2H + HC_{n-2}N \rightarrow HC_2C_{n-2}N + H. \tag{2.2}$$

For this case, many of the isotopomers would have similar $^{12}C/^{13}C$ ratios to their corresponding isotopomer of the precursor cyanopolyyne, with potentially some small variations depending on the precursor hydrocarbon (113; 202).
Mechanism 3 - Reactions of nitrogen atoms and hydrocarbon ions containing the same number of carbon atoms. One such example is

$$\begin{aligned} C_nH_3^+ \quad + N &\rightarrow H_2C_nN^+ + H \\ H_2C_nN^+ + e^- &\rightarrow HC_nN \quad + H. \end{aligned} \tag{2.3}$$

In this scenario, $^{12}C/^{13}C$ fractionation would be set by this precursor ion. Assuming the ion's carbon atoms are sufficiently scrambled, this manifests as no significant variations among the isopotomers' ratios (97; 100; 129).

Previously, the $^{12}C/^{13}C$ fractionation had only been studied for cyanoacetylene (HC_3N) and cyanodiacetylene (HC_5N). For HC_3N, Takano et al. (214) found that toward TMC-1 there was a ∼40% abundance enhancement of the isotopomer with the ^{13}C residing next to the nitrogen atom ($HC_2{}^{13}CN$) relative to the other two species, suggesting that the primary formation route could be the neutral reactions between the abundant CN and C_2H_2 (Mechanism 2.1). This enhancement in the ^{13}CN is thought to result from the exothermic exchange reaction given by

$$CN + {}^{13}C^+ \rightarrow {}^{13}CN + C^+ + \Delta E(34K). \tag{2.4}$$

Because the reaction is exothermic, only the forward process is efficient at the cold temperatures within dark clouds, which results in an enhanced ^{13}C fractionation in CN compared with the carbene precursors whose exchange reactions are much less efficient (17; 234). This enhancement of ^{13}C in CN relative to measured solar system isotopic fractions has been ubiquitously observed in Galactic molecular clouds (166).

Meanwhile, Taniguchi et al. (216) found that there was no significant difference in the abundance of the ^{13}C-isotopomers of HC_5N toward TMC-1, suggesting that the primary formation route for HC_5N could be from reactions of N with hydrocarbon ions (such as $C_5H_3^+$, $C_5H_4^+$, and $C_5H_5^+$).

It is also important to compare these results to the dominant formation routes within chemical network models. Significant work has been done for this molecular family by

Loomis et al. (141) and McGuire et al. (157) who adapted the KIDA network within NAUTILUS (199). At the model's time of best agreement, multiple formation routes significantly contributed (>30%) to the formation of cyanopolyynes, many of which do not necessarily agree with the observational constraints.

We have recently performed deep observations of TMC-1, which has resulted in the interstellar detection of several new molecules (157). Here, we present the detection of six of the seven possible ^{13}C-bearing isotopomers of HC_7N, as well as DC_7N. In addition, we confirm the recent detection of $HC_5{}^{15}N$. The observations are presented in §2.2, a review of the laboratory spectroscopy is given in §2.3, the results and analysis are discussed in §2.4, and a discussion of the astrochemical implications is given in §2.5.

2.2 Observations

Observations, described previously by McGuire et al. (157), toward TMC-1 were performed on the 100 m Robert C. Byrd Green Bank Telescope (GBT) in Green Bank, WV with the K-band Focal Plane Array (KFPA) along with the Versatile GBT Astronomical Spectrometer (VEGAS) spectrometer backend. The beam size varied from 32-40″across the observed frequency range, with a beam efficiency of ∼0.92. The VEGAS backend was configured for 187.5 MHz bandwidth and 1.4 kHz (0.02 km s^{-1}) spectral resolution. In two separate frequency setups, a total of ten individual passbands were observed for a total of 1875 MHz of spectral coverage between 18 and 24 GHz. The observations were centred on α(J2000) = 04$^{\rm h}$41$^{\rm m}$42$^{\rm s}_{.}$5, δ(J2000) = 25°41′27″$_{.}$0, with pointing corrections performed hourly with an estimated uncertainty of ∼2″. The system temperatures ranged between 40-80 K during the observations.

Position-switching mode was used with a 120 s ON-OFF cadence and a position 1°offset from the target. In total, each of the ten frequency windows were observed between ∼7.5 and 15 hours on source. Data reduction was performed using the GBTIDL package. The data were placed on the atmosphere-corrected T_A^* scale (226) and averaged. A polynomial fit was used to remove the baseline. Subsequent smoothing to a spectral resolution of 5.7 kHz (∼0.08 km s^{-1}) improved the signal to noise ratio (SNR) in the weaker features while maintaining at least 3 channels sampling across the narrowest spectral feature observed. This resulted in final RMS noises of 3-5 mK (Table 2.1)

2.3 Spectroscopy

For the new species detected here, McCarthy et al. (153) measured the pure rotational spectra of the isotopologues of several cyanopolyynes, including HC_7N, between 6 and 17 GHz, and resolved the nitrogen hyperfine splitting. The rotational spectrum for $HC_5{}^{15}N$ was measured by Bizzocchi et al. (24). The corresponding quantum transitions, frequencies (MHz), line strengths (D^2), and upper-level energies (K) for transitions falling within our observational coverage are shown in Table 2.1.

Table 2.1: Measured and observed frequencies of detected HC_7N and HC_5N isotopomer and isotopologue transitions covered in this work and pertinent line parameters from Gaussian fits.

Species	$J' \rightarrow J''$	Frequency[a] (MHz)	$V_{\rm lsr}$ [b] (km s^{-1})	ΔT_A^* [c] (mK)	ΔV (km s^{-1})	$S_{ij}\mu^2$ (Debye^2)	E_u (K)
HC_7N	17→16	19175.959	5.81	909(3)	0.474(2)	394.9	8.283
	18→17	20303.946	5.83	978(2)	0.458(1)	418.2	9.257
$HC_6{}^{13}CN$	18→17	20071.326	5.84	12(1)	0.36(5)	418.2	9.151
	19→18	21186.389	5.86	13.2(9)	0.46(3)	441.4	10.168
	20→19	22301.449	5.84	19(3)	0.31(6)	464.7	11.238
$HC_5{}^{13}CCN$	17→16	19102.044	5.84	16(1)	0.52(5)	394.9	8.251
$HC_4{}^{13}CC_2N$	18→17	20294.271	5.89	12(1)	0.54(8)	418.3	9.253
$HC_3{}^{13}CC_3N$	17→16	19165.136	5.70	9.9(4)	0.50(2)	394.9	8.278
$HC_2{}^{13}CC_4N$	17→16	19097.498	5.81	12.8(3)	0.48(1)	394.9	8.249
	18→17	20220.870	5.76	14(3)	0.32(8)	418.2	9.219
$HC^{13}CC_5N$	18→17	20063.864	5.80	9(1)	0.51(7)	418.1	9.148
	20→19	22293.157	5.76	18(3)	0.42(8)	464.6	11.234
$H^{13}CC_6N$	21→20	23168.899	-[d]	<14.8[d]	0.4[d]	487.4	12.231
DC_7N	19→18	20721.873	5.97	15(3)	0.34(7)	441.4	9.945
	20→19	21812.486	5.84	12.2(6)	0.62(4)	464.7	10.992
	21→20	22903.097	5.92	16(1)	0.49(6)	487.9	12.091
HC_5N	8→7, F=8→8	21299.750	5.82	32(3)	0.43(4)	0.781	4.600
	8→7, F=7→6	21301.245				43.3	4.600
	8→7, F=8→7	21301.261	5.82	2489(11)	0.650(3)	49.2	4.600
	8→7, F=9→8	21301.272				55.9	4.600
	8→7, F=7→7	21302.970	5.85	25(2)	0.54(6)	0.781	4.600
$HC_5{}^{15}N$	8→7	20778.180	5.78	16.9(9)	0.46(3)	150.0	4.487
$HC_4{}^{13}CN$	7→6	18454.489	5.80	28(1)	0.76(4)	131.2	3.543
$HC_3{}^{13}CCN$	8→7	21281.792	5.82	40(2)	0.59(3)	151.4	4.596
$HC_2{}^{13}CC_2N$	8→7	21279.200	5.81	42(2)	0.67(4)	150.0	4.596
$HC^{13}CC_3N$	7→6	18447.612	5.81	20(1)	0.79(5)	130.0	3.541
$H^{13}CC_4N$	8→7	20746.761	5.81	42(1)	0.59(2)	150.0	4.481
DC_5N	8→7	20336.870	5.82	52(2)	0.47(2)	150.001	4.392
	9→8	22878.963	5.86	59(2)	0.54(2)	168.729	5.490

[a] McCarthy et al. (153) had a 1σ experimental uncertainty of ∼2 kHz.
Bizzocchi et al. (24) had a 1σ experimental uncertainty of ∼15 kHz.
[b] 1σ uncertainties from Gaussian fits are ∼0.5 kHz (0.08 km s^{-1}). Given the SNR of the detected lines (∼3-5) and the linewidth, we estimate the uncertainty in the observed line centres to be ∼3.7 kHz.
[c] 1σ uncertainty of the Gaussian fit to each line given.
[d] Upper limit of line peak set by 3×RMS at transition frequency.
For purposes of N_T calculations, ΔV was estimated to be 0.4 km s^{-1}.

2.4 Results and Analysis

We detected, for the first time, emission from DC_7N and six ^{13}C-bearing isotopologues of HC_7N. In addition, we confirm the recent detection of $HC_5{}^{15}N$ (217) with the observation of the J=8→7 transition, which was not reported in that work. For the ^{13}C-isotopomers, at least one ΔJ transition between 17→16 and 20→19 was detected for six of the seven isotopomers. In addition, two transitions of DC_5N, two transitions of HC_7N, and a set of 5 hyperfine components of a single ΔJ for HC_5N were also detected. Spectra for these species are shown in Figures 2.1 and 2.2. The lines are seen at a v_{lsr} ∼5.8 km s^{-1}, typical of molecules in this source (121). For the one non-detected isotopomer, $H^{13}CC_6N$, an upper limit on the column density was derived whose value is consistent with the other detected isotopomers.

In TMC-1, the molecular emission can be well described by a single excitation temperature between T_{ex} ∼5-10 K (141; 189). To calculate the column density, we use the formalism described in (110) and given by

$$N_T = \frac{Qe^{E_u/T_{ex}}}{\frac{8\pi^3}{3k_B}\nu S_{ij}\mu^2} \times \frac{\frac{1}{2}\sqrt{\frac{\pi}{\ln 2}}\frac{\Delta T_A^* \Delta V}{\eta_B}}{1 - \frac{e^{h\nu/k_B T_{ex}} - 1}{e^{h\nu/k_B T_{bg}} - 1}}. \tag{2.5}$$

Here N_T is the column density (cm^{-2}), Q is the partition function (see below), E_u is the upper state energy of a given transition (K), T_{ex} is the excitation temperature (K), ν is the transition rest frequency (Hz), S_{ij} is the intrinsic line strength, μ^2 is the transition dipole moment squared (J cm^3), ΔT_A^* is the peak intensity (K), ΔV is the fitted FWHM linewidth (cm s^{-1}), η_B is the beam efficiency (∼0.92 at 20 GHz for the GBT), and T_{bg} is the continuum background temperature (2.73 K). Because of the narrow range of upper level energies of the observed transitions, we assume that $T_{ex} = 7$ K for all species.

The total partition function Q accounts for both the rotational and vibrational contributions, as described by

$$Q = Q_{\text{vib}} \times Q_{\text{rot}}. \tag{2.6}$$

While the rotational component dominates at interstellar conditions, cyanopolyynes can have Q values that can be affected by the vibrational component at even modest excitation temperatures. We utilised the calculated harmonic stretching vibrational wavenumbers (ω) for HC_7N by (28), with the assumption that the partition function will not be significantly impacted by the presence or location of ^{13}C or D in the molecule. The lowest three energy levels for HC_7N are 62, 163, and 280 cm^{-1} (92, 241, and 415 K, respectively). At 7 K, the change from the vibrational contribution is negligible ($\Delta Q/Q\,[7\text{ K}] \sim 10^{-6}$); this correction becomes ≳1% at $T_{ex} \gtrsim 20$ K. Similar behavior is seen for HC_5N isotopologues.

Values of ΔT_A^* and ΔV were determined by Gaussian fits to the lines (see Table 2.1). For species with more than one transition, a single column density was obtained based on a least-squares fit to reproduce the integrated line intensities, with a weighting based on the SNR of the lines. The calculated column densities are summarized in Table 2.2.

To calculate the uncertainties, we considered both the measurements and analysis. The absolute flux calibration procedure for the GBT is estimated to have ∼20% uncertainty.

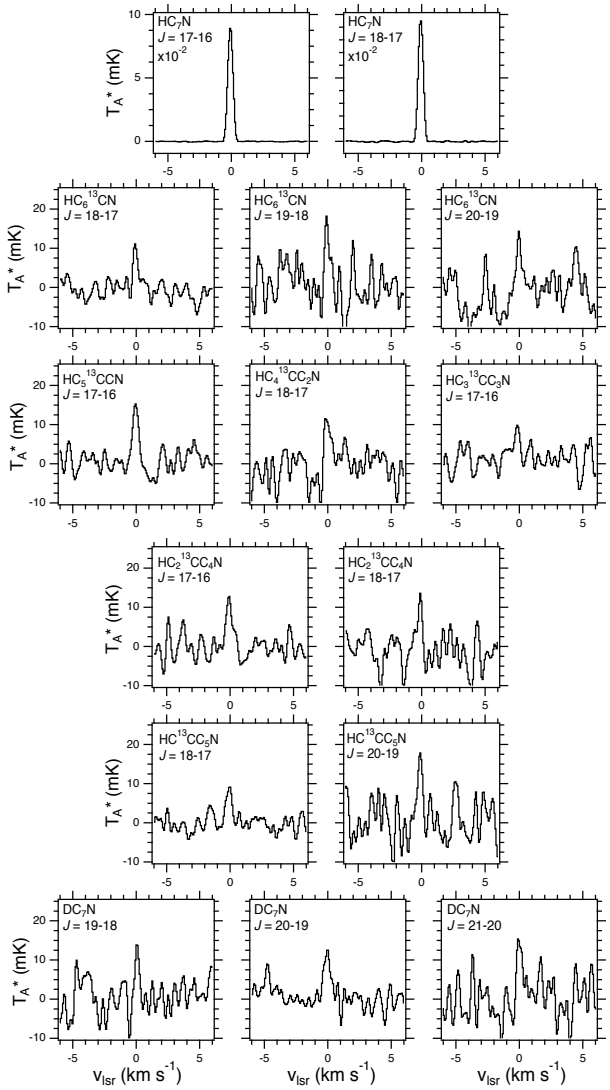

Figure 2.1: Detected transitions of HC_7N isotopologues, organized by isotope-location and corresponding quantum numbers for each transition (labelled on in top left of each spectra). Velocities are given with respect to $V_{\rm lsr}$ of the transition rest frequency, with the listed transition centred at 0 km s^{-1}.

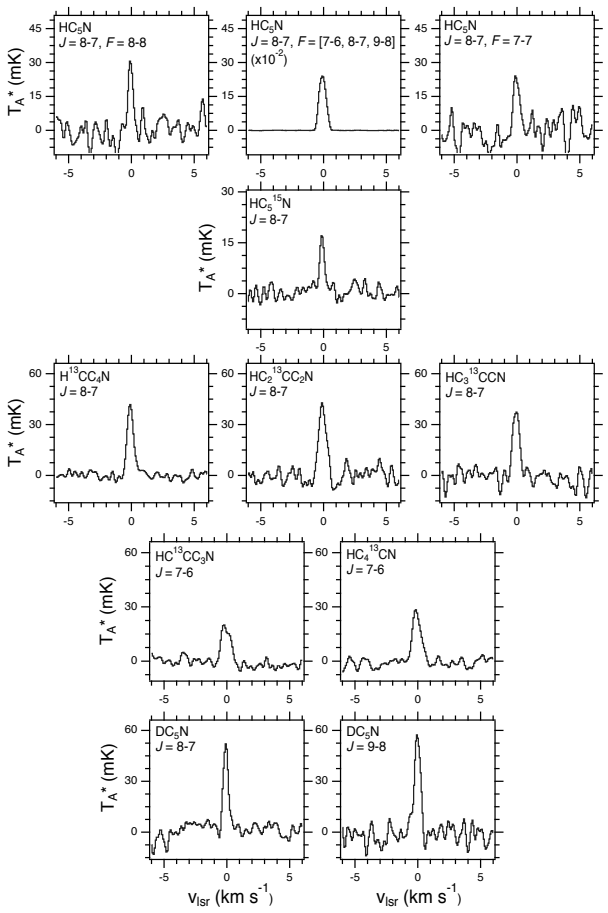

Figure 2.2: Detected transitions of HC_5N isotopologues, organized by isotope-location and corresponding quantum numbers for each transition (labelled on in top left of each spectra). Velocities are given with respect to $V_{\rm lsr}$ of the transition rest frequency, with the listed transition centred at 0 km s^{-1}.

Table 2.2: Measured column densities and upper limits for isotopomers and isotopologues discussed here, and, when relevant, the isotopic ratio (i.e. $^{12}C/^{13}C$; H/D; $^{14}N/^{15}N$).

Species	N_T ($\times 10^{11}$ cm^{-2})	N_T/N_{H_2} ($\times 10^{-11}$)	Isotopic Ratio†	$\mathcal{R}^{\ddagger}$
HC_7N	139(36)	139(36)	-	-
$HC_6{}^{13}CN$	1.7(6)	1.7(6)	83(34)	85(35)
$HC_5{}^{13}CCN$	2.6(7)	2.6(7)	52(20)	53(20)
$HC_4{}^{13}CC_2N$	2.1(7)	2.1(7)	66(27)	67(28)
$HC_3{}^{13}CC_3N$	1.6(4)	1.6(4)	88(32)	90(33)
$HC_2{}^{13}CC_4N$	1.8(5)	1.8(5)	78(31)	79(32)
$HC^{13}CC_5N$	2.0(7)	2.0(7)	71(31)	73(31)
$H^{13}CC_6N$	<2.2	<2.2	>63	>64
DC_7N	2.5(9)	2.5(9)	56(24)	61(29)
Weighted ^{13}C Average Value	1.9(2)	1.9(2)	73(21)	75(21)
Total ^{13}C-isotopologue*	13.3(1.8)	13.3(1.8)	9.6(2.7)%$^{\ominus}$	9.4(2.7)%$^{\ominus}$
HC_5N	492(122)	492(122)	-	-
$HC_5{}^{15}N$	1.5(4)	1.5(4)	326(109)	344(114)
$HC_4{}^{13}CN$	4.6(9)	4.6(9)	107(35)	108(36)
$HC_3{}^{13}CCN$	4.4(9)	4.4(9)	111(37)	113(38)
$HC_2{}^{13}CC_2N$	5.3(1.2)	5.3(1.2)	93(31)	94(32)
$HC^{13}CC_3N$	3.4(7)	3.4(7)	144(47)	146(49)
$H^{13}CC_4N$	4.8(1.0)	4.8(1.0)	102(33)	103(34)
DC_5N	5.3(1.2)	5.3(1.2)	92(30)	96(32)
Weighted ^{13}C Average Value	4.4(4)	4.4(4)	111(30)	113(31)
Total ^{13}C-isotopologue*	22(3)	22(3)	4.5(1.2)%$^{\ominus}$	4.4(1.2)%$^{\ominus}$

† Column density ratio of most common isotopologue vs less common species given (e.g. $^{12}C/^{13}C$; H/D; $^{14}N/^{15}N$)

‡ Isotope ratio, including the all other singly-substituted isotopologues (see section 2.4.2)

* Calculated by 7 times the weighted average of ^{13}C values

$^{\ominus}$ Percent of total molecular density of HC_nN containing a single ^{13}C substitution

We include 1σ uncertainties in ΔT_A^* and ΔV derived from the Gaussian fits. Due to our assumption of a single excitation temperature of T_{ex}= 7 K, we find that variations of previously calculated excitation temperatures (5-10 K) result in between 15-20% uncertainty in the resulting column densities for HC_7N isotopologues and $\sim$5% for HC_5N isotopologues. We assume that the source is significantly extended beyond the GBT beam, and thus the contributions to the uncertainty from pointing are trivial, and no beam filling correction is applied. The resulting column densities, with all uncertainties added in quadrature, are given in Table 2.2.

For the purposes of calculating the molecular abundances, we used the H_2 column density derived by Gratier et al. (83) from observations from Kaifu et al. (121) of N_{H_2}=10^{22} cm^{-2}, with the caveat that the beam size of the survey performed with the Nobeyama 45m dish telescope is about twice that of the GBT, and thus a non-isotropic distribution of H_2, or any molecular species, may result in different column densities derived between the observations. These abundances are also given in Table 2.2. In addition to comparing the relative column densities of the isotopomers, an average value across all detected ^{13}C-isotopomers is also calculated. The column density for each detected species was averaged, weighted by the error of each value, and are also tabulated in Table 2.2. These calculated values are compared to previous observations in Table 2.3.

2.4.1 Treatment of Hyperfine Splitting

For HC_5N, the brightest detected signal is a blend of three hyperfine components. Two additional, weaker ΔF=0 hyperfine components are resolved. The central, bright feature has been shown to be slightly optically thick (83). Our calculation of the column density was therefore derived using the two, optically-thin hyperfine components, yielding a value of 5(1)$\times10^{13}$ cm^{-2}, in agreement with the previous work (83; 145; 216).

For all other species studied here, the hyperfine components are unresolved. As such, for the purposes of calculating column densities, the hyperfine splitting is not considered and the integrated intensity is used instead. This likely slightly overestimates the linewidths due to the blending of hyperfine components. However, this is still a reasonable assumption, as the lines are well-modeled by a single Gaussian lineshape, and thus will not significantly impact the resulting column densities, which are calculated via the integrated intensity in Equation 2.5.

2.4.2 Calculation of Line Ratios and Total Values

Relative isotopic ratios calculated for H/D, ^{12}C/^{13}C, and ^{14}N/^{15}N are tabulated in Table 2.2. It should be noted that none of the uncertainties described above for determining the column densities should cancel out in the calculation of the ratios, as the uncertainty in the absolute flux calibration comes from the time and frequency variability of the calibrator source. For HC_7N, where we lack a detection of $H^{13}CC_6N$, we calculate a total column density of all ^{13}C-substituted isotopomers by scaling the average column density for the

isotopologue by the number of isotopomers, which is equal to the number of carbon atoms in the molecule.

As discussed in Langston and Turner (135), the presence of isotopologues affects the observed abundances of the main isotopic species, especially for increasingly complex molecules. As the number of atoms in a species increases, so does the probability that any given molecule will contain at least a single isotope-substituted atom. This would be most apparent in fullerenes like C_{60}, where a Galactic $^{12}C/^{13}C$ ratio of $\sim$68, or 1.5%, (166) would result in $\sim$60% of all C_{60} containing, at least one ^{13}C substitution. Similarly, it may be important to consider the size of the molecule when comparing the total isotopologue fraction. Given the same ISM ratio and purely ^{13}C-substitution, and no additional chemical bias, the larger cyanopolyynes would be expected to have the following total singly-substituted ^{13}C fractional abundances: HC_5N (7.2%), HC_7N (10%), HC_9N (12%), $HC_{11}N$ (15%).

Given the non-trival fraction of isotopologues for a given large species, as the observational capabilities improve it will likely be important to consider their abundances when calculating isotopic ratios. For the purposes of comparing to standard ISM values, a more accurate ratio for fractionation would be (taking ^{15}N of HC_5N as an example)

$$\mathcal{R} = \frac{N_T(HC_5N) + \Sigma N_T(H^{13}CC_4N \text{ isotopomers}) + N_T(DC_5N)}{N_T(HC_5{}^{15}N)}. \tag{2.7}$$

Here, it is assumed that doubly-substituted isotopologues do not contribute significantly yet to the ratio, which may not be valid for species as large as C_{60}. In addition to the standard column density ratio given, this additional value is also given in Table 2.2, even though the relative differences ($\sim$10%) are still well within the observational uncertainties. As chemical models increase their molecular complexity, it will become increasing important to consider the isotopologues of large molecules, as well as their precursor species. This is already shown by (147) on the modeling of deuterated species toward TMC-1, where the robust inclusion of deuterated chemistry was found to alter the chemical timescales by up to a factor of 3. This effect will also be more apparent when species contain at least one atom with a higher natural percentage in non-standard isotopes, such as S and Cl and species common in silicate grain precursors (Mg, Si, Ti, Fe). While the upper limit of this effect will likely decrease the modeled abundances by no more than roughly factor of 2, it is certainly an important effect to consider in the future.

Table 2.3: Comparison of observed ratios to previous values of cyanopolyynes and related species in the literature.

Ratio	$^{12}C/^{13}C$						H/D				$^{14}N/^{15}N$				
Source	HC_7N	HC_5N	HC_3N	HCN	CN†	ISM‡	HC_7N	HC_5N	HC_3N	HCN	HC_5N	HC_3N	HCN	CN†	ISM†
This work	73(21)	111(30)	-	-	-	-	56(24)	92(30)	-	-	326(109)	-	-	-	-
A	87^{+35}_{-19}	-	-	-	-	-	>59	-	-	-	>52	-	-	-	-
B	-	54^{+21}_{-22}	130^{+23}_{-50}	-	-	-	-	52^{+26}_{-20}	81^{+82}_{-68}	-	-	-	-	-	-
C	-	94(6)	-	-	-	-	-	-	-	-	-	-	-	-	-
D	-	-	77(7)⋆ 55(7)⋆	-	-	-	-	-	-	-	-	-	-	-	-
E	-	-	56.8⊖	69⊖	-	-	-	-	71⊖	91(38)	-	-	-	-	-
F	-	-	-	-	68(15)	-	-	-	-	-	-	-	-	-	-
G	-	-	-	-	-	88.9(6)	-	-	-	-	-	-	-	-	424(3)
H	-	-	-	-	-	-	-	83^{83}_{-21}	-	-	-	-	-	-	-
I	-	-	-	-	-	-	-	62(12)	>17(6)	-	-	-	-	-	-
J	-	-	-	-	-	-	-	-	22(12)	-	-	-	-	-	-
K	-	-	-	-	-	-	-	-	-	-	344(53)	257(54)	-	-	-
L	-	-	-	-	-	-	-	-	-	-	-	-	323(63)✠	-	-
M	-	-	-	-	-	-	-	-	-	-	-	-	-	274(18)	-
N	-	-	-	-	-	-	-	-	-	-	-	-	-	-	441(5)

† CN values acquired from observations of Galactic diffuse molecular clouds

‡ ISM values acquired from solar system measurements (i.e. Local ISM)

⋆ First value is average of $H^{13}CC_2N$ and $HC^{13}CCN$. Second value is for $HC_2{}^{13}CN$

⊖ Uncertainties not given for most values in Turner (225)

✠ Value given in literature is $H^{13}CN/HC^{15}N$, which we was scaled by the $HCN/H^{13}CN$ ratio from Turner (225)

References: [A] Langston and Turner (135); [B] Gratier et al. (83); [C] Taniguchi et al. (216); [D] Takano et al. (214); [E] Turner (225); [F] Milam et al. (166); [G] Meibom et al. (164); [H] MacLeod et al. (145); [I] Schloerb et al. (203); [J] Howe et al. (111); [K] Taniguchi and Saito (217); [L] Ikeda et al. (114); [M] Ritchey et al. (195); [N] Marty et al. (150)

2.5 Discussion

Constraining the chemistry for larger cyanopolyynes requires the consideration of both the possible formation routes, as described in §3.1, and the many precursor species, whose isotopic ratios across the literature are summarized in Table 2.3. The analysed isotopic ratios in this work agree reasonably well with previous observations or lower limits for the same species. The general spread in values for a given species may be attributable to the spread in excitation temperatures used (5-10 K) or inconsistent treatments of both the optical depths and hyperfine structure in the column density calculations for HC_5N and HC_7N. For HC_3N, the relative enhancement of $^{12}C/^{13}C$ for $HC_2{}^{13}CN$ and the agreement of the $^{14}N/^{15}N$ ratio with Galactic measurements of CN both indicate that this species may be efficiently produced through the reaction containing CN, as described in Mechanism 2.1 (214). Taniguchi et al. (216) showed that HC_5N does not show this same trend. Through the comparison of the various isotopologues studied here, it is further possible to differentiate among the three mechanisms described in §3.1 for both HC_5N and HC_7N.

In contrast to the ∼40% enhancement of $HC_2{}^{13}CN$ over $HC^{13}CCN$ and $H^{13}CC_2N$ (214), the relative isotopic ratios of all ^{13}C isotopomers for both HC_7N and HC_5N were all consistent with their respective average values within our uncertainties. The ratio of column densities of the $HC_{n-1}{}^{13}CN$ isotopomers to the weighted average ^{13}C-isotopolouge values can be used to more explicitly test the significance of Mechanism 1 in the formation of larger cyanopolyynes. Specifically the column densities of $HC_4{}^{13}CN$ and $HC_6{}^{13}CN$ agree with their respective ^{13}C average values to <10%. Because both HC_5N and HC_7N do not display the $HC_{n-1}{}^{13}CN$ enhancement, this provides evidence that larger cyanopolyynes are not produced from CN to the same extent as HC_3N. Even though $H^{13}CC_6N$ was not detected here, the formation route from CN should not significantly alter the $^{12}C/^{13}C$ isotopic ratio of this molecule and so does not conflict with this conclusion. Thus, we can eliminate Mechanism 2.1 as the dominant pathway for both HC_5N and HC_7N.

As seen Table 2.3, while still in agreement within the uncertainties, all isotopologues of HC_5N are found to be depleted (i.e. larger isotopic ratios) relative to HC_3N and HC_7N, showing that this isotopic depletion seen in Taniguchi et al. (216) does not continue for HC_7N. While the average $^{12}C/^{13}C$ ratio for HC_7N agrees very well with ratios corresponding to HCN, Galactic measurements of CN, and the two non-enhanced isotopomers of HC_3N, the average HC_5N $^{12}C/^{13}C$ ratio is ∼50% larger than any of these values. For $HC^{15}N$, the $^{14}N/^{15}N$ ratio is much larger compared to HC_3N and Galactic measurements of CN, which have been shown to have enhanced ^{15}N isotopologue abundances relative to average ISM values (105; 195; 198). Similarly, the DC_5N abundance is diminished by roughly the same percentage relative to HC_7N as the ^{13}C-substituted isotopologues in our data. However, large uncertainties due to the SNR of our data and inconsistent treatment of the excitation temperature and hyperfine splitting across the literature results in a large spread of H/D for any given species, making this trend less certain than for the $^{12}C/^{13}C$ and $^{14}N/^{15}N$ ratios. Considering all of this, the mixture of formation and destruction methods for cyanopolyynes appears to not be consistent across the molecular family.

More specifically, because the $^{12}C/^{13}C$ ratio in HC_5N is not in agreement with the ratios

observed for HC_3N and HC_7N, the carbon fractionation in these species does not appear to be inherited from the next-smallest cyanopolyyne, as would be predicted by Mechanism 2.2. Given that Mechanism 2.2 is inefficient for HC_5N and HC_7N production, the only remaining formation pathway proposed is the reaction of hydrocarbon ions with nitrogen atoms (Mechanism 2.3), and thus is the best prediction for the dominant production route for large cyanopolyynes. If the trends discussed here are found to be true, a dedicated investigation of the underlying chemistry of hydrocarbon ions and undetected C_nH isotopologues may reveal a unique ^{13}C distribution and provide constraints on the formation of cyanopolyynes and other carbon-chain molecules.

2.6 Conclusions

The interstellar detections of DC_7N, six of the seven ^{13}C-bearing isotopologues of HC_7N, and $HC_5{}^{15}N$ are reported toward TMC-1 with observations using the GBT. Column densities for each of the detected species and an upper limit for $H^{13}CC_6N$, were calculated, as well as the resulting isotopic ratios for each species. From analysis of these ratios, we find that:

- There are no significant $^{12}C/^{13}C$ variations among the isotopomers of both HC_5N and HC_7N, implying that CN is not an important precursor for their formation.
- For all isotopologues studied in this work, while the values still agree within our uncertainties, HC_5N is found to be isotopically depleted relative to other HC_nN molecules and this depletion does not continue onto HC_7N. Given also that the ^{13}C and ^{15}N ratios for HC_3N and HC_7N agree very well, there is evidence that cyanopolyynes are not efficiently formed from their next-smallest molecular family member, $HC_{n-2}N$
- As a result, the only remaining significant formation route for HC_5N and HC_7N is the reaction of hydrocarbon ions and nitrogen atoms

Acknowledgements

A.M.B. is a Grote Reber Fellow, and support for this work was provided by the NSF through the Grote Reber Fellowship Program administered by Associated Universities, Inc./National Radio Astronomy Observatory and the Virginia Space Grant Consortium. E. H. thanks the National Science Foundation for support of his astrochemistry program. S.V.K. acknowledges support from Basic Research Program P-7 of the Presidium of the Russian Academy of Sciences. A.M.B. thanks C.N. Shingledecker for helpful discussions on chemical models for cyanopolyynes. B.A.M. thanks K. L. Lee for helpful discussions regarding vibrational energy levels. The National Radio Astronomy Observatory is a facility of the National Science Foundation operated under cooperative agreement by Associated

Universities, Inc. The Green Bank Observatory is a facility of the National Science Foundation operated under cooperative agreement by Associated Universities, Inc. The authors thank the anonymous referee for comments that improved the quality of this manuscript.

CHAPTER 3

DETECTION OF THE AROMATIC MOLECULE BENZONITRILE (*c*-C_6H_5CN) IN THE INTERSTELLAR MEDIUM

The following chapter is primarily reproduced from McGuire, B. A.; Burkhardt, A. M.; Kalenskii, S.; Shingledecker, C. N.; Remijan, A. J.; Herbst, E.; McCarthy, M. C. Science ***2018****, 359, 202-205.*

3.1 Introduction

Polycyclic aromatic hydrocarbons and polycyclic aromatic nitrogen heterocycles are thought to be widespread throughout the Universe, because these classes of molecules are probably responsible for the unidentified infrared bands, a set of emission features seen in numerous Galactic and extragalactic sources. Despite their expected ubiquity, astronomical identification of specific aromatic molecules has proven elusive. We present the discovery of benzonitrile (*c*-C_6H_5CN), one of the simplest nitrogen-bearing aromatic molecules, in the interstellar medium. We observed hyperfine-resolved transitions of benzonitrile in emission from the molecular cloud TMC-1. Simple aromatic molecules such as benzonitrile may be precursors for polycyclic aromatic hydrocarbon formation, providing a chemical link to the carriers of the unidentified infrared bands.

The mid-infrared spectra, roughly from 3 to 20 μm, of the interstellar medium (ISM) and photodissociation regions (PDRs) in both our Galaxy (144) and external galaxies (187) are dominated by emission features commonly referred to as the unidentified infrared (UIR) bands. Due to the close agreement of prominent UIR features with the characteristic vibrational frequencies of aromatic C-C and C-H bonds, it is now widely accepted that polycyclic aromatic hydrocarbons (PAHs), and fullerenes like the recently detected C_{60}^+ molecule (35), and their closely related derivatives, are probably the carriers responsible for most of these features (220). A substantial fraction of interstellar carbon is calculated to be in the form of PAHs ($\sim$10%; (44)), yet the origin of these aromatic species is a topic of considerable debate. In the diffuse ISM and PDR regions, where 30–60% of the carbon is locked up in dust grains (59), top-down models of PAH formation – through the destruction of dust grains by the harsh radiation environment, shock waves, or both – may be viable pathways (23). In denser molecular clouds which are not subject to the ultra-

violet radiation and which haven't been subject to shocks, other pathways must exist to synthesize these species from smaller precursor molecules.

Despite the widespread acceptance of PAHs as a common class of interstellar molecules, no specific PAH has been identified in the ISM, either by rotational spectroscopy or by observations of its infrared features, despite long and sustained efforts (130). In the microwave and (sub-)millimeter regimes, while some laboratory data do exist (219), such studies are relatively uncommon. Many PAHs are poor candidates for detection through radio astronomy, both because of unfavorably large rotational partition functions and because they are either apolar or weakly polar, and thus lack sufficiently intense rotational lines (compared to linear molecules of similar composition and size). A notable exception is corrannulene ($C_{20}H_{10}$), a bowl-shaped molecule with a relatively large permanent dipole moment (2.07 Debye (D); (143)), but astronomical searches for that molecule have been unsuccessful as well (180). In the infrared, while a concerted effort has been undertaken to catalog both laboratory and theoretical vibrational and Raman spectra of PAHs (25), the structural similarities among individual species result in spectra that are often indistinguishable at the modest resolving power that can routinely be achieved by astronomical observations; as a result, aggregate spectra consisting of many PAHs are invoked to reproduce astronomical features (220).

For these reasons, many attempts to understand the chemistry of PAHs have focused on the possible formation pathways which proceed through more readily detectable molecules. Much effort has been centered on modeling the formation of small five- and six-membered aromatic rings, and their subsequent reactions with smaller hydrocarbons and nitrogen species to produce PAHs and polycyclic aromatic nitrogen heterocycles (PANHs; (122)). To date, the only interstellar detection of a five or six-membered aromatic ring is benzene (C_6H_6), through the observation of a single weak absorption feature arising from its ν_4 bending mode near 14.85 μm in a handful of sources (37; 73; 132; 148). The lack of a permanent dipole moment, however, precludes the identification of benzene via its rotational transitions.

In this study, we searched for a number of simple aromatic molecules, including several PA(N)Hs and nitriles (R-C≡N), a class of molecules believed to give rise to a common UIR feature at 6.2 μm (112). The astronomical source targeted in these observations was the cold core Taurus Molecular Cloud 1 (TMC-1), which has long been known to display a rich chemistry dominated by unsaturated carbon-chain molecules such as the cyanopolyynes (HC_nN; n = odd) (e.g. (83; 121; 141; 157)). The initial search was performed by construction of velocity-stacked composite-average spectra of twelve target molecules (Figure 3.1; (125)) using existing survey data taken with the Nobeyama 45 m telescope (121). This method enhances the signal-to-noise ratio (SNR) of a potential molecular detection by averaging the signal from multiple transitions of a molecule in velocity space. These composite averages are effective preliminary indicators of a molecule in a source such as TMC-1, where spectral features are narrow (0.3–0.5 km s^{-1}), the line density is relatively low ($\sim$1 line per 200 km s^{-1}), and the molecules occupy a narrow range in local standard of rest (LSR) velocity ($v_{\rm lsr}$ = 5.5–5.9 km s^{-1}) (121). As shown in Figure 3.1, the composite spectra show highly suggestive evidence for benzonitrile in this source. Nevertheless, the observation

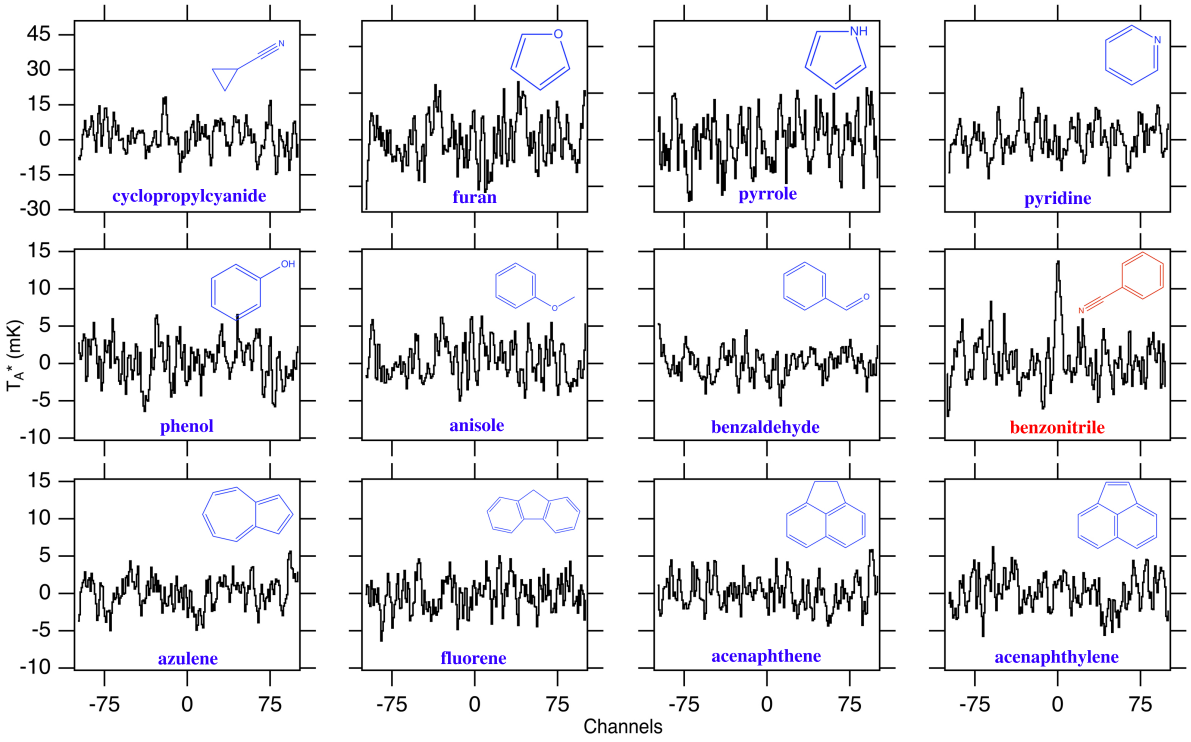

Figure 3.1: **Composite averages of molecules toward TMC-1.** Velocity-stacked composite averages of all transitions of a given molecule with upper state energy (E_U) < 70 K constructed from the entire survey (8.8–50 GHz) of TMC-1 (121). The channel spacing is 20 kHz. If a molecule is present, signal in antenna temperature (T_A^*) would be expected at channel 0. A detectable signal was only present for benzonitrile (red).

of individual transitions is required to establish a firm detection, and to enable the robust determination of the molecular abundance. The sensitivity and spectral resolution of the existing survey observations, however, were insufficient for that task.

Observations

We performed observations with the 100 m Robert C. Byrd Green Bank Telescope to confirm the detection of benzonitrile, by observing nine of its individual rotational transitions, using deep integrations at high spectral resolution. A detailed description of the GBT observations is given in (157). The observations of TMC-1 using the 100 m Robert C. Byrd Green Bank Telescope in Green Bank, West Virginia were centered on right ascension = $04^h41^m42.5^s$, declination = 25°41′27.0″ (J2000 equinox). Pointing observations were conducted every hour; the pointing accuracy is estimated to be within 2″. The beam size varied from 32–40″ across the observed frequency range. The K-band Focal Plane Array (170) was used with the VEGAS spectrometer backend (197) configured to provide

187.5 MHz total bandwidth in each of ten target windows at a 1.4 kHz (0.02 km s^{-1}) spectral resolution. Two observing setups were used, as the VEGAS backend can support at most eight simultaneous frequency windows. Observations were conducted in position-switching mode, using a 1° offset throw, with 120 s of integration at each position and between ∼7.5 and 15 hours of total on-source integration, depending on the frequency window. The resulting spectra were placed on the atmosphere-corrected antenna temperature (T_A*) scale (226). Data reduction was performed using the GBTIDL software package, and archival data of TMC-1 from Project GBT02C_012 (PI: J. Hollis) were included to increase the SNR. The spectra were averaged using a weighting scheme which corrects for the measured system temperature (T_{sys}) during each 240 s on-off position cycle. The spectra were smoothed to a resolution of 5.7 kHz (0.08 km s^{-1}), sufficient to provide ≥4 points across each 0.4 km s^{-1} full-width half-maximum (FWHM). A polynomial fit was used to correct for baseline fluctuations. The final root-mean-square (RMS) noise varied from 2 to 5 mK across the observations. Because the spectral features of other molecules in TMC-1 are so narrow, ^{14}N nuclear hyperfine structure is expected to be partially resolved in benzonitrile's lower rotational transitions. Existing spectral catalogs for benzonitrile in public databases did not contain hyperfine-splitting frequencies, and existing laboratory work at high resolution was limited to measurements below 11 GHz (238). For these reasons, additional transitions of benzonitrile were measured in the laboratory at high resolution between 7 and 29 GHz to ensure the astronomical data could be interpreted [1].

The Nobeyama 45-m observations from 8.8 – 50 GHz were conducted over a period of 13 years from 1984 – 1997, and are described in detail in (121). The RMS noise varied across the survey, but was typically ∼10 mK in 20 kHz channels.

3.2 Results and Analysis

Molecules in TMC-1 are typically well-described by a single excitation temperature between 5 and 10 K (83; 141). Under these conditions, the strongest benzonitrile transitions fall between 20 and 40 GHz. A total of 1.875 GHz of bandwidth was covered to high sensitivity (T_A^* = 2 – 5 mK) between 18 – 23 GHz. In this range, eight of the nine strongest predicted rotational transitions were observed, each with a SNR $\geq$ 3 (Fig. 3.4). For six of these, characteristic ^{14}N nuclear hyperfine splitting is partially or fully resolved for one or more components (Table 4.1). The emission features are best described by a $v_{\rm lsr}$ = 5.83 km s^{-1}, a typical velocity for molecules in this source (121). All other strong transitions between 18 and 23 GHz fell into gaps in the spectral coverage, or in regions where insufficient noise levels were achieved. Taken together, these findings establish the presence of benzonitrile in TMC-1.

[1] Materials and methods are available as supplementary materials on *Science* Online

3.2.1 Column Density Calculations

The overall data analysis procedure follows the general methodology used in previous observations (157; 160). The column density was determined using the formalism of (110):

$$N_T = \frac{Qe^{E_u/T_{ex}}}{\frac{8\pi^3}{3k}\nu S_{ij}\mu^2 g_I} \times \frac{\frac{1}{2}\sqrt{\frac{\pi}{\ln(2)}}\frac{\Delta T_A \Delta V}{\eta_B}}{1-\frac{e^{h\nu/kT_{ex}}-1}{e^{h\nu/kT_{bg}}-1}} \tag{3.1}$$

where N_T is the column density (cm^{-2}), E_u is the upper state energy (K), $\Delta T_A \Delta V$ is integrated line intensity (K cm s^{-1}), T_{ex} is the excitation temperature (K), T_{bg} is the background continuum temperature (2.7 K), ν the transition frequency (Hz), S_{ij} is the intrinsic line strength, μ^2 is the transition dipole moment (Debye), and η_B is the beam efficiency ($\sim$0.92 for the GBT at 20 GHz). An additional factor of g_I has been added to correct for the spin statistical weights (see below). The partition function, Q, is discussed in detail below. We assume that the source fills the beam (see (141)). The column density was calculated using the highest SNR transition that was at least partially hyperfine-resolved, the F = 6–5 and 8–7 components of the $7_{2,5} - 6_{2,4}$ transition; the value matches the observed spectra quite well by visual inspection, and certainly within the uncertainties. An alternative formulation of Equation 4.1, along with a detailed description of the derivations, is given in Mangum & Shirley (149).

Partition Functions

The total partition function Q is given by $Q = Q_{\rm vib} \times Q_{\rm rot}$. The rotational partition function, $Q_{\rm rot}$, is calculated explicitly by direct summation of states using Equation 3.2 (c.f. (81); $Q_{\rm rot}$[7 K] = 480). Here, $\sigma = 1$ for an asymmetric molecule.

$$Q_r = \frac{1}{\sigma}\sum_{J=0}^{J=\infty}\sum_{K=-J}^{K=J}(2J+1)g_I e^{-E_{J,K}/kT_{ex}} \tag{3.2}$$

The value of g_I is found following the definition (81) as given in Equation 3.3.

$$g_I \equiv \frac{g_{nuclear}}{g_n} \tag{3.3}$$

Here, $g_{nuclear}$ arises from the combining the two sets of equivalent nuclei which result in an overall symmetry or asymmetry. The symmetric and asymmetric ($K = \text{even}$ and $K = \text{odd}$) values and the nuclear spin weights are calculated in the final line for benzonitrile ($I_1 = I_2 = \frac{1}{2}$) using (81).

$$\begin{aligned} g^s_{nuclear} &= \psi_{1,sym}\psi_{2,sym} + \psi_{1,asym}\psi_{2,asym} \\ &= (I_1+1)(2I_1+1)(I_2+1)(2I_2+1) + I_1(2I_1+1)I_2(2I_2+1) \\ &= 10 \end{aligned} \tag{3.4}$$

$$\begin{aligned} g^a_{nuclear} &= \psi_{1,asym}\psi_{2,sym} + \psi_{1,sym}\psi_{2,asym} \\ &= (I_1+1)(2I_1+1)I_2(2I_2+1) + I_1(2I_1+1)(I_2+1)(2I_2+1) \\ &= 6 \end{aligned} \tag{3.5}$$

To solve for g_I, $g_{nuclear}$ must be divided by g_n given by Equation 3.6, which for benzonitrile is 16. Thus, the final values for g_I requires division by $(2I+1)^4$. That makes $g_{I,even} = 5/8$ and $g_{I,odd} = 3/8$.

$$g_n = \prod_i \prod_n (2I_i + 1) \tag{3.6}$$

We have calculated the energies of the vibrational states of benzonitrile at the WB97XD/6-311++G(d,p) level of theory and basis set to determine their possible contribution to the overall partition function at these temperatures. The vibrational contribution is given by Equation 3.7.

$$Q(T)_{vib} = \prod_{i=1}^{3N-6} \frac{1}{1 - e^{-E_i/kT}} \tag{3.7}$$

The lowest energy levels are at 162 cm^{-1} (233 K) and 184 cm^{-1} (265 K). At these temperatures, the vibrational contribution to the partition function is less than 10^{-14}. Indeed, the vibrational partition function does not contribute at the 1% level until $T_{\rm ex}$ ∼38 K.

Uncertainties

We estimate an overall uncertainty of 40% in the derived column density for benzonitrile. This is based on a number of contributing factors, enumerated below, and added in quadrature:

1. A 30% uncertainty arising from the absolute flux uncertainty in the observations is assumed. This incorporates the 20% uncertainty in the strongest transitions arising from the noise of the observations (SNR∼5), and a (conservative) 20% calibration uncertainty, added in quadrature.

2. A 5–10% uncertainty from the Gaussian fits to the line profiles.

3. A 20% contribution arising from the accuracy of the linewidth used (0.40 km s^{-1}) compared to the resolution element of the observations (∼0.08 km s^{-1}).

4. A 20% contribution arising from the choice of excitation temperature (7 K) compared to the lower and higher ends of the range commonly seen in the source (5–10 K).

We further note that the uncertainties given in Table 4.1 are the purely-statistical 1σ standard deviation uncertainty in the Gaussian fitting routine used to determine the peak value of T_A^* (∼5–10% as noted above). The SNR is then calculated by simply dividing this peak value by the RMS of the data in that region. The actual uncertainty in the peak is significantly higher, due to the other contributions noted above.

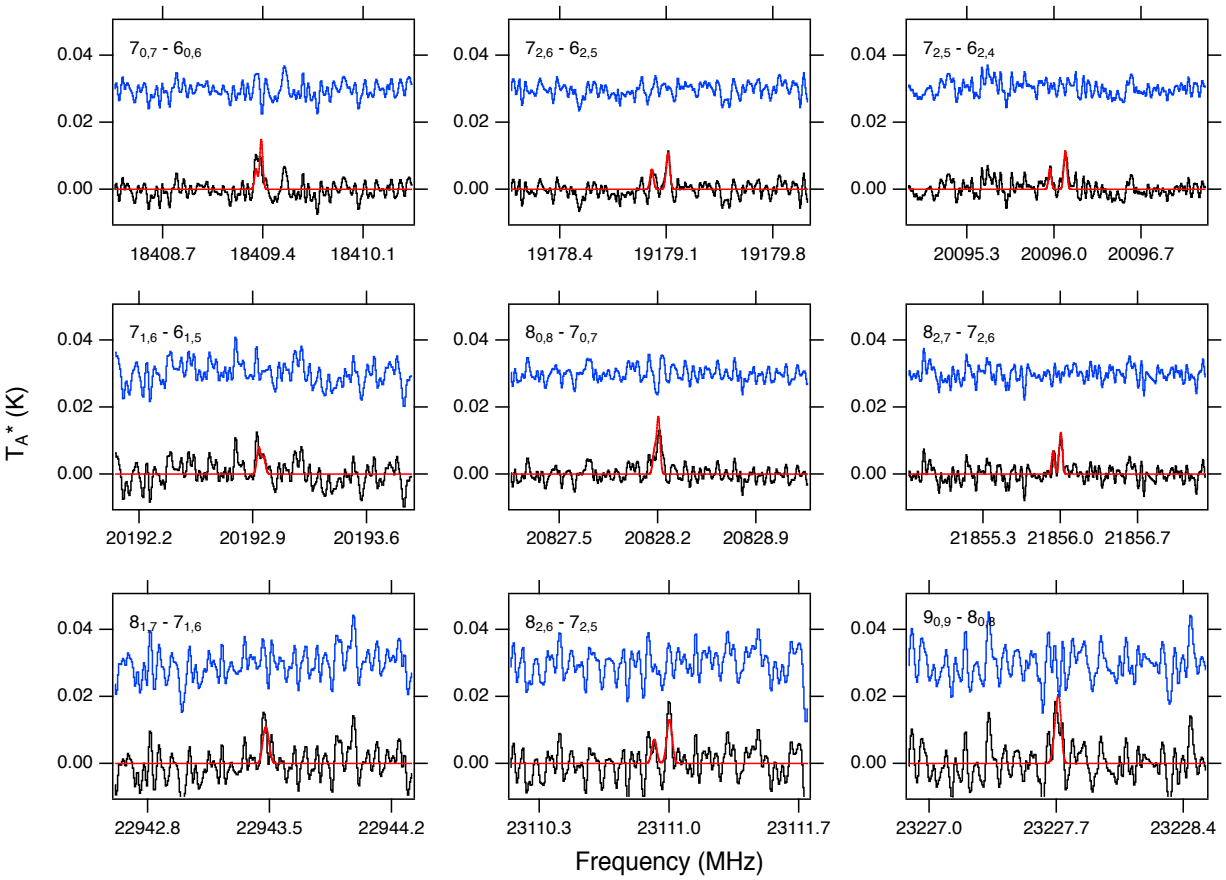

Figure 3.2: **Fit residuals.** Residuals for the nine detected transitions are shown in the upper blue tracer, and are consistent with the baseline noise level of the observations in each window. All other parameters are the same as in Figure 3.4.

Residuals and Goodness of Fit

The residuals for the nine detected transitions are shown in Figure 3.2, and are consistent with the baseline noise level of the observations in each window. Figure 3.3 shows the comparison of the model spectra to the observed spectra on a zoomed-in scale to show greater detail for the four transitions with a well-resolved hyperfine component. The $8_{2,7} - 7_{2,6}$ $F = 8 - 7$ component at 21855.93 MHz is the poorest agreement in line-center position of any detected transition. The difference is 7.2(4) kHz, equivalent to 1.25(5) channel widths. Given the SNR of the line, and the agreement of every other transition, this is likely a simple issue of the noise slightly affecting the line center position in the Gaussian fit.

Composite Averages

The process of building a composite average (CA) used in this work consists of the following steps:

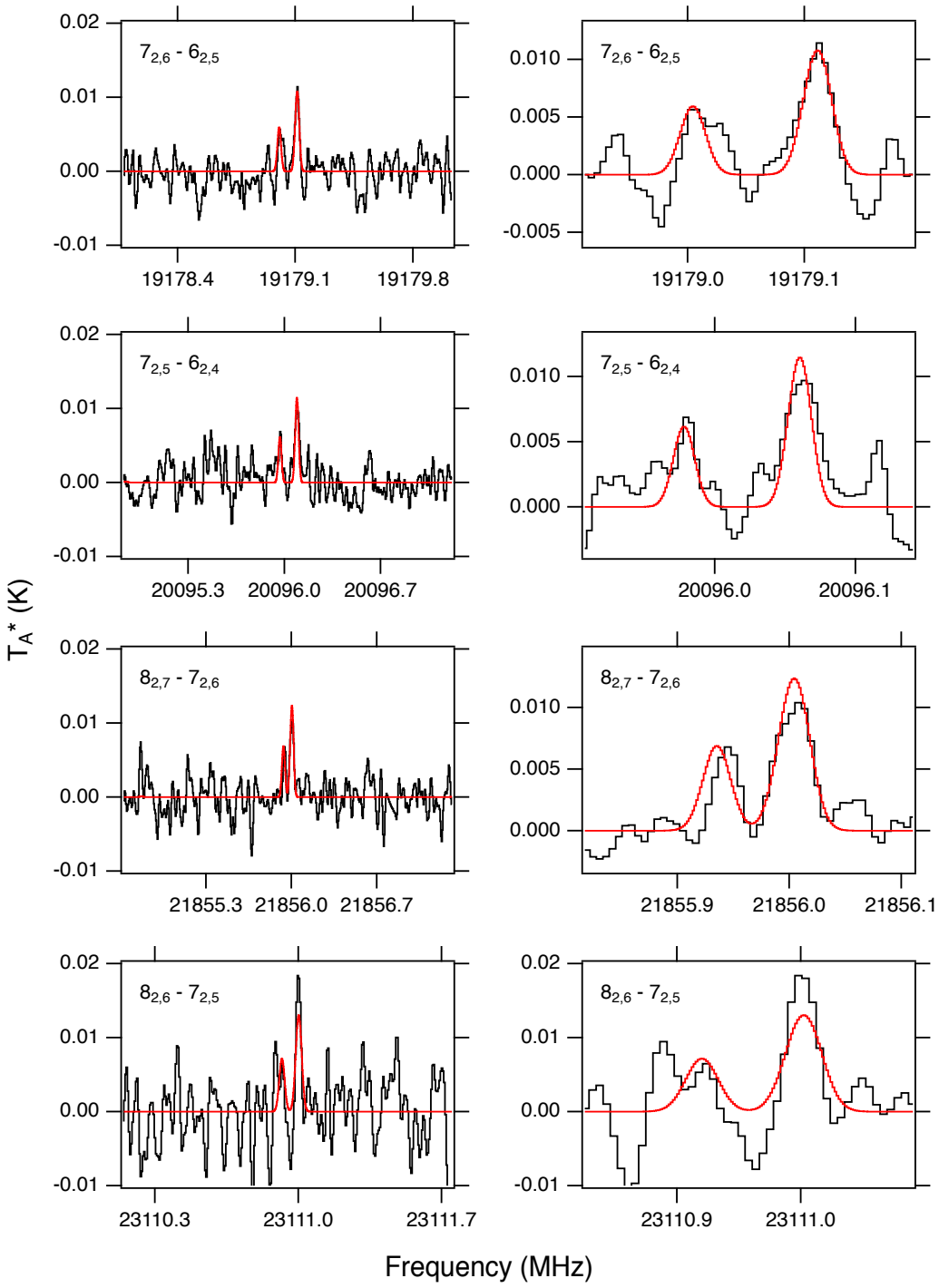

Figure 3.3: **Detailed spectral comparisons.** Comparison of the model spectra (red) to the observed spectra (black) on a zoomed-in scale to show detail on the four detected transitions with a well-resolved hyperfine component.

1. Transition frequencies for target molecules are determined, and the broadband observational spectra are trimmed into narrow-band elementary spectra centered on those frequencies.

2. A single excitation temperature is assumed (7 K in the case of TMC-1) and the strongest predicted line with observational coverage is set as the reference line.

3. Each elementary spectrum is multiplied by the ratio of the brightness temperatures of the given transition relative to that of the reference line. As a result, the brightness temperatures of all lines are normalized, while the RMS noise of the elementary spectra (except for the reference spectrum) increases.

4. Finally, the elementary spectra are averaged together using weights inversely proportional to their RMS noise levels, and the final CA is obtained.

Final Results of Column Density Calculation

A joint analysis of all the lines yields a total column density N_T = 4 × 10^{11} cm^{-2} (Sci), about twenty times less that of HC_7N (1.1 × 10^{13} cm^{-2}; (141)), an unsaturated linear cyanopolyyne with the same carbon and nitrogen composition as benzonitrile, in the same source. Because the upper state energies of the observed transitions span only a narrow energy range (3.6 to 5.7 K), the excitation temperature could not be constrained from these observations. Our analysis therefore assumed $T_{\rm ex}$ = 7 K, in the middle of the range of 5–10 K, derived from other molecules in this source (83; 141). We also constrained the linewidth to 0.4 km s^{-1}, based on the three fully-resolved hyperfine components. Although these components are some of the lowest SNR features, and our data are limited by the resolution of the observations (0.08 km s^{-1}), this linewidth is consistent with that seen previously for other molecules in this source (121). Simulated spectra under these conditions are shown in Fig. 3.4, and are in agreement with the observations.

3.2.2 Astrochemical Modeling of Benzonitrile

The pathways leading to the formation of benzonitrile at low temperature and in low density environments have not been studied in detail. Perhaps the only promising astrochemically-relevant formation pathway discussed in the literature is the neutral-neutral reaction

$$\mathrm{CN} + c\text{-}\mathrm{C_6H_6} \rightarrow c\text{-}\mathrm{C_6H_5CN} + \mathrm{H}. \tag{3.8}$$

This barrierless, exothermic reaction has been considered previously (222; 239). In an effort to determine the contribution of Reaction 3.8 to the observed abundance of benzonitrile in TMC-1, we have modified the Kinetic Database for Astrochemistry (KIDA) gas-phase reaction network (231) to include this reaction, as well as destruction pathways from photons, ions, and depletion onto grains (Sci). This network was then combined with the `NAUTILUS-1.1` modeling code (199) assuming elemental abundances and physical conditions appropriate for TMC-1 (106). A number of additional gas-phase formation routes

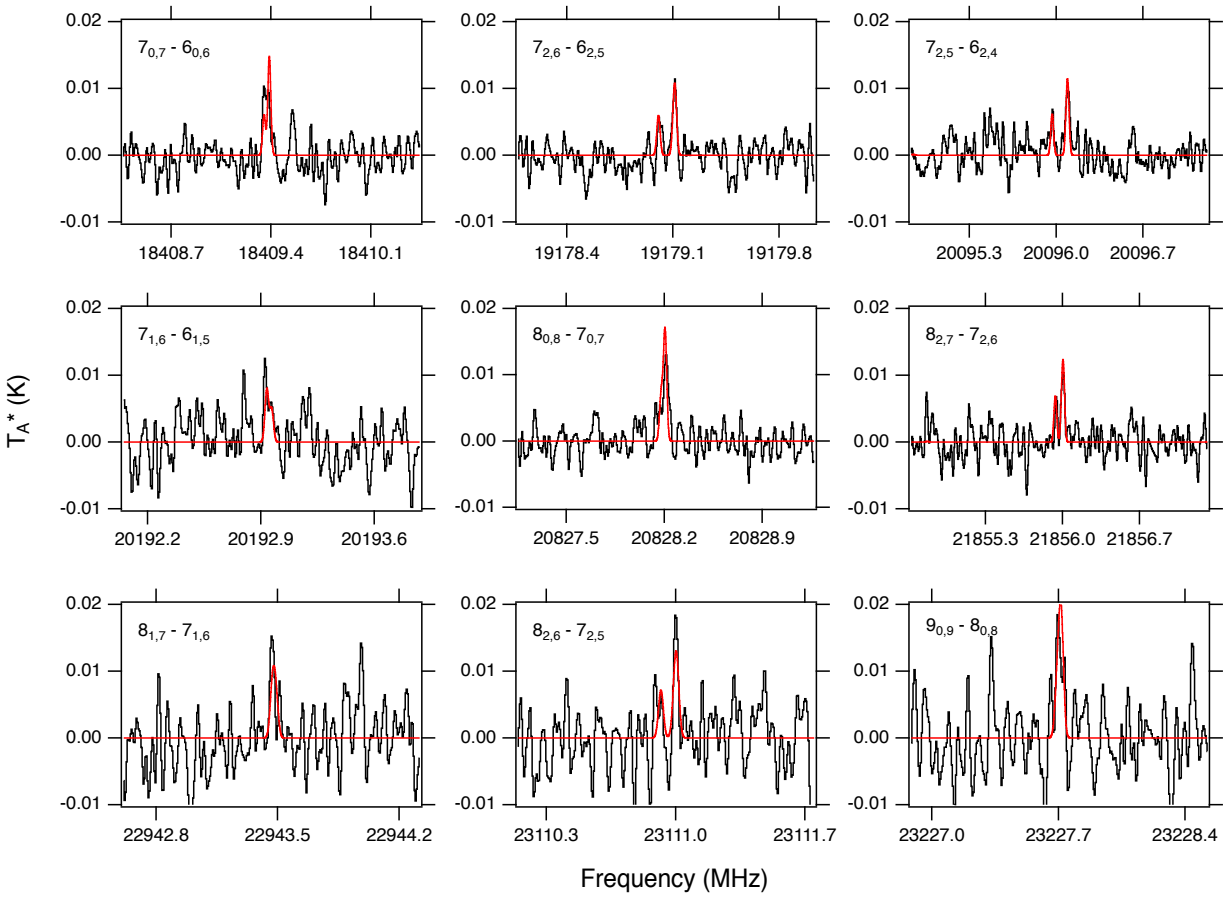

Figure 3.4: **Detected emission lines of benzonitrile in TMC-1.** Observational spectra are shown in black smoothed to a resolution of 5.7 kHz (0.08 km s^{-1}) and shifted to a $v_{\rm lsr}$ = 5.83 km s^{-1}. A simulated spectrum of benzonitrile, 0.4 km s^{-1} linewidth, N_T = 4 $\times$ 10^{11} cm^{-2}, and $T_{\rm ex}$ = 7 K is overlaid in red (Sci). Rotational quantum numbers are displayed in the upper left of each panel. The four transitions with well-resolved hyperfine structure are shown on an expanded frequency axis in (Sci).

Table 3.1: **Detected benzonitrile transitions.** Quantum numbers, frequencies, upper state energies (E_U), line strengths ($S_{ij}\mu^2$), observed intensities (ΔT_A^*), and signal-to-noise ratio of detected benzonitrile transitions. Statistical uncertainties (1σ), derived from the best-fitting constants in (Sci) are given in parentheses in units of the last significant digit.

Transition		Frequency	E_U	$S_{ij}\mu^2$	$\Delta T_A^{*\dagger}$	
$J'_{K_a,K_c} - J''_{K_a,K_c}$	$F' - F''$	(MHz)	(K)	(Debye^2)	(mK)	Signal-to-Noise
$7_{0,7} - 6_{0,6}$	$6-5$	18409.3490(2)	3.61	39.5		
	$8-7$	18409.3840(2)	3.61	52.9	10.3(8)^b	4.4
	$7-6$	18409.3879(2)	3.61	45.7		
$7_{2,6} - 6_{2,5}$	$7-6$	19179.0017(2)	4.52	42.4	5.4(5)	2.7
	$6-5$	19179.1027(2)	4.52	36.6	10.6(5)^b	5.4
	$8-7$	19179.1128(2)	4.52	49.1		
$7_{2,5} - 6_{2,4}$	$7-6$	20095.9645(2)	4.62	42.5	6.6(5)	3.3
	$6-5$	20096.0824(2)	4.62	36.7	10.0(2)^b	4.9
	$8-7$	20096.0917(2)	4.62	49.2		
$7_{1,6} - 6_{1,5}$	$6-5$	20192.9325(2)	4.11	39.0		
	$7-6$	20192.9342(2)	4.11	45.1	8(1)^b	2.1
	$8-7$	20192.9632(2)	4.11	52.2		
$8_{0,8} - 7_{0,7}$	$7-6$	20828.1746(2)	3.20	46.2		
	$9-8$	20828.2012(2)	3.20	59.6	11.7(9)^b	5.9
	$8-7$	20828.2045(2)	3.20	52.5		
$8_{2,7} - 7_{2,6}$	$8-7$	21855.9322(3)	5.57	49.7	7.1(4)	3.1
	$7-6$	21855.9944(3)	5.57	43.8	10.7(5)^b	4.7
	$9-8$	21856.0064(3)	5.57	56.4		
$8_{1,7} - 7_{1,6}$	$7-6$	22943.4640(3)	5.21	45.8		
	$8-7$	22943.4729(3)	5.21	52.0	16.2(8)^b	3.2
	$9-8$	22943.4885(3)	5.21	59.1		
$8_{2,6} - 7_{2,5}$	$8-7$	23110.9171(3)	5.73	49.9	6.2(9)	1.2
	$7-6$	23110.9923(3)	5.73	43.9	19.6(9)^b	3.8
	$9-8$	23111.0042(3)	5.73	56.7		
$9_{0,9} - 8_{0,8}$	$8-7$	23227.6903(3)	5.72	52.9		
	$10-9$	23227.7105(3)	5.72	66.3	16(2)^b	3.3
	$9-8$	23227.7127(3)	5.72	59.3		

†Uncertainty in the Gaussian fit. A conservative 30% uncertainty in the absolute flux calibrated value is assumed (Sci).

^{b}Indicates blended hyperfine components; ΔT_A^* is the peak value of the observed feature.

for the precursor benzene were also considered, and included in the modified network (Sci). A column density of H_2 = 10^{22} cm^{-2} (83) was used to convert from modeled abundances to column densities to compare with observations. Figure 4.3 shows the derived column densities and those predicted by the model for benzonitrile, benzene, CN, and the cyanopolyynes HC_3N, HC_5N, HC_7N, and HC_9N. While the calculated column densities of most of the cyanopolyynes agree with observational results within a factor of two, the predicted benzonitrile column density is smaller than the derived value by nearly a factor of four.

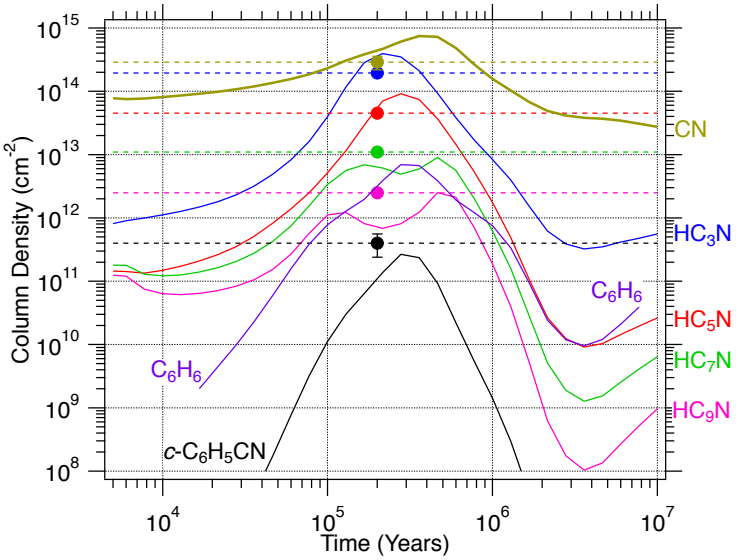

Figure 3.5: **Chemical model of TMC-1.** Results of a three-phase astrochemical model, updated to include the benzonitrile formation pathway given in Reaction 3.8. The model gas-phase column densities as a function of time are given as solid, colored lines. Column densities of benzonitrile, cyanopolyynes, and CN derived from observations are shown as dots with dashed horizontal lines (from top to bottom: CN, HC_3N, HC_5N, HC_7N, HC_9N, and benzonitrile (54; 141)). The derived column densities are plotted at the chemical age of TMC-1 ($\sim 2 \times 10^5$ yrs; (106)).

Benzene Formation Chemistry

A number of formation pathways have been proposed for the key precursor species, benzene, in interstellar regions. One of the first is the dissociative recombination reaction (156):

$$c\text{-}C_6H_7^+ + e^- \rightarrow c\text{-}C_6H_6 + H \tag{3.9}$$

which is the main formation route for benzene in the KIDA network. Another production pathway that could occur under interstellar conditions is the neutral-neutral reaction between the ethynyl radical and 1,3-butadiene (119):

$$C_2H + H_2CCHCHCH_2 \rightarrow c\text{-}C_6H_6 + H. \quad (3.10)$$

This reaction satisfies the typical requirement for gas-phase chemistry in cold cores such as TMC-1 since it is thought to be barrierless, exothermic, and can occur on a single-collision basis. Given those characteristics which are ideal for interstellar gas-phase chemistry, we have added this reaction, with a rate coefficient of $\sim 3 \times 10^{-10}$ cm^3 s^{-1} (c.f. (119)), to our modified version of the KIDA 2014 reaction network (231) to which we have previously added reactions of the HC$_n$O ($n = 3 - 7$) family of molecules (157).

There is another formation route for benzene that has been previously studied in the context of combustion chemistry (80; 167) involving the reaction between two propargyl radicals:

$$C_3H_3 + C_3H_3 \rightarrow c\text{-}C_6H_6^* \rightarrow c\text{-}C_6H_5 + H. \quad (3.11)$$

Here, the benzene is produced in an unstable excited state and will dissociate into atomic hydrogen and the phenyl radical unless it is stabilized radiatively or via collision with a third-body. However, three-body collisions in molecular clouds occur on timescales greater than the lifetime of the cloud (123). Moreover the rate coefficient for the radiative stabilization of the C_6H_6 product is estimated to be several orders of magnitude slower than its dissociation rate coefficient (119). Thus, reaction (3.11) is unlikely to contribute to the abundance of benzene in a cold core such as TMC-1.

The reported difference in the observed and simulated benzonitrile column densities may be explained by other formation routes for benzene, benzonitrile, or both that are not considered in our model. For instance, experiments have found that benzene can be formed in electron-irradiated acetylene ices (243). In astrochemical models, the addition of cosmic ray driven irradiation chemistry in the solid phase has been found to improve agreement between observational and theoretical abundances for other large interstellar molecules (1), although for such grain-surface processes to contribute to gas-phase abundances there must exist efficient non-thermal desorption mechanisms. Recent theoretical and experimental work suggests that interactions between cosmic rays and grain surfaces could result in the liberation of solid-phase species into the gas phase via processes that are viable in cold cores such as TMC-1 (193).

Benzene is also known to be produced in irradiated acetylene gas (69). Radiation chemistry differs from photochemistry in a number of ways (237) and may be a viable formation pathway for aromatic and PAH molecules as a result of their increased photostability (relative to simpler organics (118)). However, there is insufficient theoretical and experimental work to include such pathways in our model. Previous work also suggests a possible connection between benzonitrile and the cyanopolyynes (141) . That work showed a sharp decrease in the calculated abundance of $HC_{11}N$ relative to the abundance trend of the $n(\mathrm{odd}) = 3 - 9$ cyanopolyynes, possibly due to cyclization processes for HC$_n$N molecules which could eventually lead to functionalized aromatics such as benzonitrile.

3.3 Further Discussion

We also consider the possibility that benzonitrile itself may be a contributor to the UIR bands. The vibrational spectrum of benzonitrile has been studied in the infrared, both experimentally (84) and theoretically (55), but it does not appear in spectral databases (25), and it is not commonly considered as a potential UIR carrier. Nevertheless, the interstellar IR emission features at 3.3 μm (C–H aromatic stretch) and 4.48 μm (C$\equiv$N stretch) are both in agreement with very strong IR modes of benzonitrile (55), thus making it a potential carrier in its own right, as well as a likely precursor to polyaromatic species.

3.4 Conclusions

In summary, we have detected the aromatic molecule benzonitrile in TMC-1, using radio astronomy to probe this class of molecules. These species may be either direct contributors to the UIR bands, or precursors to the carriers themselves.

3.5 Acknowledgements

Support for B.A.M. was provided by NASA through Hubble Fellowship grant #HST-HF2-51396 awarded by the Space Telescope Science Institute, which is operated by the Association of Universities for Research in Astronomy, Inc., for NASA, under contract NAS5-26555. A.M.B. is a Grote Reber Fellow, and support for this work was provided by the NSF through the Grote Reber Fellowship Program administered by Associated Universities, Inc./National Radio Astronomy Observatory. S.V.K. acknowledges support from Basic Research Program P-7 of the Presidium of the Russian Academy of Sciences. E.H. and C.N.S. acknowledge support from the National Science Foundation. M.C.M. acknowledges support from NSF grant AST-1615847. The authors thank G.A. Blake for a critical reading of the manuscript and J. Mangum for helpful discussions. The National Radio Astronomy Observatory is a facility of the National Science Foundation operated under cooperative agreement by Associated Universities, Inc. The Green Bank Observatory is a facility of the National Science Foundation operated under cooperative agreement by Associated Universities, Inc.

The Nobeyama observations are archived at `www.cv.nrao.edu/PRIMOS`, and the GBT observations at `https://archive.nrao.edu/archive/advquery.jsp` under IDs AGBT02C_012, AGBT17A_164, and AGBT17A_434. Laboratory data are tabulated in the Supplementary Material. The modifications we applied to KIDA and the output of our chemical model are at `doi:10.18130/V3/4IFDBP`.

CHAPTER 4

DETECTION OF INTERSTELLAR HC_5O IN TMC-1 WITH THE GREEN BANK TELESCOPE

The following chapter is primarily reproduced from McGuire, B. A.; Burkhardt, A. M.; Shingledecker, C. N.; Kalenskii, S. V.; Herbst, Eric; Remijan, A. J.; McCarthy, M. C. The Astrophysical Journal Letters ***2017****, 843, L28.*

We report the detection of the carbon-chain radical HC_5O for the first time in the interstellar medium toward the dark cloud TMC-1 using the 100 m Green Bank Telescope. We observe four hyperfine components of this radical in the $J = 17/2 \rightarrow 15/2$ rotational transition that originates from the $^2\Pi_{1/2}$ fine structure level of its ground state, and calculate an abundance of n/n_{H_2} = 1.7×10^{-10}, assuming an excitation temperature of $T_{ex} = 7$ K. No indication of HC_3O, HC_4O, HC_6O, is found in these or archival observations of the source, while we report tentative evidence for HC_7O. We compare calculated upper limits, and the abundance of HC_5O to predictions based on (1) the abundance trend of the analogous HC_nN family in TMC-1 and (2) a gas-grain chemical model. We find that the gas-grain chemical model well reproduces the observed abundance of HC_5O, as well as the upper limits of HC_3O, HC_6O, and HC_7O, but HC_4O is over produced. The prospects for astronomical detection of both shorter and longer HC_nO chains are discussed.

4.1 Introduction

Observations of complex chemistry occurring outside the typical hot core environments are critical for understanding the underlying reaction mechanisms and chemical evolutionary processes at work in the larger interstellar medium (ISM). One of the prototypical sources for such investigations is the dark cloud TMC-1, which contains a rich chemical inventory distinct from star-forming regions. Indeed, while most hot core sources display a wealth of saturated organic molecules[1] such as methanol (CH_3OH), ethanol (CH_3CH_2OH), dimethyl ether (CH_3OCH_3), and ethyl cyanide (CH_3CH_2CN) (173), the inventory in TMC-1 is heavily weighted toward *un*saturated species such as HC_nN (n = 1−9) (140), C_nH

[1]Those species which have few double and triple carbon-carbon bonds and instead use these electrons to bind hydrogen atoms.

(n = 3–6), C_2S, C_3S, and C_3O (121). Since hydrogenation reactions are much more efficient on grains (e.g. CO $\rightarrow$ CH_3OH), saturated species will tend to be predominantly found on grain surfaces at the low temperatures within cold cores ($\leq$20 K) (38; 77). Therefore, gas-phase reactions (such as carbon insertion processes) that proceed rapidly at low temperature and density will tend to dominate the chemistry in these regions, resulting in the efficient production of unsaturated hydrocarbons and other carbon-chain molecules (98).

Because cold cores such as TMC-1 are at an early stage of stellar evolution, their relatively simple physical history and well-defined conditions allow one to model and test chemical pathways, often in great detail. For species that are observed in both cold and hot cores, it is then possible to study the effects of the vastly differing physical conditions (temperature, density, radiation field, etc.) on the chemical evolution. Despite the relative dearth of complex organic molecules, another important characteristic of cold cores is the ease with which new molecular species can be unambiguously identified, especially at cm-wavelengths, due their cold excitation conditions, narrow linewidths, and uncrowded ($\sim$1 line per 200 km s^{-1}) spectrum. For these reasons, it is not surprising that TMC-1 is one of the most well-studied astrochemical sources outside of hot cores and the carbon-star IRC+10216; several dozen new molecular detections have been reported there over the past several decades (see Kaifu et al. (121) for an extensive review).

We have recently conducted high-sensitivity observations of TMC-1 in search of a number of new molecules. Here, we report the first of several new detections from this study: the carbon-chain HC_5O radical via observation of four hyperfine components in the $J = 17/2 \rightarrow 15/2$ rotational transition. The observations are presented in §4.2, a review of the laboratory spectroscopy of HC_5O in §4.3, the results and analysis in §5.3, and a discussion of the astrochemical implications and future study is given in §5.4.

4.2 Observations

The observations were conducted over eight observing sessions from 2017 February to 2017 June using the 100 m Robert C. Byrd Green Bank Telescope in Green Bank, WV. The observations of TMC-1 were centered on α(J2000) = $04^h41^m42.5^s$, δ(J2000) = $25^\circ41'27.0''$. Pointing observations were conducted every hour; the pointing accuracy is estimated to be within 2″. The K-band Focal Plane Array was used with the VEGAS spectrometer backend configured to provide 187.5 MHz total bandwidth in each of ten spectrometer banks at a 1.4 kHz (0.02 km s^{-1}) spectral resolution. These extremely high-resolution observations were necessary to resolve the $\sim$0.3 km s^{-1} FWHM spectral features typical of TMC-1 (121). The total spectral coverage was 1875 MHz in ten discontinuous 187.5 MHz windows within the range of 18 to 24 GHz.

Observations were conducted in position-switching mode, using a 1° offset throw, with 120 s of integration at each position and between $\sim$7.5 and 15 hours of total on-source integration depending on the frequency window. The resulting spectra were placed on the atmosphere-corrected T_A* scale (226). Data reduction was performed using the GBTIDL software package. The spectra were averaged using a weighting scheme which corrects for

Table 4.1: Measured and observed frequencies of HC_5O transitions covered in this work as well as pertinent line parameters.

$J' \rightarrow J''$	$F' \rightarrow F''$	e/f	Frequency (meas.)[a] (MHz)	Frequency (obs.)[b] (MHz)	Diff. (kHz)	ΔT_A^c (mK)	ΔV^d (km s^{-1})	$S_{ij}\mu^2$ (Debye^2)	E_u (K)
$17/2 \rightarrow 15/2$	$9 \rightarrow 8$	e	21941.846	21941.848	-1	13.0	0.30	41.7	5.017
	$8 \rightarrow 7$	e	21941.977	21941.980	-2	13.6	0.27	37.0	5.018
	$9 \rightarrow 8$	f	21945.232	21945.231	2	15.1	0.26	41.7	5.019
	$8 \rightarrow 7$	f	21945.370	21945.370	1	11.0	0.33	37.0	5.018

[a]Mohamed et al. (169); 1σ experimental uncertainty is ∼2 kHz.
[b]Gaussian fit to line at v_{lsr} = 5.64 km s^{-1}. 1σ uncertainty from Gaussian fit is ∼0.5 kHz. Given the SNR of the detected lines (∼5.4) and the linewidth, we estimate the uncertainty in the observed line centers to be ∼3.7 kHz.
[c]We estimate a conservative uncertainty of 30% in the overall flux calibration.
[d]Uncertainty in Gaussian fit is ∼0.01 km s^{-1}.

the measured value of T_{sys} during each 240 s ON-OFF cycle. The spectra were smoothed to a resolution of 5.7 kHz (0.08 km s^{-1}), sufficient to provide ≥3 points across each 0.3 km s^{-1} FWHM. A polynomial fit was used to correct for baseline fluctuations. The final RMS noise in the HC_5O window examined here was 2.4 mK.

4.3 Spectroscopy

The pure rotational spectrum of HC_5O was precisely measured between 6 and 26 GHz by Mohamed et al. (169). This radical was produced in an electrical discharge of HC_4H + CO, and its spectrum measured using a Balle-Flygare cavity Fourier-Transform microwave spectrometer (10). Rest frequencies were determined to better than 1 ppm (2 kHz; 0.03 km s^{-1} at 20 GHz). The ground electronic state of HC_5O is $^2\Pi_r$ with the $^2\Pi_{1/2}$ fine structure level lying lowest in energy, many tens of K below the $^2\Pi_{3/2}$ level. At high spectral resolution, its rotational spectrum displays well-resolved Λ-doubling but more closely spaced hydrogen hyperfine splitting. At the low rotational temperature characteristic of TMC-1, only transitions from the lower $^2\Pi_{1/2}$ ladder are significantly populated; those that fall within the frequency coverage of the observations are given in Table 4.1. Of the ten spectrometer windows used in these observations, only one, covering the range of 21766 to 21953 MHz contained HC_5O transitions.

4.4 Results and Analysis

We observe emission from four hyperfine components of HC_5O in the $J = 17/2 \rightarrow 15/2$ rotational transition at $v_{lsr} = 5.64$ km s^{-1}, typical of molecules in this source (121); the parameters of the observed lines are given in Table 4.1 and the spectra toward TMC-1 are shown in Figure 4.1. Although these lines originate from a single J rotational level, taken together, the Λ-doubling and hydrogen hyperfine splitting provide a unique spectroscopic signature. Given the very low line density of the spectra and the coincidence of the line centers to less than the experimental uncertainties, a mis-identification of these lines is extremely unlikely from these data alone.

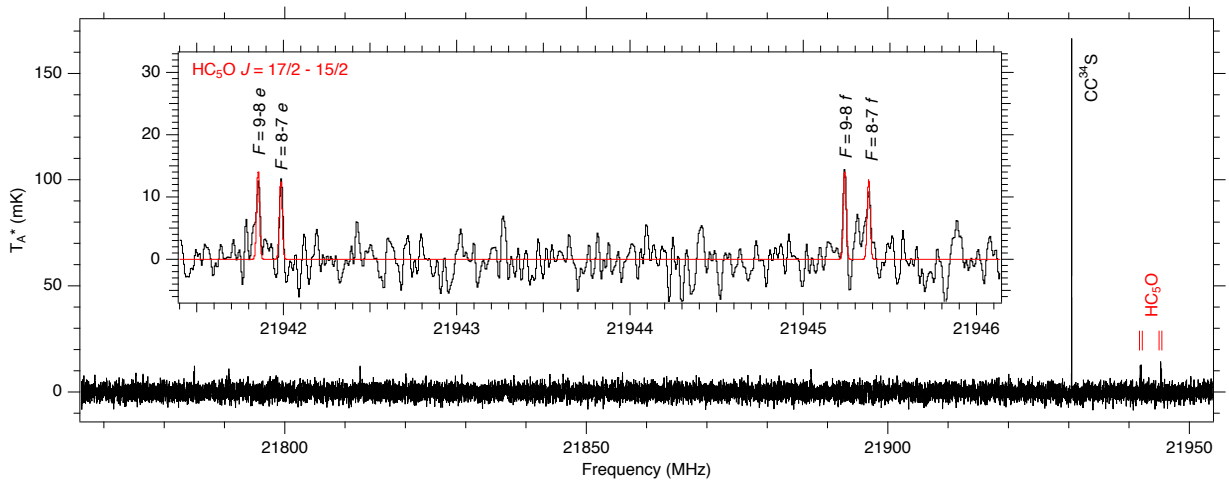

Figure 4.1: Spectrum (black) toward TMC-1 in the frequency range containing the HC_5O transitions. The inset provides an expanded view of the HC_5O features. A simulation of the radical at T_{ex} = 7 K from the laboratory work of Mohamed et al. (169), at a linewidth of 0.26 km s^{-1} and a v_{lsr} = 5.64 km s^{-1} is overlaid in red. The quantum numbers for each observed transition are labeled.

Molecular emission in TMC-1 has been shown to be well-modeled by a single excitation temperature (189), typically T_{ex} = 7–10 K. Because of the negligible spread (∼0.1%) in upper-state energies probed by the observed transitions, we assume a T_{ex} = 7 K for our abundance determination. The column density of HC_5O was determined using the formalism of Hollis et al. (110), given in Eq. 4.1,

$$N_T = \frac{Qe^{E_u/T_{ex}}}{\frac{8\pi^3}{3k}\nu S\mu^2} \times \frac{\frac{1}{2}\sqrt{\frac{\pi}{\ln(2)}}\frac{\Delta T_A \Delta V}{\eta_B}}{1 - \frac{e^{h\nu/kT_{ex}}-1}{e^{h\nu/kT_{bg}}-1}} \tag{4.1}$$

where N_T is the column density (cm^{-2}), E_u is the upper state energy (K), $\Delta T_A \Delta V$ is integrated line intensity (K cm s^{-1}), T_{ex} is the excitation temperature (K), T_{bg} is the background continuum temperature (2.7 K), ν the transition frequency (Hz), S is the intrinsic line strength, μ^2 is the transition dipole moment (Debye)[2], and η_B is the beam efficiency (∼0.7 for the GBT at 20 GHz). The rotational partition function, Q, is calculated explicitly by direct summation of states (Q[7 K] = 491). We assume that the source fills the beam (see Loomis et al. (140) for a detailed discussion).

4.4.1 HC_5O

For HC_5O, we calculate a column density of 1.7×10^{12} cm^{-2} at T_{ex} = 7 K. Assuming the HC_5O is co-spatial with previous estimates of H_2 in the region [$N(H_2) = 10^{22}$ cm^{-2}; Gratier et al. (83)], this corresponds to an abundance of $n/n_{H_2} = 1.7 \times 10^{-10}$.

[2]These units must be properly converted to Joules·cm^3 to give N_T in cm^{-2}.

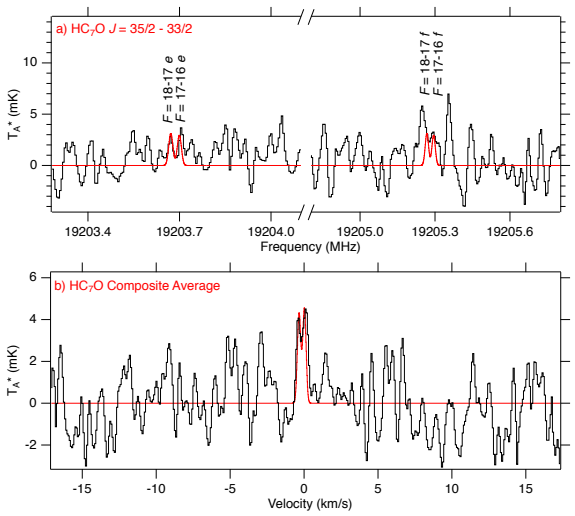

Figure 4.2: A) observational spectra coincident with the $J = 35/2 - 33/2$ rotational transition of HC_7O in black, with the HC_7O transitions overlaid in red. This is the lowest RMS noise window containing an HC_7O line, and there is no detection of HC_7O. B) Composite average of the $J = 35/2 - 33/2$ and $J = 37/2 - 35/2$ transitions of HC_7O; because the hydrogen hyperfine splitting is not fully resolved, the average was performed using the central frequency, preserving the partial splitting. The SNR of the (tentative) composite line is $\sim$3.

4.4.2 HC_3O, HC_4O, HC_6O, HC_7O

We have also searched our observations, and those of Kaifu et al. (121), for other members of the HC_nO (n = 3–7) family of oxygen-terminated hydrocarbon free radicals. At present, our observations only cover transitions of HC_7O , and no detection is seen in individual transitions (Fig. 4.2)a. If the four Λ-doubling components of the two J transitions covered in our observations are stacked in velocity space using a composite average approach (124), some tentative indication of HC_7O is seen, suggesting the individual transitions remain at or just below our detection limit (Fig. 4.2b).

We do not find any definitive evidence in our survey, or that of Kaifu et al. (121), for signal arising from any of the other HC_nO radicals. Assuming the same $T_{ex} = 7$ K as for HC_5O, we have calculated upper limits to the column densities using the strongest transition in the available frequency coverage (Table 4.2). Mohamed et al. (169) lists the calculated dipole moments for the HC_nO radicals discussed here, all of which are approximately 2 Debye.

4.5 Discussion

The detection of HC_5O, combined with the non-detections of HC_3O and HC_7O, raises the question of whether the abundance and upper limits agree with the chemistry thought

Table 4.2: Measured column densities and upper limits for the HC_nO (n = 3–7) family compared to the predicted values from the HC_nN family abundance trend (§4.5.1) and from the chemical model (§4.5.3). Details of the transition used for the calculation, the assumed maximum brightness temperature, and the laboratory reference for the spectroscopy are also given.

	Column Density (10^{11} cm^{-2})						
Molecule	Observed	HC_nN	Model	Transition	ν (MHz)	T_A (mK)	Ref.
HC_3O	< 3	200	0.5	$N_{k_a,k_c} = 5_{0,5} \rightarrow 4_{0,4}$, $J = 11/2 \rightarrow 9/2$, $F = 6 \rightarrow 5$	45327.7	10†	1,2,3
HC_4O	< 6	-	220	$N_J = 8_{17/2} \rightarrow 7_{15/2}$, $F = 9 \rightarrow 8$	36494.6	10†	4
HC_5O	17	17*	16	See Table 4.1			5
HC_6O	< 10	-	0.0003	$J = 27/2 \rightarrow 25/2$, $F = 14 \rightarrow 13$, f-parity	22165.2	10†	5
HC_7O	≤ 5	10	5	$J = 35/2 \rightarrow 33/2$	19204‡	2.4	5
				$J = 37/2 \rightarrow 35/2$	20302‡	3.7	5

*Fixed to observed value.
†Kaifu et al. (121). Accessible at www.cv.nrao.edu/SLiSE.
‡These transitions display Λ-doubling and hyperfine splitting analogous to HC_5O. For simplicity, a central frequency for these splittings is given here; individual frequencies are available in Mohamed et al. (169).
References. [1] Cooksy et al. (51) [2] Chen et al. (40) [3] Cooksy et al. (50) [4] Kohguchi et al. (131) [5] Mohamed et al. (169)

to be operative in the region, and if these closely-related species might be detectable in follow-up observations. To the former point, there are two logical avenues to explore: (1) a direct comparison to the abundance trends of the analogous carbon and nitrogen polyyne species in this source (HC_nN and C_nH) to explore if the formation and destruction pathways are perhaps similar and (2) state-of-the-art gas-grain chemical models and reaction networks. We explore each of these below, and conclude by discussing the feasibility of future detections of other HC_nO radicals.

4.5.1 Comparison to HC_nN

If we assume that the abundance log-linear decrease in HC_nO family members follows that of the HC_nN family reported in Loomis et al. (140), we can predict the abundances of other HC_nO species. Table 4.2 shows the trend in column density of HC_nN mapped onto that for HC_5O and predicted for HC_3O and HC_7O. Both of these values are larger than our established upper limits, particularly for HC_3O, where the predicted value is nearly two orders of magnitude larger. We therefore conclude that the formation mechanisms that are responsible for HC_nO species are significantly different than those which govern the formation of the HC_nN family.

4.5.2 Comparison to C_nH

The presence of HC_5O in TMC-1 was previously predicted by Adams et al. (2). They propose that the dominant formation pathway for C_nO, HC_nO, and H_mC_nO molecules is through the reaction of $C_nH_m^+$ precursors with CO, followed by dissociative recombination. It could therefore also be argued that the abundances may more closely follow the $C_{n-1}H$ precursors. There are, however, practical difficulties in making such a quantitative com-

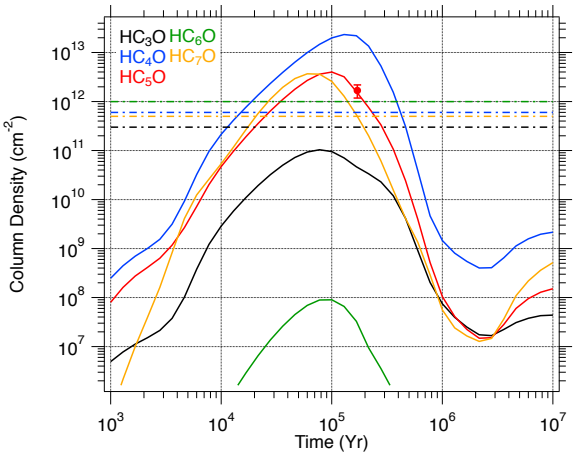

Figure 4.3: Results of the model of the HC_nO radicals discussed in §4.5.3. Gas-phase column densities predicted by the model as a function of time are shown as solid lines. Upper limits established by observation are shown as dashed lines. The observed column density of HC_5O at the best-fit cloud age ($\sim$2 $\times 10^5$ yr) is indicated with a red dot. An estimated error of 30% is shown based on assumed flux calibration accuracy.

parison, especially with respect to C_4H which would be the direct progenitor to HC_5O. As indicated in Eq. 4.1, the calculated column density is inversely proportional to μ^2. There is, however, significant uncertainty in the literature concerning the dipole moment of C_4H, as the ground state of the molecule involves a mixture of two, nearly degenerate electronic states, $^2\Sigma^+$ and $^2\Pi$, with vastly different dipole moments (0.87 – 4.3 Debye) (83). As such, the derived abundance of C_4H in TMC-1 is poorly constrained, making a rigorous, quantitative analysis of this type difficult.

4.5.3 Gas-Grain Chemical Model

Instead, as an initial attempt to model the chemistry of the HC_nO series with $n = 3 - 7$, we have used the NAUTILUS 3-phase astrochemical model developed in Bordeaux (199) with the KIDA 2014 network (231), which we have updated to include reactions related to these species. In a previous study, Adams et al. (2) predicted observable abundances of the $4 \leq n \leq 6$ HC_nO radicals, assuming formation via the dissociative recombination reactions

$$H_2C_nO^+ + e^- \rightarrow HC_nO + H \tag{4.2}$$

$$H_3C_nO^+ + e^- \rightarrow HC_nO + H_2. \tag{4.3}$$

Since only $H_2C_3O^+$ and $H_3C_3O^+$ were included in the KIDA 2014 network, following Adams et al. (2), we have added radiative association reactions (4.4) and (4.5) as formation pathways using the rate coefficients tabulated in Adams et al. (2) for the $4 \leq n \leq 6$ HC_nO series and a calculated Langevin rate coefficient for reaction (4.4) leading to the HC_7O radical. We further updated our chemical network to include destruction of the HC_nO

radicals by photons and ions, with the ion-polar rate coefficients calculated using the Su-Chesnavich capture approach (240).

$$C_{n-1}H_2^+ + CO \rightarrow H_2C_nO^+ + h\nu \tag{4.4}$$

$$C_{n-1}H_3^+ + CO \rightarrow H_3C_nO^+ + h\nu \tag{4.5}$$

With the updated network, simulations were run using standard TMC-1 conditions (106), the results of which are shown in Fig. 4.3. We find the best agreement with the observational results at a time of $\sim$2 $\times 10^5$ yr, and previous studies have noted that TMC-1 models are in good agreement with observations at around this time (106; 146). We note that at this cloud age, there is excellent agreement between the observed and theoretical column densities for HC_5O, and values for HC_3O, HC_6O, and HC_7O are also below the upper limits derived in this work. At $\sim$2 $\times 10^5$ yr, however, we find that HC_4O is overproduced by a factor of about a few compared to our present upper limit. These preliminary results suggest that the ion-neutral reactions noted in Adams et al. (2) can lead to significant abundances of HC_nO radicals that are in good agreement with observation at reasonable timescales. The overproduction of HC_4O in our preliminary models illustrates the need to further explore the chemistry of these radicals, particularly the possible importance of radical-radical reactions and of destruction pathways, which we do not consider in this work due to the current lack of theoretical studies for those pathways.

4.5.4 Future Directions

Our preliminary model well reproduces the observed column density of HC_5O and is in excellent agreement with the upper limits for HC_3O and HC_7O, which may indicate that the chemistry of the n odd HC_nO radicals is rather well-constrained. If so, this would be in agreement with the composite average evidence for a population of HC_7O just below our detection limit (see Fig. 4.2b). Given the already long integration times, and the fact that at these excitation temperatures there are no appreciably stronger transitions, however, either a significantly greater investment of observing hours or a composite average of several additional transitions would be needed to establish a firm detection. Unless the column density for HC_3O is much higher than predicted by the model, it is unlikely a detection will be possible in any practical integration time. Because our current model is unable to reproduce the observed upper limit to HC_4O, we reserve comment on its detectability at this juncture.

4.6 Conclusions

We have presented the discovery of the HC_5O radical through observation of four well-resolved hyperfine components in high-sensitivity observations of TMC-1 with the Green Bank Telescope. A search for other HC_nO radicals ($n = 3 - 7$) resulted in non-detections. A first-look chemical model well-reproduces the observed column density of HC_5O and

agrees with the upper limits inferred for HC_3O, HC_6O, and HC_7O. HC_4O, however, is over-produced in the model, likely indicating that additional reaction pathways not considered here contribute significantly to that chemistry. A detailed modeling study is now underway to more thoroughly examine these possibilities.

4.7 Acknowledgments

The National Radio Astronomy Observatory is a facility of the National Science Foundation operated under cooperative agreement by Associated Universities, Inc. The Green Bank Observatory is a facility of the National Science Foundation operated under cooperative agreement by Associated Universities, Inc. S.V.K. acknowledges support from Basic Research Program P-7 of the Presidium of the Russian Academy of Sciences. E. H. thanks the National Science Foundation for support of his astrochemistry program. A.M.B. is a Grote Reber Fellow, and support for this work was provided by the NSF through the Grote Reber Fellowship Program administered by Associated Universities, Inc./National Radio Astronomy Observatory. The authors thank the anonymous referee for comments which improved the quality of this manuscript.

Part III

Constraining Effects of Shock Chemistry: Observations and Modeling of Isolated Molecular Outflows

Preface and Future Directions

Astrophysical shocks are seen to occur over a wide variety of sources, scales, and speeds, from active galactic nuclei jets to galaxy-wide shocks inducing large-scale star formation to protostellar sources ejecting accreting material out as jets to supernovae exploding out into surrounding circumstellar media. These transient phenomena can have dramatic, and sometimes permanent, effects on the material it interacts. Because the observations of molecules can act as useful probes and tracers of various physical processes and properties, it is important to understand how shocks impact the chemistry of a given source.

Formally, a shock is a process in fluid dynamics where a fluid is traveling faster than the sound speed of the material it is going through. As a result, as the fluid propagates through the material, it entrains additional matter, inducing a irreversible, pressure-driven compression and temporary spikes in temperature(63). Much of the discussion that follows is discussed in detail in Draine and McKee (63) and Draine (61). As the material is slowed, the kinetic energy is converted into thermal energy, which subsequently heats the surrounding gas or is radiated away. Unlike collisionally-mediated shocks that typically occur on Earth, astrophysical shocks have mean free paths commonly larger than the source itself, and thus are instead mediated by interaction with the bulk electromagnetic fields in the source (63).

As the fluid motion is governed by the conservation of energy, mass, and momentum (134), along with Maxwell's equations for electromagnetism, there exist standard conditions that must be maintained throughout the sharp changes in density, velocity, and pressure across the shock event. These jump conditions are referred to as the Rankine-Hugonist conditions. Adopting the frame of reference of moving with the shock front, the shock appears to be stationary. Therefore, variables and physical conditions with a steady shock will be independent of the time. Approximating the shock front as plane-parallel, we can also assume that the changes in the fluids will only occur in one physical direction, or that no perpendicular evolution exists. Through these assumptions of conservation of mass, momentum, energy, and magnetic flux, we arrive at the jump conditions that must be maintained between any two points across the shock (assuming a single fluid):

$$\rho_1 v_1 = \rho_2 v_2$$

$$\rho_1 v_1^2 + p_1 + \frac{B_1^2}{8\pi} = \rho_2 v_2^2 + p_2 + \frac{B_2^2}{8\pi}$$

$$\frac{\rho_1 v_1^3}{2} + \frac{\gamma}{\gamma - 1} v_1 p_1 + \frac{v_1 B_1}{4\pi} = \frac{\rho_2 v_2^3}{2} + \frac{\gamma}{\gamma - 1} v_2 p_2 + \frac{v_2 B_2}{4\pi}$$

$$v_1 B_1 = v_2 B_2$$

where ρ is the mass density, v is the velocity, p is the momentum, B is the magnetic field strength, and γ is the specific heat ratio.

These conditions are formally used to describe a shock wave that can be characterized by a single fluid, which is valid for a completely ionized gas. However, in regions of interest to astrochemistry, the material must instead be treated as having both a neutral fluid of gas particles and a plasma of ions and electrons. Because magnetic fields in the shock can accelerate charged particles in the plasma, such as dust grains, much more efficiently than the neutral gas, the two fluids will decouple and induce a two-fluid magnetohydrodynamic (MHD) shock. Depending on the strength of the magnetic field, and in turn the significance of ion-neutral collisions, these shocks can be classified as either C-shocks or J-shocks. When the magnetic field is weak or the velocity of the shock is large ($>$40 km s^{-1} for standard interstellar conditions), the ion-neutral collisions can become highly efficient which, in turn, heats the neutral fluid enough to deaccelerate it to subsonic values. At this point, there is a near-instantaneous "jump" in the shock structure and is referred to as a J-shock. On the other hand, if the magnetic field is sufficiently strong or the shock velocity is reasonably slow (10-40 km^{-1} for standard interstellar conditions), then the neutral fluid will remain cold and is able to maintain a supersonic velocity. This results in the physical conditions within the shock to remain "continuous," and is referred to as a C-shock (60). In actuality, in many MHD shocks, both C-shocks and J-shocks can exist in the same region due to the gradients in physical conditions. However, one shock tends to dominate, depending on the observational signature of choice.

One major physical process that results from these shocks is sputtering, or the non-thermal desorption of species from the surface into the gas phase due to collisions between accelerated particles and the icy grains (64). This process is especially important in the study of astrochemistry, as molecules that are typically frozen onto ice in cold interstellar environments can be efficiently brought into the gas phase through this method. To produce the complex organic molecules (COMs) observed in the interstellar medium (ISM), there are two major regimes of interstellar chemistry: reactions that occur in the gas-phase and reactions that occur in the ice mantles of dust grains. It is believed that many complex organic molecules (COMs) have efficient ice-chemistry formation routes (77; 104). However, our knowledge of interstellar ice-chemistry still remains highly unconstrained due to a much less robust molecular inventory. This uncertainty arises from the fact that, unlike gas-phase molecules, solid-phase molecules can only be observed through infrared ice absorption observations, which requires the fortuitous alignment of a strong infrared background source, a colder ice-rich source in the foreground, and a telescope capable of observing the proper transitions. Observations of these vibrational transitions are further complicated because the transitions can be highly degenerate between similar species (making individual identification difficult). Furthermore, many of the transitions of interest reside at wavelengths commonly blocked or attenuated by the Earth's atmosphere (requiring space-based observatories). As such, less than 20 individual species have been successfully identified in interstellar ices (27), compared to the $\sim$200 detected gas-phase species. Because of the challenges in direct observations of ice-chemistry, an alternative ways to constrain this molecular reservoir have been proposed, including gas-phase ob-

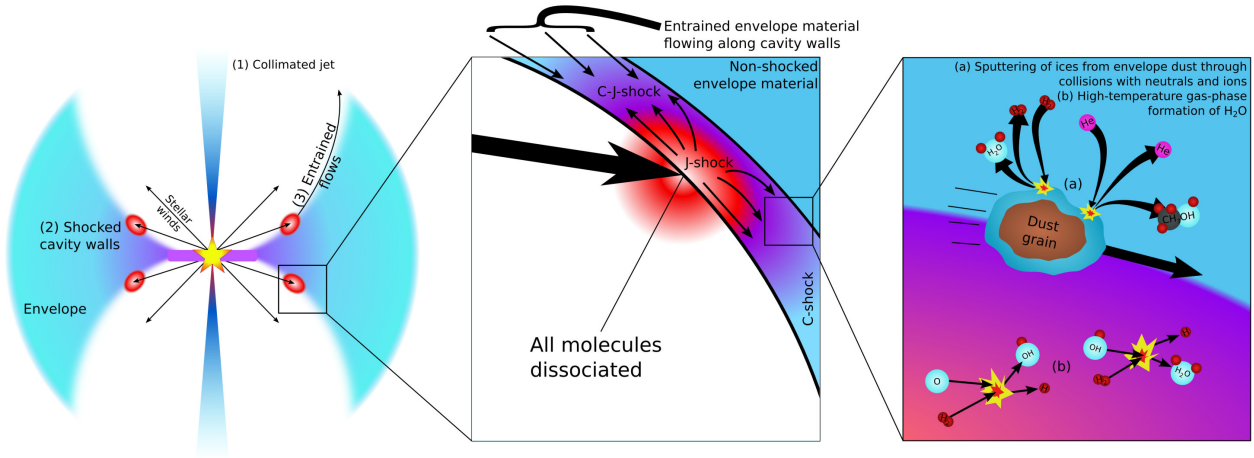

Figure 4.4: A series of diagrams (not to scale) illustrating the shock chemistry within a molecular outflow originating from a young stellar object. *Left* The general shape of the disk and outflow surrounding a young protostar and where astrophysical shocks occur. *Center* A zoom-in on the structure of one shock event. *Right* Sputtering and post-shock gas-phase chemistry is displayed as the gas and dust interact within a shock. Figure originally from Suutarinen et al. (209).

servations of these molecules immediately after they desorb off the surface. Thermal desorption, which can be efficient within hot cores, can effectively liberate the ice-mantle into the gas, but can induce additional chemistry in the process. And so, we require additional ways to desorb the chemical-rich ices into the gas phase as a way to probe this mostly-unconstrained chemical reservoir. The sputtering in astrophysical shocks, which liberate molecules off from the ice into the gas phase without additional thermal processing, provide this indirect probe (see Fig. 4.4 *Right*).

The efficiency of sputtering varies when comparing C-shock and J-shocks in astrophysical sources, resulting in different observational signatures (see Fig. 4.4 *Center*). The lower velocity C-shocks tend to liberate the molecules that make up the ice covering the interstellar dust grains without destroying most molecular bonds (192). As a result, species that are efficiently formed on the ice, such as CH_3OH and HNCO are seen to be strongly enhanced in C-shocks (14; 165). Conversely, J-shocks are energetic enough that many of these molecules are dissociated during the process and to even start sputtering off species from the refractory grain core. As a result, high velocity shocks can often be traced by species containing Si, which is commonly locked up in dust grains, with enhancements in particular being prominent SiO (90; 91). Because we wish to utilize shocks to probe the chemical complexity within the ice, we will therefore focus on C-shocks in this work.

In addition to the gas-phase abundance enhancements brought on by sputtering, the temporary high temperature and density conditions within the shocks can also induce post-shock gas-phase chemistry (34; 209). Therefore, in order to determine what the un-

derlying pre-shock ice chemistry was, it is necessary to determine which observational gas-phase enhancements are due to sputtering and which are due to post-shock chemistry within astrophysical sources. This has been studied both by comparing the locations of peak abundances of different molecules throughout a bow shock front (46; 209).

In particular, one of the most commonly studied types of sources to study shock chemistry is in the molecular outflows propagating out from low-mass protostars (see Figure 4.4 *Left*). As low-mass star formation tends to occur in relative isolation compared to high-mass counterparts (162), their bipolar outflows are able to launch ejected material into the pristine, chemically-rich ice in the surrounding dark cloud, where it can be subsequently shocked without any other significant competing physical processes. One source in particular that has received significant study is the prototypically chemically-active shocked outflow, L1157, which has been shown to display a high degree of molecular complexity (7; 33; 46; 137; 158; 165).

And so, in order to study ice-chemistry reservoirs in protostellar environments and understand the impacts of shocks on the chemistry in a region, we performed observations of several shock-tracing molecules toward L1157 with the Combined Array for Research in Millimeter-wave Astronomy (CARMA), as described in Chapter 5. From these observations, we made several predictions regarding shock-chemistry in isolated molecular outflows. In order to test these predictions, Chapter 6 discusses our efforts to reproduce these effects through the synthesis of astrochemical models and the physical conditions and processes associated with shocks.

Moving forward from this work, in order to fully test the results of the astrochemical model, it is necessary to have observational constraints on the various parameters the model uses. Because the model considers far more molecules than have been observationally detected, the creation of a chemical inventory of as many molecules as possible and how they temporally evolve would allow us to better understand how the post-shock gas-phase chemistry proceeds. To do this, in the coming years, we will perform the first broadband interferometric survey of L1157 using the Submillimeter Array (SMA), taking advantage of the SMA Wideband Astronomical ROACH2 Machine (SWARM) correlator's 32 GHz of continuous bandwidth to efficiently probe a large range of molecular transitions simultaneously (245). This survey will allow us to produce radial (and thus time-dependent) profiles for a large number of molecules of varying complexity across the blue shifted lobe of L1157, which would provide crucial constraints to the astrochemical model. In addition, these observations will also allow us to study the dynamics of the outflow itself, potentially answering the questions of whether previously unmapped molecules support the two precessing jet model in this source and whether it is possible to resolve chemical transitions in the envelope surrounding the central protostar.

In addition to constraining the evolution of molecular complexity in this one source, it is vital that the predictions of shock-chemistry here are also valid in other sources with a wide range of shock velocities, shock ages, densities, and stages of protostellar evolution. As such, a broad, unbiased Band 7 spectral line survey is currently being observed with the Atacama Compact Array (ACA) of seven southern outflows of widely-varying ages, velocities, and chemical conditions to elucidate the underlying links between phys-

ical conditions, outflow properties, and chemical evolution in these important pre-stellar environment through the Shocked Molecular Outflows across a Range of Environments Survey (SMORES). Through this survey, we will be able to create complex molecular inventories, probe the spatio-temporal chemical evolution, and constrain our astrochemical shock models for these seven sources. Moving on beyond this, additional spectral surveys can also be performed with SMA to probe northern molecular outflows.

In terms of improvements to the astrochemical model, we intend to continually develop and enhance the capabilities through the refinement of current processes and the inclusion of new ones. First and foremost, recent work by Shingledecker et al. (204) showed that the inclusion of cosmic ray-induced chemistry can significantly enhance the ice and gas-phase abundances in dark cloud conditions. Since cosmic rays are thought to be common in astrophysical shocks (70), the inclusion of these processes could be highly effective at overcoming the current underproduction of certain observationally ice-abundant species. These reactions types are in the current version of NAUTILUS (199) used for the shock model, but are not activated in the model. In addition to ice-species enhancements, cosmic rays can also induce additional sputtering and gas phase processes. As such, future work to study the effect of cosmic rays on shock chemistry could be highly fortuitous.

In order to treat the most common shock tracer for astronomers, SiO, it would be necessary to consider how the grain itself is impacted by the shock. To physically produce the SiO, one would need to include some form of core-sputtering, which would require the inclusion of solid-phase abundances of both carbonaceous and silicate dust grains as a fourth phase of chemistry in the model. The inclusion of this additional phase could also facilitate the simultaneous modeling of C-shock tracers, such as HNCO, and J-shock tracers, such as SiO. Grain erosion or shattering could also be considered, which would dynamically impact the average dust grain size, and subsequently alter the total surface area for ice-surface reaction to occur and the collisional cross section of the grains.

As well, many of the reactions discussed here in the post-shock chemistry were gas-phase reactions whose temperature dependence was more effectively calculated and measured at high temperature ranges (95). It is possible that in the hot-gas regime of the model, reactions with significant barriers, but are strongly correlated with the gas temperatures, may become important. While these reactions' barriers make them uncommon for typical studies in astrochemical models, initial estimations and the few that were added suggest that some number of them could be highly efficient in post-shock gas. As such, a more robust treatment of these types of reactions may prove to induce additional post-shock gas-phase chemistry.

CHAPTER 5

CSO AND CARMA OBSERVATIONS OF L1157: CHEMICAL COMPLEXITY IN THE SHOCKED OUTFLOW

The following chapter is primarily reproduced from Burkhardt, A. M.; Dollhopf, N. M.; Corby, J. F.; Carroll, P. B.; Shingledecker, C. N.; Loomis, R. A.; Booth, S. T.; Blake, G. A.; Herbst, E.; Remijan, A. J.; McGuire, B. A. The Astrophysical Journal ***2016****, 827, 1-17.*

L1157, a molecular dark cloud with an embedded Class 0 protostar possessing a bipolar outflow, is an excellent source for studying shock chemistry, including grain-surface chemistry prior to shocks, and post-shock, gas-phase processing. The L1157-B1 and B2 positions experienced shocks at ∼2000 and 4000 years ago, respectively. Prior to these shock events, temperatures were too low for most complex organic molecules to undergo thermal desorption. Thus, the shocks should have liberated these molecules from the ice grain-surfaces *en masse*, evidenced by prior observations of SiO and multiple grain mantle species commonly associated with shocks. Grain species, such as OCS, CH_3OH, and HNCO, all peak at different positions relative to species that are preferably formed in higher velocity shocks or repeatedly-shocked material, such as SiO and HCN. Here, we present high spatial resolution (∼3″) maps of CH_3OH, HNCO, HCN, and HCO^+ in the southern portion of the outflow containing B1 and B2, as observed with CARMA. The HNCO maps are the first interferometric observations of this species in L1157. The maps show distinct differences in the chemistry within the various shocked regions in L1157B. This is further supported through constraints of the molecular abundances using the non-LTE code RADEX (244). We find the east/west chemical differentiation in C2 may be explained by the contrast of the shock's interaction with either cold, pristine material or warm, previously-shocked gas, as seen in enhanced HCN abundances. In addition, the enhancement of the HNCO abundance toward the the older shock, B2, suggests the importance of high-temperature O-chemistry in shocked regions.

5.1 Introduction

Shocks and turbulence are prevalent in molecular gas, from dense gas undergoing star formation to diffuse material filling the thin disk of the Galaxy. Thus, it is crucial to un-

derstand the underlying chemistry within shocked regions. For many complex molecules, gas-phase formation routes are inefficient under interstellar conditions, and are unable to reproduce observed abundances. Theoretical work instead predicts efficient chemical reactions on the ice mantles of dust grains (30; 99), and laboratory work confirms that grain-surface chemistry efficiently produces diverse molecular species (74; 176). Low-velocity C-shocks, common in dense molecular clouds, sublimate the ice from the surfaces of grains without destroying most molecular bonds (192). As a result, gas-phase observations of recently-shocked clouds can provide substantial information on the condensed-phase chemistry that occurred prior to the passage of the shock. Reactions on the surface of grains are now believed to be responsible for the formation of most complex organic species (77), and studies of shocked molecular clouds are essential for understanding the processing of molecular material and the formation of biologically-relevant molecules. Given the difficulties of unambiguously identifying molecules trapped in ice grains, shock-chemistry studies are among the most promising cases for understanding ice grain chemistry.

The nearby ($\sim$250 pc) dark cloud, L1157, provides an excellent opportunity to study shock chemistry. L1157 contains a Class 0 protostar, L1157-mm, with a bipolar outflow that extends $\sim$2′, or 3×10^4 AU, from the central infrared source (142). The blueshifted and redshifted outflows are referred to as L1157B and L1157R, respectively. As the jet precesses, the periodic ejection events produce bow shocks at multiple positions in the outflow (86). The bow shocks, in turn, produce regions of minimal protostellar heating of the dust, and significant shock-induced non-thermal desorption of grain mantles (71).

L1157-B1 and B2 are prominent, recently-shocked regions in the southern, blue-shifted lobe of the outflow. B1 is warmer and more recently shocked ($T_{\rm kin} \sim$ 80-100 K, t $\sim$ 2000 yr) than B2 ($T_{\rm kin} \sim$ 20-60 K, t $\sim$ 4000 yr) (86; 136; 212). The progenitor gas for B1 and B2 should have had a cold history within the dark cloud (at T < 20 K for $\sim$1 Myr). The unshocked portions of the outflow are also cool (at $T_{\rm kin}$ $\sim$15 - 30 K) (9). As a result, observations of B1 and B2 primarily probe the chemistry of cold ($\lesssim$20 K) ice-grain mantles, and subsequent evolution in the warmer gas-phase.

B1 and B2 are considered chemically-active outflows (9), with the detection of numerous complex species including $HCOOCH_3$, HCOOH, CH_3CHO, NH_2CHO, C_2H_5OH, and CH_3CN (7; 242, and refs. therein). Abundances of shock tracers including SiO, CH_3OH, and HNCO are particularly enhanced in B1 and B2 as compared to unshocked regions of the outflow. This includes an SiO abundance enhancement of 10^4 compared to unshocked material in the region, which high spatial resolution ($\sim$2.5″) images indicate that the distribution of SiO closely traces the positions of B1 and B2 (87). Furthermore, L1157-B2 has been found to contain the highest abundance of HNCO yet observed in any source in the Galaxy, including an enhanced abundance of 4-11 times compared to hot cores and dense cores in the Galactic Center (165; 196).

Interferometric images of multiple molecules have demonstrated the clumpy structure of the southern outflow. Previous work by Benedettini et al. (15) at λ=3 mm mapped transitions of CS, CH_3OH, HCN, OCS, and ^{34}SO at $\theta \sim$ 3-6″ spatial resolution with the Plateau deBure Interferometer (PdBI). In this work, we present images of 3 mm transitions

of HCO^+, HCN, CH_3OH, and HNCO observed by the Combined Array for Research in Millimeter-Wave Astronomy (CARMA). While two of the species have been imaged with comparable resolution, this work produces a higher spatial resolution map of HCO^+ and the first interferometric map of HNCO in L1157.

Furthermore, we build upon the work of McGuire et al. (159, hereafter Paper I) to estimate column densities and abundances of three of the species (CH_3OH, HCN, and HNCO) in the B1 and B2 clumps.

5.2 Observations

We observed the southern outflow with the CARMA 15-element array at λ = 3 mm, targeting the $J = 1 - 0$ transitions of HCN and HCO^+, four $J = 2_K - 1_K$ transitions of CH_3OH, and the $J = 4 - 3$ transition of HNCO, as described in Table 5.1. A total of 89.3 hours of observations were conducted: 46.7 hours in C-configuration during August 2012, 23.3 hours in D configuration between October and November 2012, and 19.3 hours in E-configuration during May 2013. All observations were toward a single pointing position at α(J2000) = $20^h39^m07^s.7$, δ(J2000) = 68°01′11″.5. The 62 MHz bandwidth, 3-bit mode of the CARMA correlator was used, providing fourteen non-contiguous windows with 255 channels each, and resulting in 243 kHz ($\sim$0.7 km s^{-1}) channel resolution.

The data were reduced using the MIRIAD package (201) using standard techniques of bandpass, absolute flux, and complex gain calibration. MWC349 and Neptune were used as primary flux calibrators; the bandpass calibrators were 1635+381, 2232+117, 0102+584, 1743-038, 2015+372, and 3C84; and the gain calibrator was 1927+739. Images were generated using the CLEAN algorithm in the MIRIAD package with a Briggs weighting scheme that tended toward natural weighting, resulting in a synthesized beam of 3.″4 × 3.″2 at the center frequency for the majority of the observed transitions. Image analysis was performed in CASA. The targeted transitions and synthesized beam values are shown in Table 5.1. The synthesized beam of the CH_3OH maps are about a factor of two larger than the other observed transitions because the CH_3OH lines were not observed in the most extended configuration used (C-array). While primary beam corrections were not applied, preliminary analysis implied that the ultimate impact of this correction would be minimal, especially for the regions where we perform more in-depth analysis. It should be noted that the sensitivity of the 10-m antennae will be more significantly reduced at the edges of the primary beam in this single pointing.

5.3 Results

5.3.1 Structure

Table 5.1: The resolved quantum numbers and frequencies of each transition are listed. Also included are the synthesized beam sizes and approximate rms levels for each window, where no spectral binning was performed. Transitions and parameters accessible at `www.splatalogue.net` (188). Catalogued at CDMS (172). and JPL (178)

Molecule	Transition	ν (GHz)	E_u (K)	Beam (arcsec^2)	RMS (σ) (mJy beam^{-1})
CH_3OH	$2_{-1,2} - 1_{-1,1}$	96.73936(5)	12.9	$6\farcs03 \times 5\farcs53$	8.5
	$2_{0,2} - 1_{0,1}++$	96.74138(5)	6.9		
	$2_{0,2} - 1_{0,1}$	96.74455(5)	20.1		
	$2_{1,1} - 1_{1,0}$	96.75551(5)	28.0		
HCN	$J = 1 - 0, F = 1 - 1$	88.63042(2)	4.25	$3\farcs45 \times 3\farcs27$	4.8
	$J = 1 - 0, F = 2 - 1$	88.63185(3)	4.25		
	$J = 1 - 0, F = 0 - 1$	88.63394(3)	4.25		
HCO^+	$J = 1 - 0$	89.18853(4)	4.28	$3\farcs39 \times 3\farcs23$	5.1
HNCO	$J = 4_{0,4} - 3_{0,3}$	87.92524(8)	10.6	$3\farcs50 \times 3\farcs28$	7.0

Summary of L1157B Structure

To orient the reader to the structure of the southern, blueshifted outflow, L1157B, we highlight the positions of the shocked clumps with respect to the two cavities, C1 and C2, originally observed in CO (88). Observations of SiO, a prominent shock tracer, reveal large abundances along the structures of the cavities. Figure 5.1 shows line emission by CH_3OH and HCO^+ observed by CARMA with the position of the cavities highlighted. The southern-most cavity, C1, holds the shocked B2 region, while the B1 region is observed at the apex of the C2 (northern) cavity. The bowshock nature of the outflow is apparent from the U-shaped structure of C2 observed with CH_3OH, other shock tracers, and mid-IR emission (213)

The B0 region follows the shape of the C1 cavity north of B1 into the L1157-mm source; however, B0 is not correlated with a shock front, and much of it remains cool ($T_{\rm kin}$ $\sim$15-30 K; 9). The aforementioned U-shaped structure along the C2 walls delineates B0 from the ambient gas. The eastern B0 wall shows higher abundances of SiO and HCN than the western wall (94), perhaps suggesting a pseudo-shock event in the region. There is also a ridge of emission connecting the east and west walls of B0, showing similar abundances to the western wall.

High spatial resolution, interferometric observations of the outflow reveal a clumpy structure within L1157 (15). Within all three regions, molecules are seen to peak in clumps $\sim$10-15$''$ in diameter. In B1 and B2, these clumps lie within the shocked regions. In B0, these clumps are well correlated with the eastern wall, western wall, and the emission ridge.

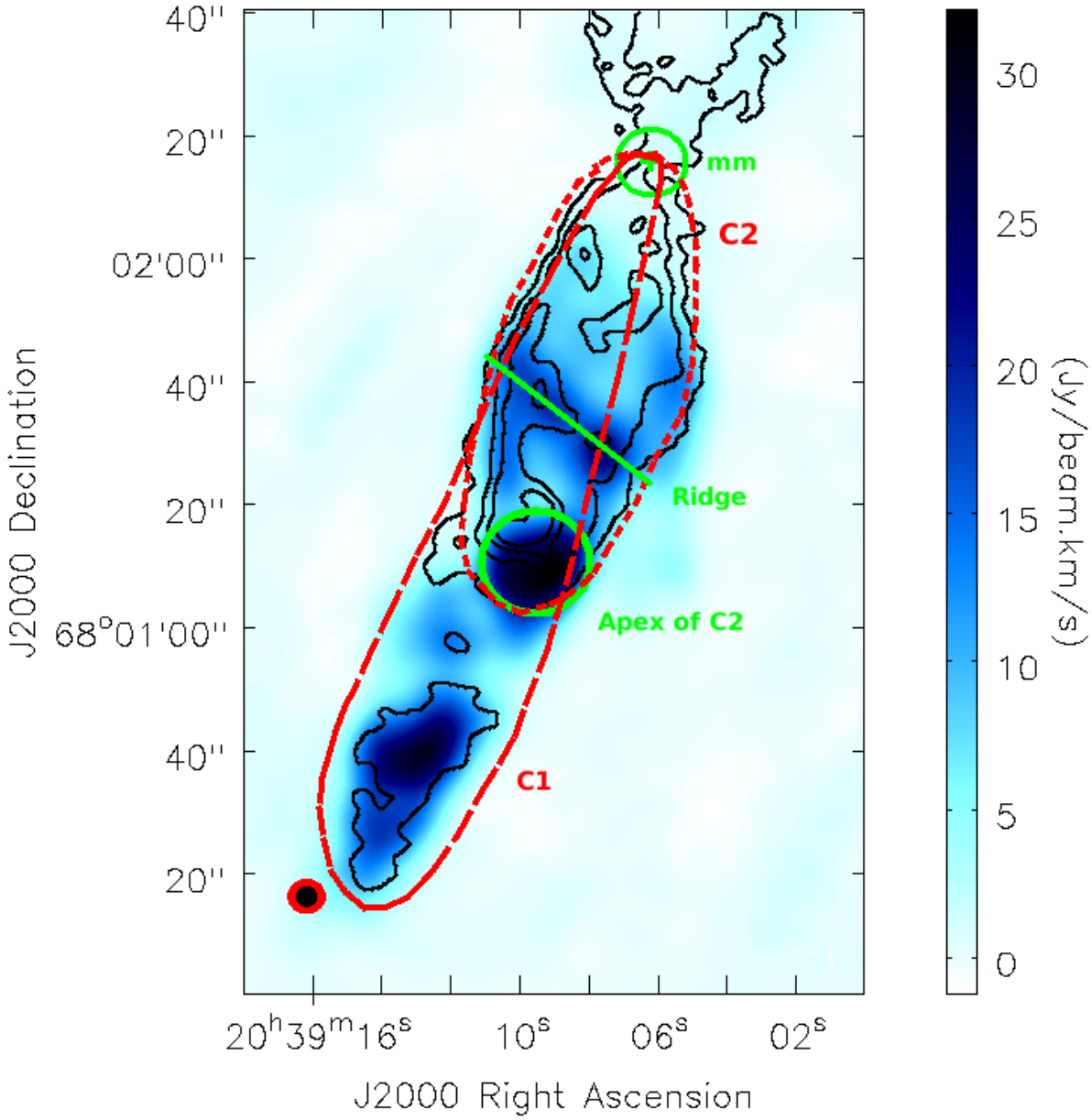

Figure 5.1: Integrated CH_3OH ($2_K - 1_K$) emission raster, -17.8 to +14.0 km s^{-1}, with integrated emission of HCO^+ (1-0) contours, -20.1 to +11.9 km s^{-1}, overlayed in black, both observed with CARMA. The contour levels for HCO^+ are 0.44, 0.88, 1.32, 1.76, 2.2 Jy $beam^{-1}$ km s^{-1}. The synthesized beam sizes for CH_3OH and HCO^+ are shown in red and black, respectively, in the lower left. The two cavities in L1157B are shown and labeled in red, with the ridge and apex of C2 shown and labeled in green.

Table 5.2: Region Positions and Sizes. Regions based off of Benedettini et al. (15) and Rodríguez-Fernández et al. (196), with several new clumps assigned (B0k, B0ℓ, and B2d). For non-circular regions, the semi-minor axis, semi-major axis, and position angle of the semi-major axis from straight north are given in that order. L1157-mm source size is likely much smaller, but the region size and shape were chosen for comparison to clumps in outflow.

	Ellipse Center		Ellipse Parameters		
Region	RA (J2000) (^{h} ^{m} ^{s})	Dec. (J2000) ($^\circ$ $'$ $''$)	RA ($''$)	Dec. ($''$)	PA ($^\circ$)
B0a	20 39 10.4	68 01 38.0	11	11	-
B0b	20 39 05.7	68 01 42.0	14	14	-
B0c	20 39 09.0	68 01 36.0	11	11	-
B0d	20 39 07.7	68 01 28.0	12	12	-
B0e	20 39 10.3	68 01 24.0	12	12	-
B0k	20 39 08.1	68 02 00.4	11	11	-
B0ℓ	20 39 06.4	68 01 54.3	11	11	-
B1a	20 39 10.2	68 01 12.0	11	11	-
B1b	20 39 08.8	68 01 10.0	11	11	-
B2a	20 39 12.6	68 00 40.7	7.5	15.5	50
B2b	20 39 13.8	68 00 26.8	7.5	15.5	50
B2c	20 39 11.8	68 00 58.0	13	13	-
B2d	20 39 14.1	68 00 37.7	5	12	0
mm	20 39 06.2	68 02 15.9	11	11	-

Structure Revealed by CARMA Maps

The HCN and CH_3OH transitions presented here were previously imaged by Benedettini et al. (15) with similar resolutions. Indeed, the structure observed by CARMA agrees with the PdBI images previously published. While discussing the structure in this work, we therefore adopt the naming convention of Benedettini et al. (15) and further added to by Codella et al. (48) and Gómez-Ruiz et al. (94). They defined 10 clumps in B0 (B0a-B0j), 8 clumps in B1 (B1a-B1h), and 3 clumps in B2 (B2a-B2c), based primarily on emission from CH_3OH, HCN, CH_3CN, SiO, and H_2CO. To maintain consistency with previous work, we specify elliptical regions corresponding to the clump positions reported in these papers. While the regions were described as ellipses $\sim$10-15$''$ in size (15), we specify the dimensions of the ellipses with major and minor axis lengths determined based on the distributions observed in our images. We also define three new clumps: B0k and B0ℓ using the HCO^+ emission, and B2d using the HNCO emission. The coordinates and dimensions of the regions used are defined in Table 5.2. Also in Table 5.2, we list the region used to extract the spectra toward the gas surrounding L1157-mm, whose position was determined by Gueth et al. (88). While the source size is likely much smaller than the region used, the size and shape were chosen for comparison to clumps in outflow. Figure 5.2 shows the integrated line emission of CH_3OH 2_k-1_k, HCN (1-0), HCO^+ (1-0), and HNCO ($4_{0,4} - 3_{0,3}$), with the elliptical regions overlaid.

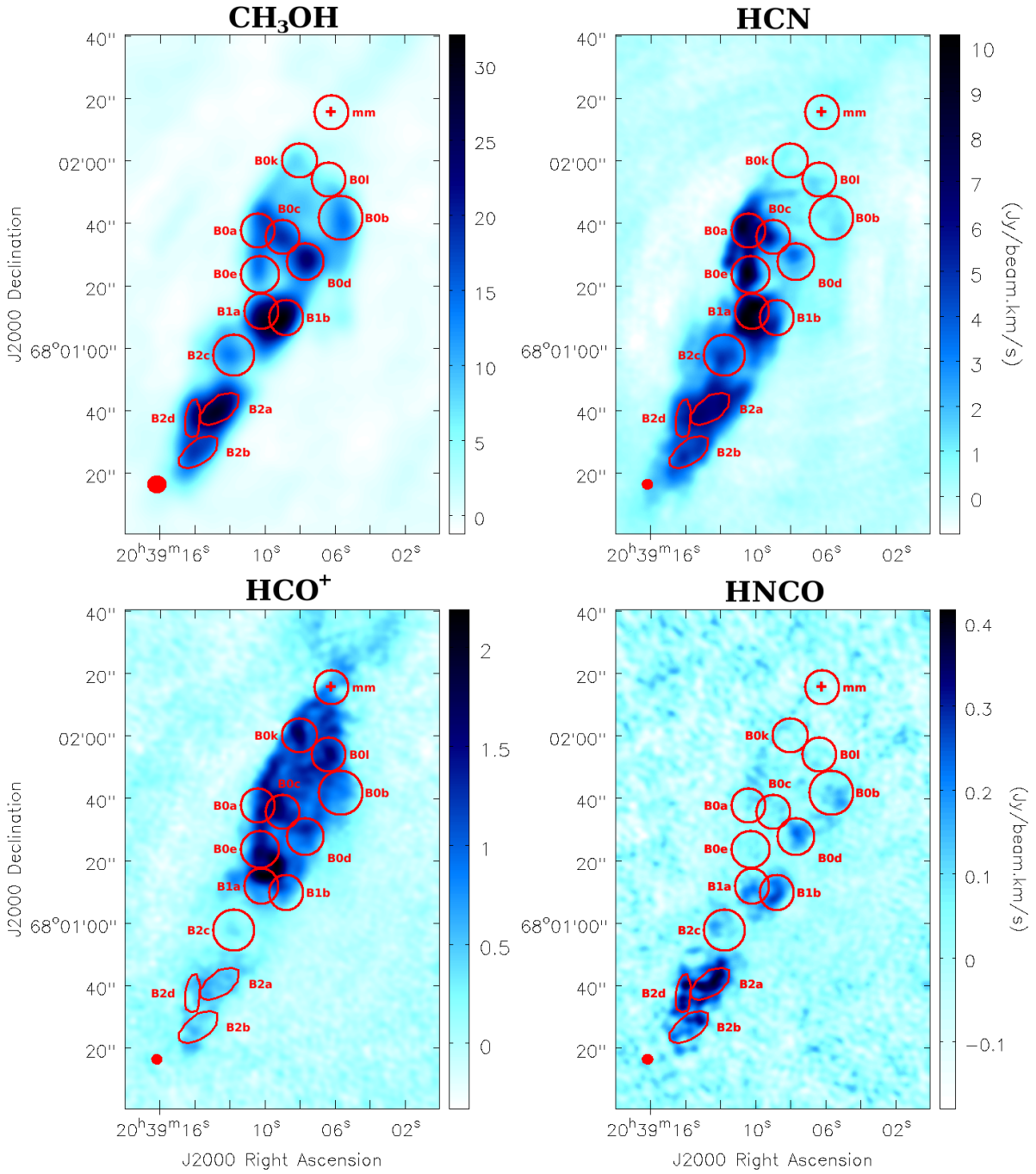

Figure 5.2: Integrated emission maps of CH_3OH ($2_k - 1_k$), HCN (1-0), HCO^+ (1-0), and HNCO ($4_{0,4} - 3_{0,3}$) with the clump regions and stellar source shown in red. The velocity ranges of integration were (-17.8 to +14.0 km s^{-1}), (-22.1 to +15.0 km s^{-1}), (-20.1 to +11.9 km s^{-1}), and (-6.45 to +6.9 km s^{-1}), respectively. The synthesized beam sizes are displayed as filled red in the lower left.

CH_3OH

CH_3OH 2_k-1_k displays a clumpy structure that is consistent with the previous observations by Benedettini et al. (15). In our newly-assigned clumps of B0k, B0ℓ, and B2a, we detect emission, although the clumps are not as prominent in CH_3OH emission as in HNCO and HCO^+. As has been found in previous observations, CH_3OH emission is generally observed to be brighter on the western side of B1, and has significant emission along the ridge in B0.

HCN

HCN (1-0) shows structure similar to CH_3OH, with significant clumping evident throughout L1157B. However, whereas CH_3OH produces stronger emission on the western wall of the C2 cavity (i.e. in B1b, B0d, B0b), HCN emission is strongest on the eastern wall of C2 (i.e. in B1a, B0e, and B0a). This trend was also reported in Benedettini et al. (15). Significant structure is also seen outside of these clumps that is not seen in other molecules, especially toward the eastern wall of B0, with an arm protruding to the east of B0. This structure has been observed previously in SiO (5-4) as an "arc-like" structure to the east of the U-shape of C2 (94). HCN (1-0) has stronger emission toward the eastern clumps of B1, unlike CH_3OH, which is consistent with the chemical segregation previously observed (15). In B2, we observe significant emission toward B2a, B2b, and B2d.

HCO^+

HCO^+ (1-0) exhibits a more extended distribution, and is detected beyond the combined 10m-6m primary beam ($\sim 2'$) of CARMA along the outflow axis. The HCO^+ emission is observed further into B0, tracing the C2 cavity, than the other molecules observed, and extending past the stellar source. We define two new clumps with HCO^+, B0k and B0ℓ, located in the northern regions near the stellar source, L1157-mm. Strong emission is present in C2, particularly toward the eastern wall and the northern clumps, while much weaker emission is observed toward C1. The distribution is consistent with previous interferometric observations of HCO^+, where the majority of the emission was observed to trace the low-velocity ambient gas in B0 (9; 45).

HNCO

HNCO exhibits a distribution distinct from the other observed species, with significantly-stronger line emission from B2. Weaker line emission is associated with B1 and the western wall of B0, similar to CH_3OH and unlike HCN. Previous single-dish observations have detected strong HNCO line emission toward B1 and B2, which are in agreement with our observations (165; 196).

5.3.2 Spectra and Column Density Determination

We extracted spectra from the regions defined in Table 5.2. Transitions of CH_3OH, HNCO, and HCN, including hyperfine components, were fit with Gaussian profiles, utilizing a modified version of the line fitting code described in Corby et al. (52). Figure 5.3 displays the extracted spectra of the observed molecules at 5 representative regions which probe the emission at a variety of environments across L1157B: B0a, B0d, B1a, B1b, and B2a, with line fits overlaid. Spectra for all of the defined regions in Table 5.2 are included in the Appendix 5.7 and Gaussian fits parameters are in Appendix 5.8.

An inspection of the line fit parameters reveal the kinematic structure of the outflow. For the purposes of studying the systemic velocities, we use the average velocities for the three strongest components of CH_3OH and the $F = 1 - 1$ hyperfine transition of HCN, which will be further discussed in Sections 5.3.2 and 5.3.2, respectively. The gas surrounding the stellar source, L1157-mm, was found to have velocities between $v_{\rm LSR}$ ∼2.3-3.1 km s^{-1}. For reference, the cloud velocity for this region has been found to be $v_{\rm LSR}$ ∼2.6 km s^{-1} (8).

In general, the clumps located in B0 south of the ridge, B1, and B2c are found to be kinematically related, with average systemic velocities around 0 to 1.5 km s^{-1}. Meanwhile, in the northern part of B0, the systemic velocities generally increase for each species: ∼1 km s^{-1} for CH_3OH, ∼1.3 km s^{-1} for HCN, and ∼1.6 km s^{-1} for HNCO. Toward B2, the velocities are found to be consistent and larger than what was found in B1, southern B0, and B2c: ∼2 km s^{-1} for CH_3OH, ∼0.9 km s^{-1} for HCN, and ∼1.8 km s^{-1} for HNCO. While the line widths of CH_3OH consistently remain around 3.4 km s^{-1} throughout L1157B, HCN has smaller line widths in northern B0 (∼2.1 km s^{-1}) than the rest of the L1157B, which displays similar line widths to CH_3OH of ∼3.5 km s^{-1}. Even more dramatically, the line widths of HNCO within these three kinematic regions are found to be distinct: ∼1 km s^{-1} in northern B0, ∼5 km s^{-1} in southern B0 and in B1, and ∼3 km s^{-1} in B2. Curiously, while the HNCO (4-3) line velocity shift in B2c is more related to the apex of C2, the line width is closer to the rest of B2. It is important to note that the current naming scheme for clumps in L1157 does not appear to accurately reflect the regions that are kinematically associated. Based on these findings, HNCO may prove to be a useful probe for disentangling kinematic structure in these sorts of regions, perhaps due to its unique formation pathway, as discussed in Section 5.4.3.

To compute the column densities of CH_3OH, HCN, and HNCO, we utilize the non-LTE radiative transfer code, RADEX (244). As inputs of the gas temperatures, we adopt the physical conditions determined in Paper I, using a RADEX analysis of ∼30 transitions of CH_3OH observed with the CSO. As the CSO observations only included single pointings toward B1, encompassing B1a, B1b, and B0d, and toward B2, containing B2a, B2b, and B2d, we only computed the column densities in these six regions. While a similar analysis could be performed for the remainder of B0, previous estimates for the kinetic temperatures and gas densities throughout B0 have not been consistent in the literature (9; 45). It should be noted that further observations could help constrain the physical environment in B0, which would provide contrast to B1 and B2 shocks.

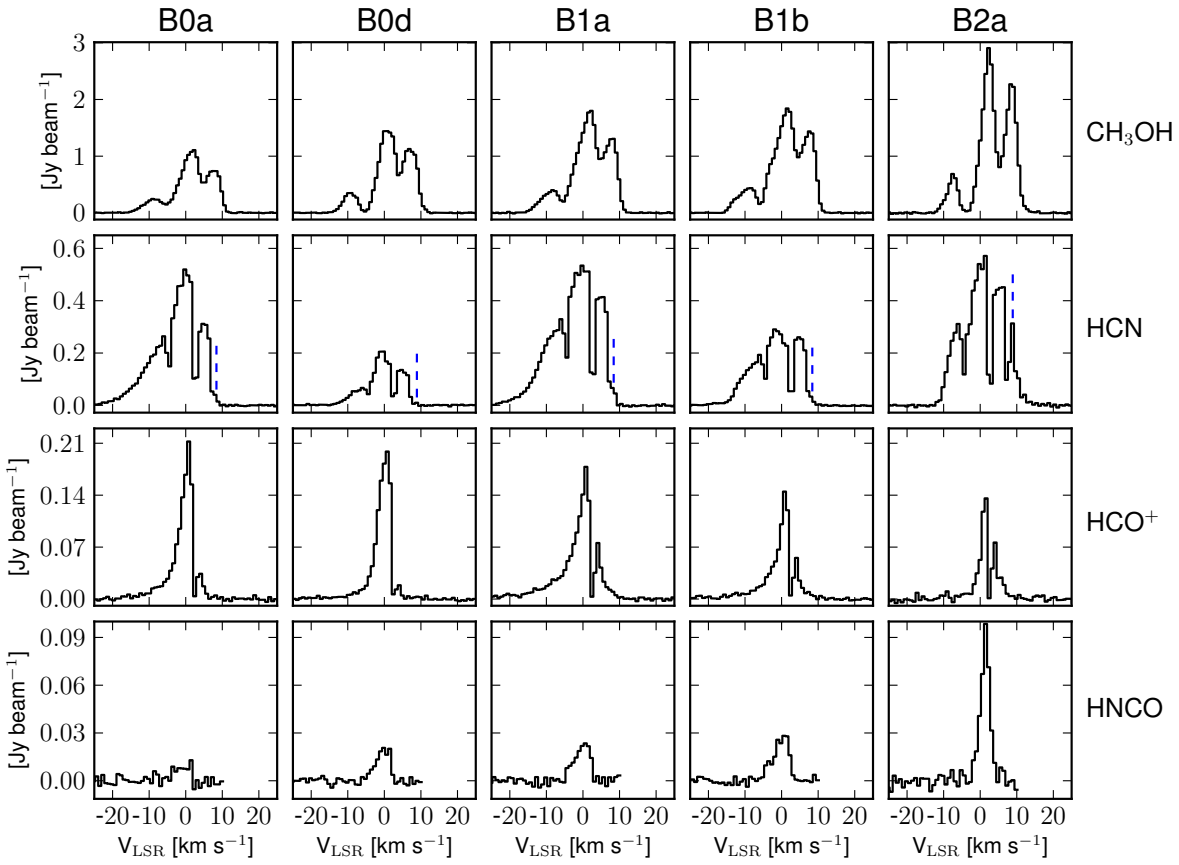

Figure 5.3: The extracted spectra from the regions B0a, B0d, B1a, B1b, and B2a are shown in black. For molecules with multiple transitions, CH_3OH and HCN, the velocities displayed are relative to the rest frequency of the central transition. For HCN, the unknown feature discussed in Section 5.3.2 is marked with a blue dashed line. Not shown is the transition CH_3OH $2_{1,1}$-$1_{1,0}$.

	CH_3OH		HCN			HNCO		
	N	$\frac{N}{N_{H_2}}$	N	$\frac{N}{N_{CH_3OH}}$	$\frac{N}{N_{H_2}}$	N	$\frac{N}{N_{CH_3OH}}$	$\frac{N}{N_{H_2}}$
	(10^{15} cm^{-2})	(10^{-6})	(10^{13} cm^{-2})	(10^{-2})	(10^{-8})	(10^{13} cm^{-2})	(10^{-2})	(10^{-8})
B0d	1.5	1.5	2.6	1.7	2.6	2.5	1.6	2.5
B1a	1.9	1.9	10.	5.3	10.	3.2	1.7	3.2
B1b	2.1	2.1	5.3	2.5	5.3	3.8	1.8	3.8
B2a	2.7	2.7	9.9	3.7	9.9	8.0	3.0	8.0
B2b	1.6	1.6	6.6	4.2	6.6	5.5	3.5	5.5
B2d	2.1	2.0	8.0	3.9	7.9	7.5	3.6	7.5

Table 5.3: Molecular Abundances and Enhancements. For the three molecules studied in depth, the column densities calculated through RADEX are given at each region that coincides with Paper I CSO pointings, along with the enhancement relative to CH_3OH and overall abundance relative to H_2. Errors, as described in Paper I, are calculated to be $\sim$32%

We apply derived parameters of $T_k = 60$ K, $n_{H_2} = 3 \times 10^5$ cm^{-3} toward B1 and $T_k = 50$ K, $n_{H_2} = 6 \times 10^5$ cm^{-3} toward B2. While Paper I used a 2-component fit with an extended, cool component and a compact, warm component, we only adopt the warm component parameters, as the warm component should dominate the emission originating from these small clumps. With these input conditions and line parameters from the Gaussian fits to the spectra, we obtain column densities reported in Table 5.3.

For the purposes of this analysis, the spectral lines without anomalous features, such as non-symmetric broadening, significant self-absorption, and line-blending, were used to constrain the abundances. The individual cases are discussed below. The derived column densities of each species are given in Table 5.3. Liberal uncertainties are assumed due to the small number of transitions observed, asymmetric line profiles, and the inherit uncertainties discussed in Paper I to be $\sim$32%.

We further convert from column densities to abundances with respect to hydrogen. Bachiller and Gutiérrez (8) determined that $N_{H_2} \sim 10^{21}$ cm^{-2} in B1 and $N_{H_2} \sim 5 \times 10^{20}$ cm^{-2} in B2 using the optically thick ^{12}CO line emission and conversion by $N_{H_2} \simeq 10^4 N_{CO}$. However, using measurements on the optically thin isotopologues of CO, such as ^{13}CO, higher column densities are derived. Additionally, multiple authors have suggested that a higher conversion factor of $N_{H_2} \simeq 3 \times 10^4 N_{CO}$ may be more appropriate (26; 136). Given these ambiguities, we adopt $N_{H_2} \sim 2 \times 10^{21}$ cm^{-2} toward B1 and $N_{H_2} \sim 10^{21}$ cm^{-2} toward B2 based on $N_{CO} \sim 9 \times 10^{16}$ cm^{-2} in B1 (136) and $N_{CO} \sim 5 \times 10^{16}$ cm^{-2} in B2 (8)..

Furthermore, roughly half of the CO line flux towards B1 arises within a blueshifted wing component in the velocity range of -15 to -4 km s^{-1}, previously designated the *g2* component (136). This wing component is evident in HCN and HCO^+, but is absent from the profiles of CH_3OH and HNCO, as seen in Figures 5.3 and 5.4. Similar effects have been described by Tafalla et al. (211), but with their designated f-wing to range over -7.5 to -3.5 km s^{-1}, as determined by the transition from optically thin to thick through the ^{13}CO(2-1) to CO(2-1) ratio at each given velocity. Because CH_3OH and HNCO do not exhibit this wing component, we focus on the primary velocity peak, which is more Gaussian shaped.

Taking this feature into account, we estimate that $N_{\rm H_2} \sim 10^{21}$ cm^{-2} in the primary component toward B1, in the *g*2-wing component of B1, and toward B2, in agreement with the derived hydrogen column within the slow wing of Tafalla et al. (211). We assume that this hydrogen column density is the same towards all six clumps. As is typical of abundance measurements, the reported abundances are therefore approximate, and relative abundances determined from lines within this dataset are more precise. Below, we briefly discuss the spectrum of each molecule and observed patterns in column density and abundance.

CH_3OH

We detect the four $2_k - 1_k$ transitions of CH_3OH in all of the clumps used in this study, and we detect weak CH_3OH emission towards the stellar source, consistent with previous observations (94). The relative intensities of the three stronger lines ($2_{-12}-1_{-11}$, $2_{02}-1_{01}$++, $2_{02} - 1_{01}$) remained a very consistent ratio of 4:3:1, respectively, throughout the regions. We note the presence of a small wing on the blue shifted side of the CH_3OH line profiles towards B1a and b and towards B0a, c, d, and e. This wing component spans a velocity range of -4 to -2 km s^{-1}, which is distinct from the $g2$ wing component which extends to -15 km s^{-1}. This has been observed previously by Gómez-Ruiz et al. (94). As was also reported by Gómez-Ruiz et al. (94), CH_3OH emission in L1157B is detected at velocities only slightly blueshifted ($|\Delta v_{\rm LSR}| < 3.5$ km s^{-1}) to the cloud velocity, with generally larger offsets observed at distances further from L1157-mm (Table 5.4). There is also a small, blue wing with a width of $\sim$4 km s^{-1} observed towards B1 and B0a, c, d, and e. Since B1 is located at the apex of the bow shock, this wing may originate from the terminal velocity of the shock as it propagates into cold, dense, unshocked material.

The reported column density for CH_3OH is the SNR-weighted average of the individual column densities derived per transition using RADEX. The column densities remained fairly consistent for the various regions, being on the order of $\sim$1.5-2.7$\times10^{15}$ cm^{-2}. Similarly, the abundances relative to hydrogen are estimated to be $\sim$1.5-2.7$\times10^{-6}$, with the highest abundances toward B2a. These are displayed in Table 5.3. These values are consistent with the results of Paper I, which obtained column densities of $\sim3\times10^{15}$ cm^{-2} from CSO observations towards B1 and B2. The small differences in column densities may be attributed to Paper I's use of a two-component fit in the RADEX analysis, as well as some of the extended emission from CH_3OH in the cooler component being resolved out by CARMA's beam. Given the general agreement with previous observations, we will study the abundance enhancement of other observed molecules relative to methanol.

HCN

HCN has been detected in all clumps studied in L1157B, as well as the stellar source. Velocity offsets of HCN (1-0) were observed to be slightly blueshifted to the systemic velocity, but with no significant gradient over distance from L1157-mm observed. As seen in Figure 5.3, the three hyperfine components are clearly resolved, and we report two anomalous

features.

First, the $F = 0-1$ hyperfine component is seen to be broadened and contains a prominent blueshifted wing toward most clumps in B0 and B1, as seen in previous observations of this line (15). This component is associated with the $g2$ component observed in CO (136) as well as in HCO^+ in our observations. Here, the lower-frequency edge of the blue wing was set by where the morphology of the line emission significantly changed before the peak of the $F = 0 - 1$ transition. The integrated HCN (1-0) emission in the velocity range of -15 to -4 km s^{-1}, with respect to the $F = 0 - 1$ hyperfine component, is shown in Figure 5.4 overlaid on HCO^+ emission within this velocity range. This velocity component clearly maps to the apex and eastern wall of C2 and is notably absent toward B2. This may imply that the wing emission originates from the shock as it propagates through the semi-processed material between C1 and C2, and thus has not been significantly slowed down. This is further evidenced by SiO emission, which displays broader velocity wings ($\sim$20 km s^{-1}) (94). This will be further discussed later.

The second anomalous feature in the spectrum is a strong line at $\sim$4 km s^{-1}, with respect to the $F = 1 - 1$ transition, toward B2a, B2b, and B2d. This can be seen in B2a of HCN in Figure 5.3. The integrated emission of this fourth component can be seen in Figure 5.5 to be nearly exclusively in B2. The flux observed in B1a and the eastern wall of B0 is blended emission from the red tail of the $F = 1 - 1$ line and not a separate component. This supposed fourth line could be explained by a second, prominent velocity component redshifted by approximately the hyperfine spacing. This would result in the central two observed features being a blend of two components, $F = 2 - 1/F = 0 - 1$ and $F = 1 - 1/F = 2 - 1$ for the second and third most blueshifted features, respectively. Meanwhile, the outer two features are unblended, single-transition features $F = 0 - 1$ and $F = 1 - 1$ for the first and fourth most blueshifted features, respectively. However, the relative emission strengths of the hyperfine components do not clearly indicate this is the case. Further, it is curious that a red-shifted component is not apparent in the spectral lines of other species observed in B2, and no similar feature has been reported in the literature for another molecule. But if the feature is a second velocity component, then this would provide further evidence that B2c is kinematically related to the apex of C2, and not to the rest of B2. Another possible explanation could be that this is an unidentified line of a separate species, which may explain why it is primarily in B2, similar to HNCO. However, it seems unlikely that we would observe an unknown transition of similar strength to HCN (1-0), with no reasonable candidate transitions within the NRAO Splatalogue database[1]. Observation of the HCN (2-1) has the potential to clarify the scenario.

Finally, the observed line intensity ratios of HCN were distinct from the optically thin, LTE hyperfine line ratios of $F = (2-1) : (1-1) : (0-1) = 5 : 3 : 1$. The observed ratios are about $\sim 1.76 : 1.35 : 1$, respectively. While we do not expect LTE conditions, these line ratios cannot be accounted for by RADEX under physical conditions consistent with previous observations of L1157. This may indicate a pumping process producing weak masing, which should be accounted for by RADEX. It is also possible that, in part, the

[1] Available at `www.splatalogue.net` (188)

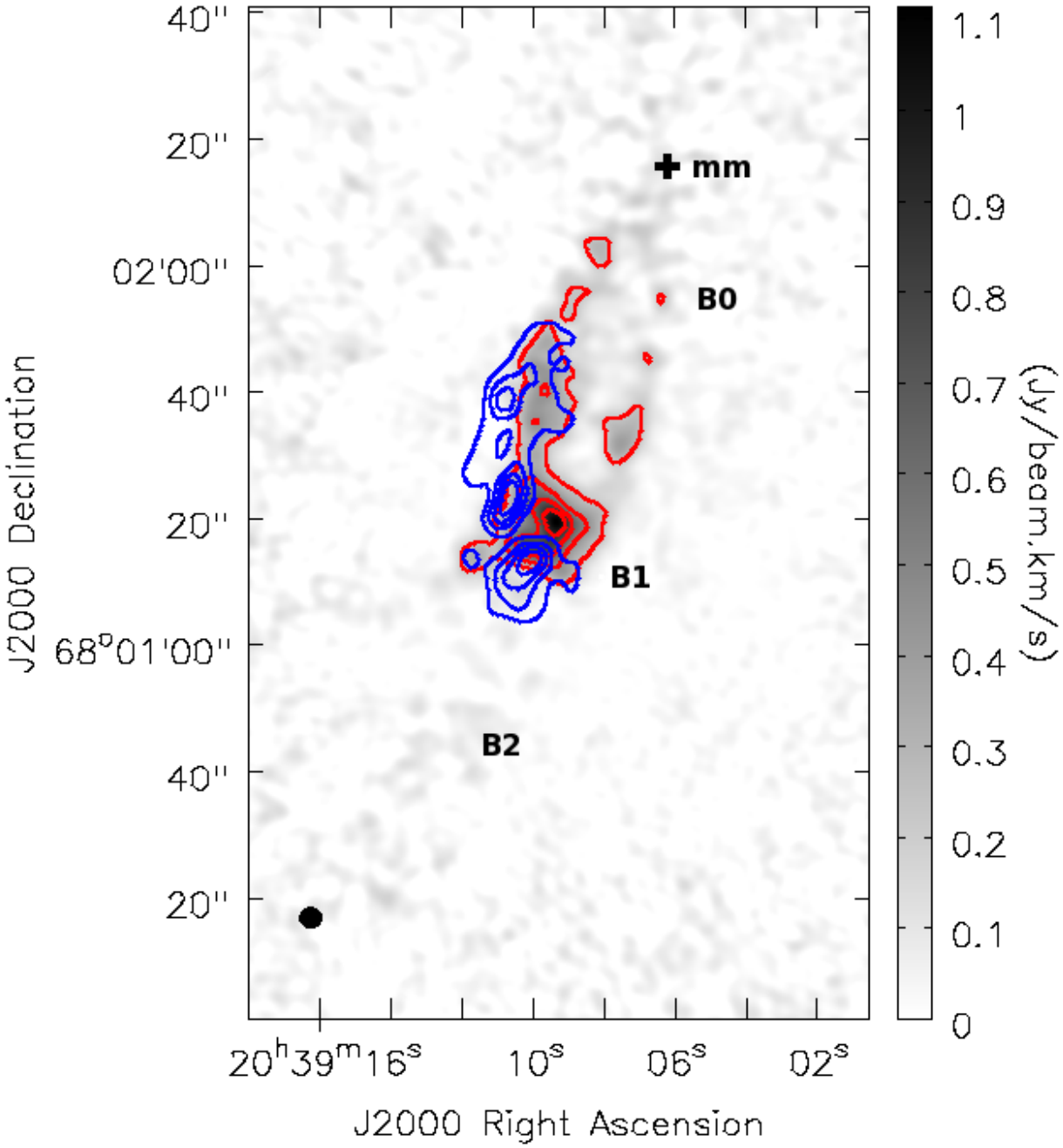

Figure 5.4: Integrated emission maps of the blue wing component of HCN (1-0) (blue contours at levels of 0.5, 1.0, 1.5, & 2.0 Jy beam^{-1} km s^{-1}) and HCO$^+$ (1-0) (raster, red contours at levels of 0.22, 0.45, 0.67, & 0.89 Jy beam^{-1}). The velocity ranges of integration were both -15 to +4 km s^{-1}. The synthesized beam size is displayed as filled black in the lower left.

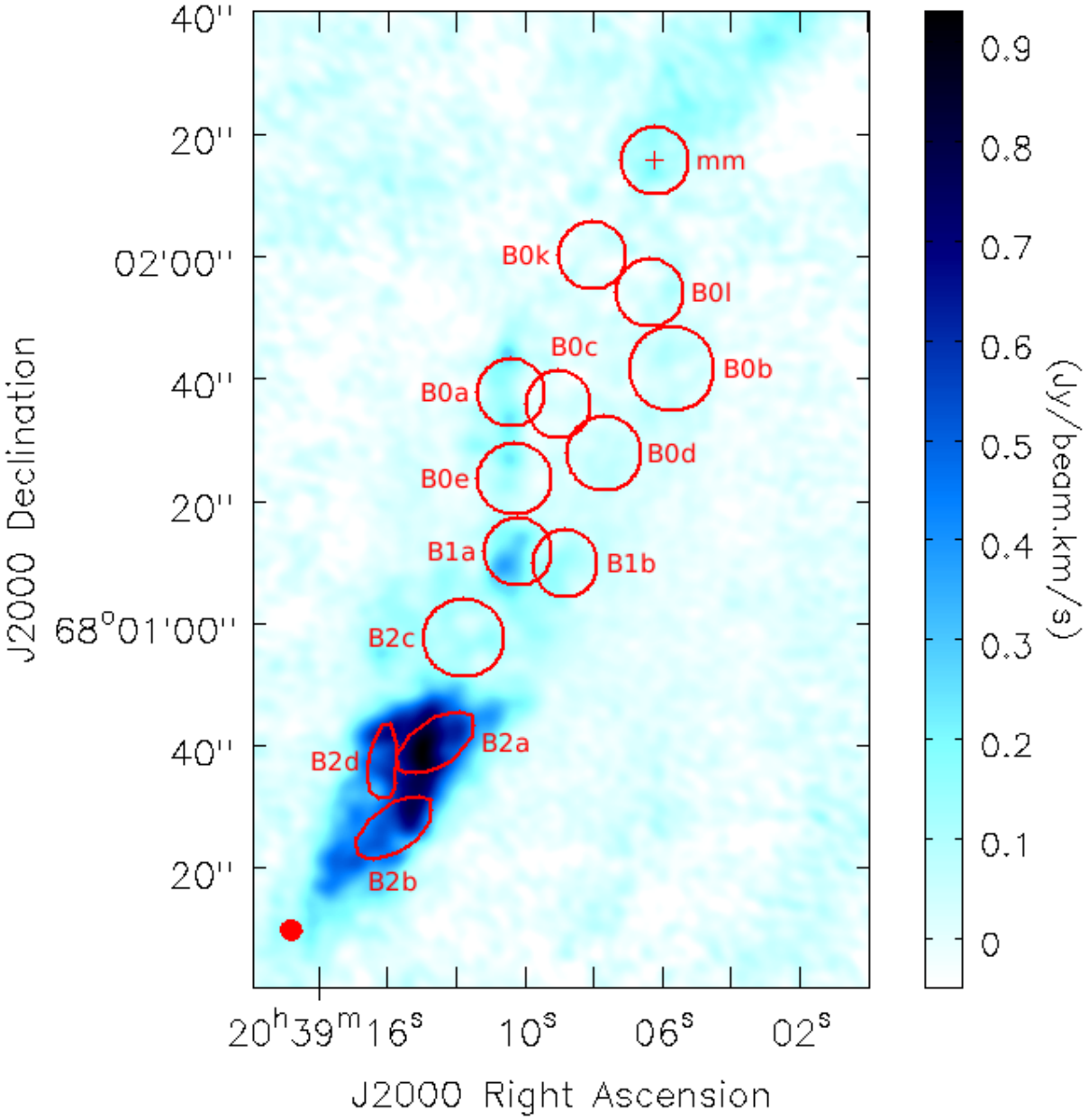

Figure 5.5: Integrated emission maps of the 4th unknown component near HCN (1-0), with the regions defined in Table 5.2 displayed in red, along with the stellar source. The synthesized beam size is displayed as filled red in the lower left.

potential two blended velocity components discussed previously may cause some of the deviation from the thermal line ratios. Recent work by Mullins et al. (171) on anomalous hyperfine line strengths also point to a strong dependency on optical depth in combination with gas infall or dynamics as a potential explanation of these observed ratios.

Because the blue wing component appears to be associated with different gas than the clumps, we report HCN column densities from RADEX calculations solely on the $F = 1 - 1$ transition. This hyperfine line should not include substantial flux contributed by the blue shifted wing. It has been previously shown that accurate modeling of HCN hyperfine transitions requires that radiative transfer calculations be explicitly applied to each F-level independently. In particular, the $J = 1 - 0$, $F = 0 - 1$ transition is prone to producing spurious results, especially when the line ratios are not well-described by a single excitation temperature (171). The derived column densities are of order $10^{13} - 10^{14}$ cm^{-2}, as shown in Table 5.3, with higher column densities toward B1a and B2. The HCN to CH_3OH column density ratio varied between $1.7 - 5.3 \times 10^{-2}$. Benedettini et al. (15) reported larger column densities by up to an order of magnitude in all regions except B0d. However, they derived their column densities assuming LTE, whereas we utilized the non-LTE code RADEX (244). The non-LTE approach is likely more accuate, especially given the non-thermal hyperfine ratios.

Benedettini et al. (15) report that HCN (1-0) undergoes strong self-absorption in observations toward L1157B, which would result in an underestimation of their reported column density. It is interesting to note that toward all regions in L1157B the troughs between the hyperfine features lie very close to what would result from HCN residing in ambient gas (i.e. shifted by the systemic velocity of $\sim$2.7 km s^{-1}). The red side of each of these features also appears to fall off with slopes that are not indicative of a typical Gaussian profile, suggesting the line may be significantly self-absorbed. A possible analogous absorption feature is also observed in the HCO^+ (1-0) emission. It does not appear that CH_3OH or HNCO have similar self-absorption features.

If the observed profiles for HCN are indeed due to self-absorption, the abundances derived here would be underestimated. As a result, the molecular enhancements would be even larger than those determined here. We do not have sufficient data to make a claim as to the likelihood that this is self-absorption, but we suggest this may be an intriguing avenue for follow-up study.

HCO+

HCO^+ has been detected toward each region in L1157B and in the stellar source. As seen in Figure 5.3, the emission displays significant self-absorption toward all positions in the outflow at a velocity of 3$-$4 km s^{-1}. However, this self-absorption is not detected towards the stellar source. Due to the non-Gaussian line shapes and the self-absorption, we do not fit the spectra or determine HCO^+ column densities here.

The blueshifted $g2$ wing of HCO^+ (1-0) is observed, spanning a similar velocity range of HCN (1-0). As shown in Figure 5.4, both of these blueshifted components map to the apex and eastern wall of C2, implying that the source of these emission wings may origi-

nate from the same physical structure. Figure 5.6 shows blue wing ($v_{\rm LSR}$ =-15 to -3.86 km s^{-1}) and red wing ($v_{\rm LSR}$ =4.3 to 10 km s^{-1}) of the HCO$^+$ emission along with the central peak ($v_{\rm LSR}$ =-3 to 3.5 km s^{-1}). The transition from the blue wing to the central peak was determined by where the morphology significantly changed, as discussed above, while the red wing/central peak boundary was the velocity where the self-absorption was strong enough to make the observed line strength effectively zero. Here, the central peak is observed to trace the ambient gas throughout the C1 cavity, with a slight peak along the ridge. The redshifted emission continues far past the stellar source, as would be expected. Interestingly, there are also redshifted components also observed at concentrated peaks along the apex of B0/1, B0ℓ, and B2. While these are not necessarily separate components, it is possible that the emission originates from gas from the far side of the C1 and C2 cavity.

HNCO

HNCO was detected toward all of the regions in L1157B, but not toward the stellar source. Although weak, a wing component from -3 to -1 km s^{-1} is apparent in the spectra towards B1 and the ridge of B0. This occupies the same velocity range and general spatial distribution as the weak wing component in CH_3OH, but is distinct from the $g2$ component evident in the spectra of HCN and HCO$^+$. Our RADEX calculations based on our Gaussian fits determine the column densities of HNCO to vary between $\sim$2.5-8.0$\times10^{13}$ cm^{-2} across the entire line, comparable to the measured column densities of HCN. A factor of 2 increase in column density between B2 and B1 is immediately apparent. This corresponds to the N(HNCO)/N(CH_3OH) increasing by a factor of 2 ($\sim$1.7$\times10^{-2}$ to $\sim$3.5$\times19^{-2}$) and similar for abundance enhancement relative to H_2, which is consistent with previous observations (165).

CH_3CN

A significant feature appears in three edge channels of one of our windows. Given a similar velocity profile as our other observed molecules, the transition appears to coincide with the $5_k - 4_k$ transition of CH_3CN. The integrated emission of these three channels display a distribution similar to CH_3OH, with significant emission observed throughout the major shocked regions of L1157B. Very little emission appears to come from any of the less prominent shocks and ambient gas. It has been detected previously in B1 in $14_k - 13_k$ (7) and mapped in $8_k - 7_k$ (48), with a distribution consistent with our observations. These both report column densities between 10^{12}-10^{13} cm^{-2}.

5.4 Discussion

A few trends emerge from the results. First, it is apparent that the northernmost clumps in B0 are kinematically distinct from the material in the south of the ridge. Further, the clumps in B1 and south of the ridge in B0 are more kinematically and structurally similar

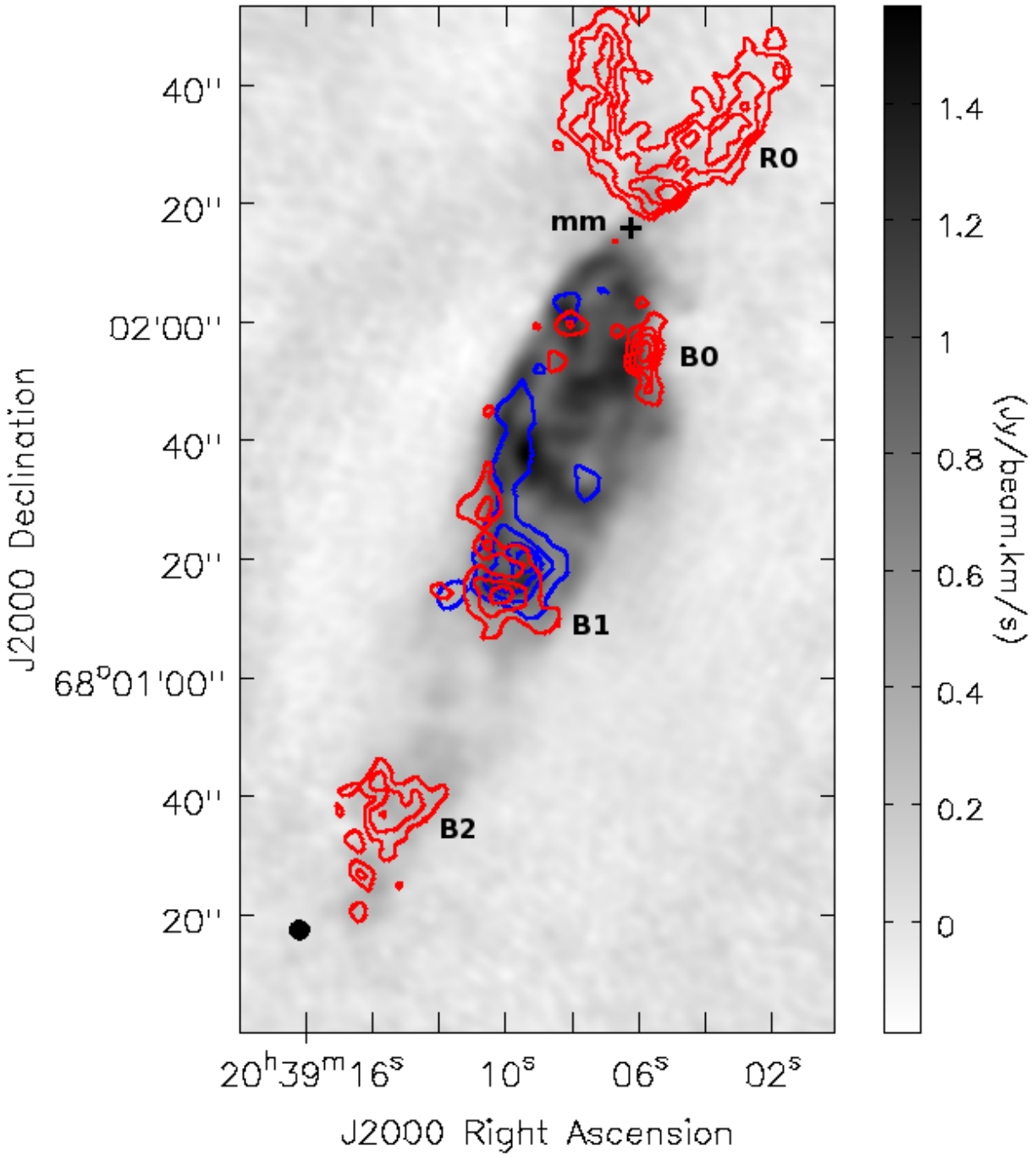

Figure 5.6: Integrated emission map of HCO^+ (1-0) with contours of its blue wing (-15 to -3.86 km s^{-1} at levels of 0.18, 0.37, 0.55, & 0.74 Jy $beam^{-1}$) and red wings (+4.3 to +10 km s^{-1} at levels of 0.08, 0.16, 0.24, & 0.33 Jy $beam^{-1}$) in their respective colors over the central peak raster (-3 to +3.5 km s^{-1}). The synthesized beam size is displayed as filled black in the lower left.

compared to northern B0. Second, a broad ($\sim$15 km s^{-1}) component, referred to as $g2$, has been observed in HCN and HCO^+, as well as CO and SiO in previous work (136). It is predominately located along the eastern wall of the C2 cavity and near the apex of C2, most significantly towards B0e. This component contributes a significant fraction of the molecular line emission by these species in the eastern portion of C2. Furthermore, we notice possible east-west differentiation within C2 and also between B1 and B2.

5.4.1 East/West Chemical Contrast in C2

Previous literature has discussed the existence of a chemical differentiation within C2 (9; 15; 16; 87; 212). While species including HCN and SiO produce strong line emission along the eastern wall of C2, other molecules such as CH_3OH and OCS are seen stronger along the western wall, especially towards the apex. We observe this trend in the species studied here as well. In our CARMA images, CH_3OH is seen to be strongest at the western wall of B1 and along the ridge in B0, although this relative abundance enhancement is less significant compared to the other studied species. With the first interferrometric maps of HNCO presented here, it can be seen that this species is even more concentrated to the eastern wall of C2 than CH_3OH. Meanwhile, HCN is substantially stronger on the eastern wall compared to the western. As the $g2$ component preferentially contributes to the emission seen in the eastern wall, it is plausible that the apparent differentiation results from the contribution of this wing. However, considering only the emission by the HCN (1-0) $F = 1 - 1$ transition, for which the wing component should not contribute substantially, it appears that the east-west differentiation still persists. As reported previously, the column density of CH_3OH is relatively consistent near the apex of C2, while a significant enhancement is observed for HCN in B1a over B1b (16). In our analysis, we found this to be an increase of column density of about a factor of two, which is a similar enhancement found along the eastern wall up to the ridge.

Bachiller et al. (9) assert such chemical segregation is due to chemical stratification within the cloud. Gueth et al. (86) proposed that as the precessing jet sweeps from east to west, the western wall of C2 would be interacting with new, unshocked material in the molecular cloud. Meanwhile, the eastern wall is expanding into material already processed during the previous shock that produced C1.

In the western wall, especially towards the apex in B1, abundances would be indicative of protypical ice mantle desorption as the shock interacts with grains that previously resided in cool, quiescent gas. This results in an enhancement of grain-species, which we observe with CH_3OH and HNCO. On the other hand, the eastern wall is interacting with dust grains that have already been recently shocked by the B2 event. As a result, the ice mantles would not have had time to redeposit onto the surface of the grains. The shock would instead destroy the complex species that were brought into the gas phase during the first shock, and further erode the bare dust grain. The resulting products of these complex molecules would then be enhanced in these regions, as seen in HCN and HCO^+. This is supported by the reported anti-correlation of CN and HNCO in this region (196), as CN is

likely to be the product of this destruction. In addition, this also explains the distribution of SiO toward the eastern wall of C2, as it would be enhanced in the shocking of bare-grains compared to grains with significant ice-mantles. In Benedettini et al. (15), emission from HC_3N, HCN, CS, NH_3, and SiO were found to be brighter in eastern clumps in C2, while CH_3OH, OCS, and ^{34}SO emissions were more prominent in western clumps. The segregation of these specific species aligns with our proposed scenario.

This scenario is further supported by the velocity wings observed in these species. While the chemical differentiation within C2 is seen both in the wing and the primary velocity components, the wing components probe the properties of the shock that would affect the chemistry in the entire region. CH_3OH and HNCO are observed to have a small, $\sim$4 km s^{-1} blue wing primarily towards B1b, as was previously discussed. This wing could be tracing the shock as it hits, and is thus slowed down, by the cold, dense, and unshocked gas. Meanwhile, HCO^+ and HCN are observed to have a large, blue, $g2$ wing primarily towards B1a and the eastern wall of C2. Here, the shock would not be slowed down because it is interacting with gas that has already been processed and recently shocked, and thus is less dense than towards B1b. This higher velocity scenario is also supported by the higher abundance of SiO towards the eastern wall, as it is produced more efficiently in high-velocity shocks, and where the dust grains are already bare due to the previous shock.

It should be noted that observations by Gómez-Ruiz et al. (94) of a pair of H_2CO lines with differences of excitation energies of $\Delta T \sim 47$ K show significantly different emission on opposite edges of B1, suggesting these asymmetries could instead be due to excitation effects. However, the majority of the lines studied here have relatively low excitations and still display chemical differentiation. A follow up study of higher energy transitions of these species would help determine the significance of excitation on the chemical differentiation in C2. Recent observations of isotopologues of CO by Kwon et al. (133) may suggest that there are in fact two bipolar jets, each of which could contribute to a different wall of C2. While this may explain the asymmetric brightness of certain lines, this does not necessarily explain the distinct chemical segregation within the region.

5.4.2 Enhancements in B2

Among the species studied, abundances toward the shocked regions in B2 were found to be either equivalent or higher compared to the B1 shocks. The abundance relative to H_2 of HCN toward B2a and B1a are nearly equivalent. For CH_3OH, B2 appears to be enhanced, although it is only just outside of our reported uncertainties. And in HNCO, we see a factor of two increase in abundance relative to CH_3OH. Meanwhile, HCO^+ emission is significantly weaker in B2 relative to B0 and B1. To determine what may cause this difference, it is necessary to determine how B1 and B2 vary.

Since the shock in B2 is older than in B1, the observed abundances could be a result of viewing changes on a chemically-relevant timescale. If this proves significant, then it would imply that the initial liberation of molecules from the grain by the shock may not

be the only prominent process that occurs in these environments. Instead, post-shock, gas-phase reactions would become significant, as these regions are at higher densities and temperatures than the pre-shock environments. Examples of these will be discussed briefly in Section 5.4.3.

Gómez-Ruiz et al. (94) have also proposed that the shock in B2 is $\sim$10 km s^{-1} faster than B1 from observations of SiO and its line profile. Higher shock velocities can result in more efficient erosion of ices on grain surfaces and the mantles themselves, as has been shown in models of sputtering on grains. (117; 227). If this difference in shock velocities is significant to the proceeding chemistry, then the higher abundances of CH_3OH and HNCO could be explained by a higher liberation rate from the grain.

5.4.3 Formation Chemistry Implications

CH_3OH

Overall, the consistent abundance of CH_3OH indicates that its primary source is from the liberation of grains during the shock. The slightly higher abundances toward the relatively cooler, older shock, B2, may imply that the CH_3OH may have a production pathway as the young shock-tracing molecules react following their initial release into the gas phase. Chemical models of outflows have shown that methanol abundance is elevated in higher gas density regions, from 10^5 to 10^6 cm^{-3} (228). This difference in density was observed when comparing the gas densities of B1 and B2 from Paper I, supporting this interpretation. Rawlings et al. (186) has discussed that recently shocked material surrounding the grains is at high enough densities that three-body reactions may occur efficiently, such as with CH_3, OH, and H_2O (as a passive third body) to produce CH_3OH. It is also possible that the larger shock velocity in B2 relative to B1, as proposed by Gómez-Ruiz et al. (94), could result in a more efficient liberation of grain species.

HCN

If the scenario proposed for the east/west chemical differentiation is valid, then the formation of HCN would be significantly impacted by the formation of CN from the destruction of more complex species in the gas phase. Following the enhancement of CN in the region, HCN could be readily produced as well. Similar iterations of this interpretation have been proposed by Benedettini et al. (15).

HCO^+

The strong emission of HCO^+ toward the region not directly associated with the shock front, B0, is consistent with previous work, where the molecule is thought to be rapidly produced in the gas phase. Rawlings et al. (185) found that HCO^+ is enhanced in the boundary layer between the jet and the surrounding ambient gas, which is observed here. Within this region, the shock will cause H_2O and CH_3OH to be lifted from the grains. With

these species abundant in the gas phase, sufficient amounts of the ions H_3O^+ and $CH_3OH_2^+$ can be formed to rapidly produce HCO^+. Once HCO^+ resides in this high-temperature, water-rich environment, it may then be efficiently destroyed through dissociative recombination (9) or through a reaction with H_2O (19). Bergin et al. (19) found that HCO^+ could be efficiently converted into H_3O^+ and CO on the order of 100 years, or the approximate timescale of the shock passage modeled. This points to the eastern wall of C2 being the site of a recent interaction, as observed by the wing feature of HCN and HCO^+ seen towards this region. Then, as the shock evolves, the HCO^+ is rapidly destroyed, as evidenced by the weaker emission toward B1 and B2.

HNCO

HNCO has been studied in gas-grain warm-up chemical models of hot corinos, and was found to be formed through the gas-phase destruction of more complex molecules after they are lifted from the grain surface (78; 184). In the high temperature phase of the hot core models, the gas-phase abundances were found to be only 2×10^{-9}. However in some models, the peak abundance on the grain prior to desorption due to the warm up, was as high as $\sim10^{-8}$–10^{-7}.

Hypothetically, this would imply that, in a hot-core-like environment, the observed abundances could be explained by all of the HNCO on the grain suddenly being lifted from the grain. However, Rodríguez-Fernández et al. (196) argue that the gas-phase chemistry within shocks should differ due its higher temperatures and densities over a short period of time. They propose the dominant pathways to be a) the initial grain erosion increasing the HNCO then b) neutral-neutral gas phase reaction of CN and O_2 to produce OCN, which may be favored due to the significant enhancement of O_2 within the post-shock gas (19; 91). The OCN can then be rapidly converted into HNCO.

This formation pathway is consistent with the fact that HNCO is currently the only non-sulfur-bearing molecule observed to have significantly greater enhancement in B2 than B1. This is because the efficient formation of both HNCO and several sulfur-bearing species (i.e. SO and SO_2) heavily relies on molecules reacting with the abundant species O_2, converting CN to HNCO, and H_2S to SO and SO_2. CN and HNCO have anticorrelated physical distributions, supporting this pathway (196). Further observations of other species associated with the O_2 chemistry in shocks may help constrain the significance of this pathway. Again, the cause of this enhancement may also be due to B2's high shock velocity compared to B1.

5.5 Conclusions

We report high-resolution interferometric maps of emission from CH_3OH, HCN, HCO^+, and HNCO toward the southern outflow of L1157 from CARMA observations. In addition to defining three new clumps (B0k, B0ℓ, and B2d), we utilized the non-LTE code RADEX to constrain the column densities and abundances of three of our species. We find:

- The abundance of CH_3OH is relatively consistent across the regions and appears to be primarily produced by the liberation off of grain surfaces due to shocks
- Both HCN/HCO^+ and CH_3OH/HNCO display velocity profiles that are indicative of their originating from the same physical regions
- The east/west chemical differentiation observed in B0 and B1 could be explained by the difference in shock-chemistry that occurs when the impacted medium is cold, dense, and quiescent or warm, diffuse, and previously-shocked, as evidenced by the molecular enhancement and velocity profiles
- Through the first interferrometric maps of HNCO, enhanced abundances are seen toward B2 relative to B1, which may be explained by the importance of the formation of O_2 in shocked regions or by differences in shock velocities.

5.6 Acknowledgments

EH, AMB, and CNS thank the National Science Foundation (NSF) for continuing to support the astrochemistry program at the University of Virginia and the NASA Exobiology and Evolutionary Biology Program through a subcontract from Rensselaer Polytechnic Institute. NMD gratefully acknowledges funding by the National Radio Astronomy Observatory Summer Research Internship, a Research Experience for Undergraduates funded by the NSF and Peter Teuben for helpful discussion. BAM gratefully acknowledges funding by an NSF Graduate Research Fellowship during initial portions of this work. The National Radio Astronomy Observatory is a facility of the National Science Foundation operated under cooperative agreement by Associated Universities, Inc. Portions of this material are based upon work at the Caltech Submillimeter Observatory, which was operated by the California Institute of Technology under cooperative agreement with the National Science Foundation (AST-0838261). Support for CARMA construction was derived from the Gordon and Betty Moore Foundation, the Kenneth T. and Eileen L. Norris Foundation, the James S. McDonnell Foundation, the Associates of the California Institute of Technology, the University of Chicago, the states of California, Illinois, and Maryland, and the National Science Foundation. CARMA development and operations were supported by the National Science Foundation under a cooperative agreement, and by the CARMA partner universities.

5.7 Spectra for All Molecules and Regions

For each of the species observed with CARMA (see Table 5.1), the spectra for all of the defined regions in Table 5.2 are provided below. For species with multiple transitions, CH_3OH and HCN, the velocities displayed are relative to the rest frequency of the central

transition. For HCN, the unknown feature discussed in Section 5.3.2 is marked with a blue dashed line.

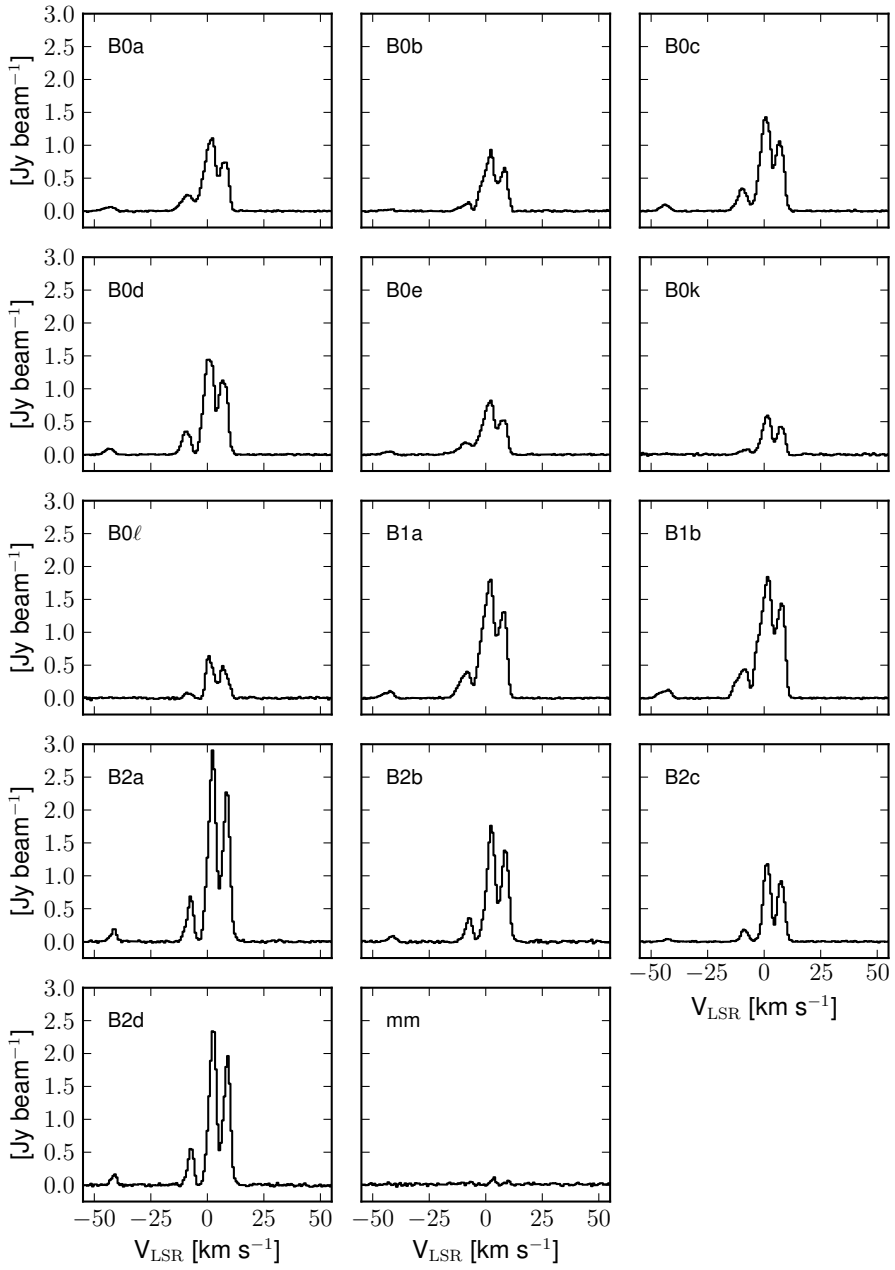

Figure 5.7: Extracted spectra of all regions in Table 5.2 for CH_3OH emission from the CARMA observations.

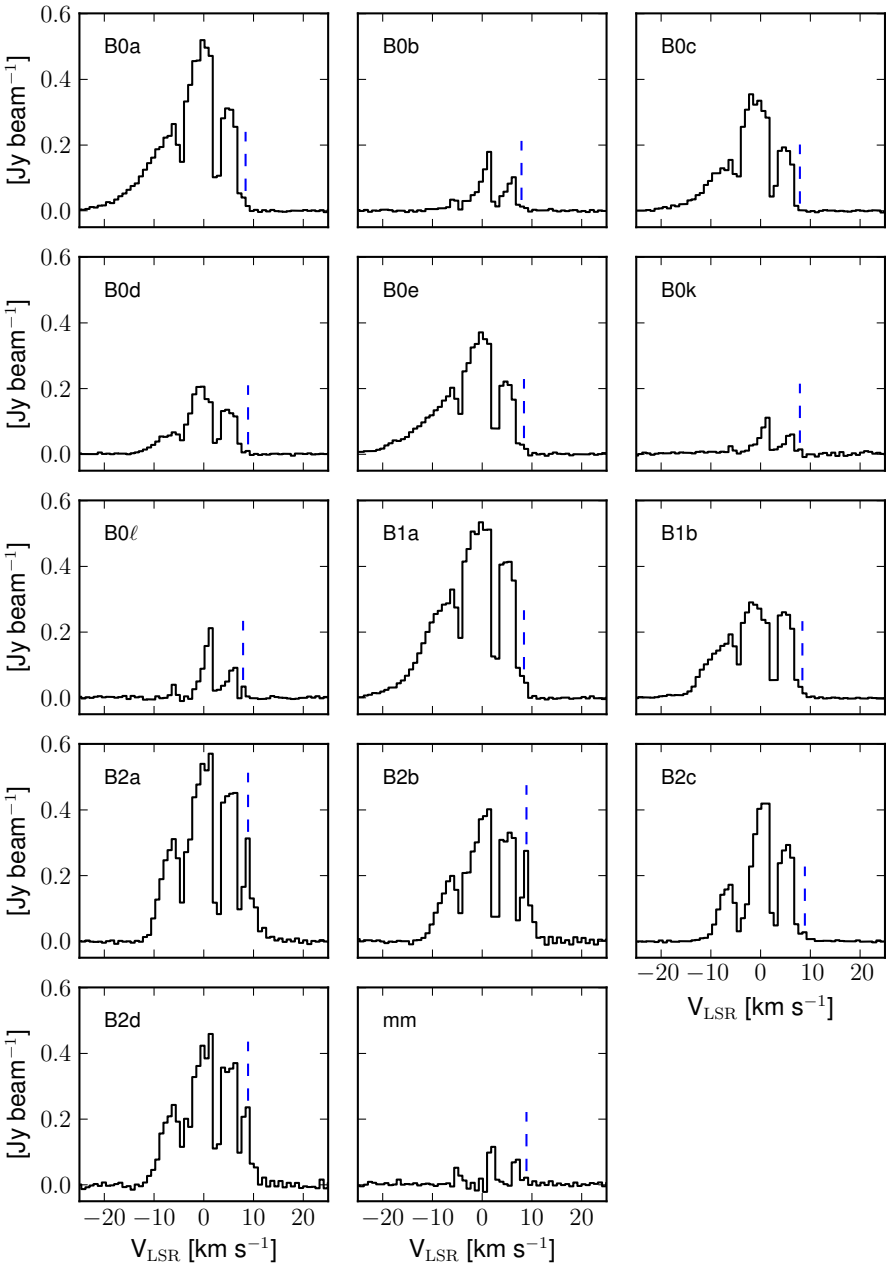

Figure 5.8: Extracted spectra of all regions in Table 5.2 for HCN emission from the CARMA observations. The unknown feature is marked with a blue dashed line.

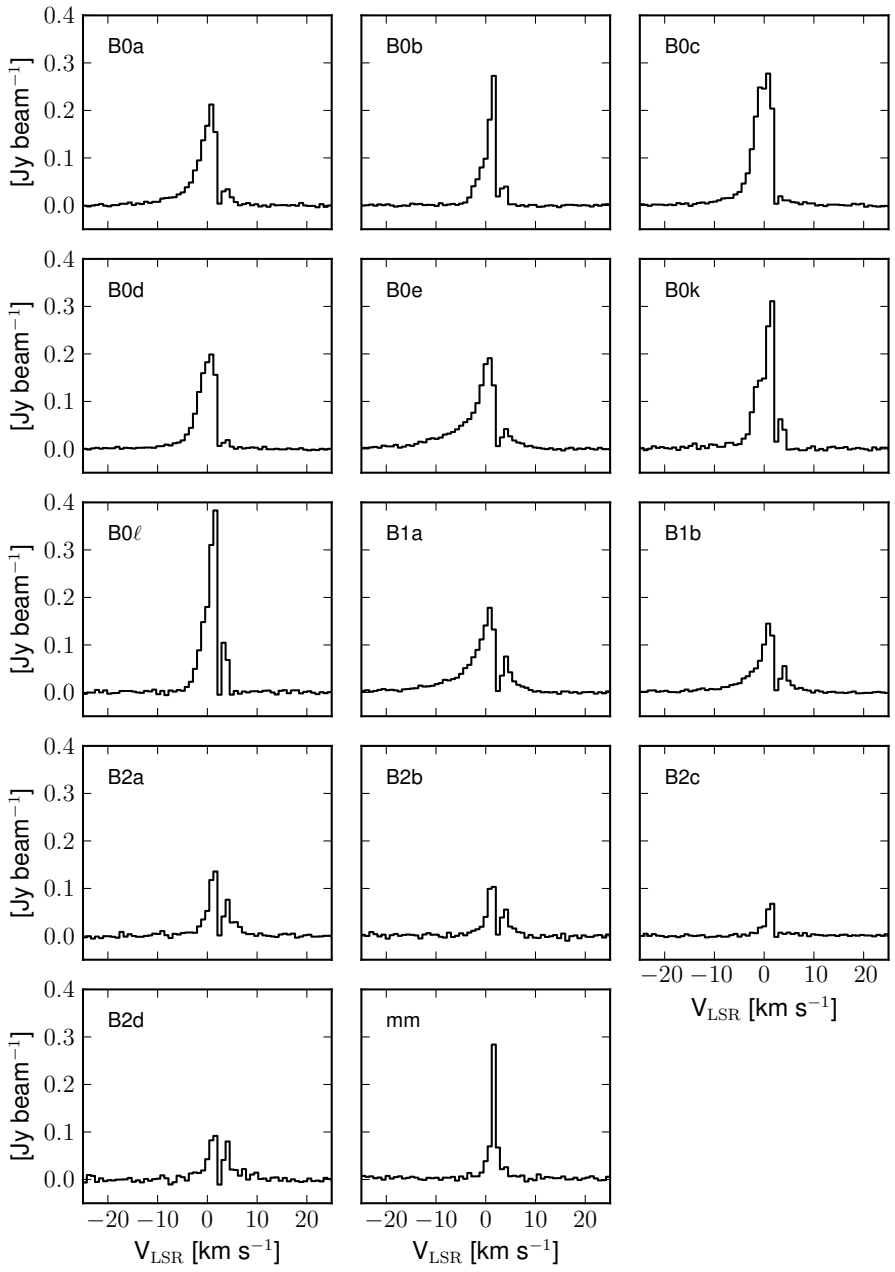

Figure 5.9: Extracted spectra of all regions in Table 5.2 for HCO^+ emission from the CARMA observations.

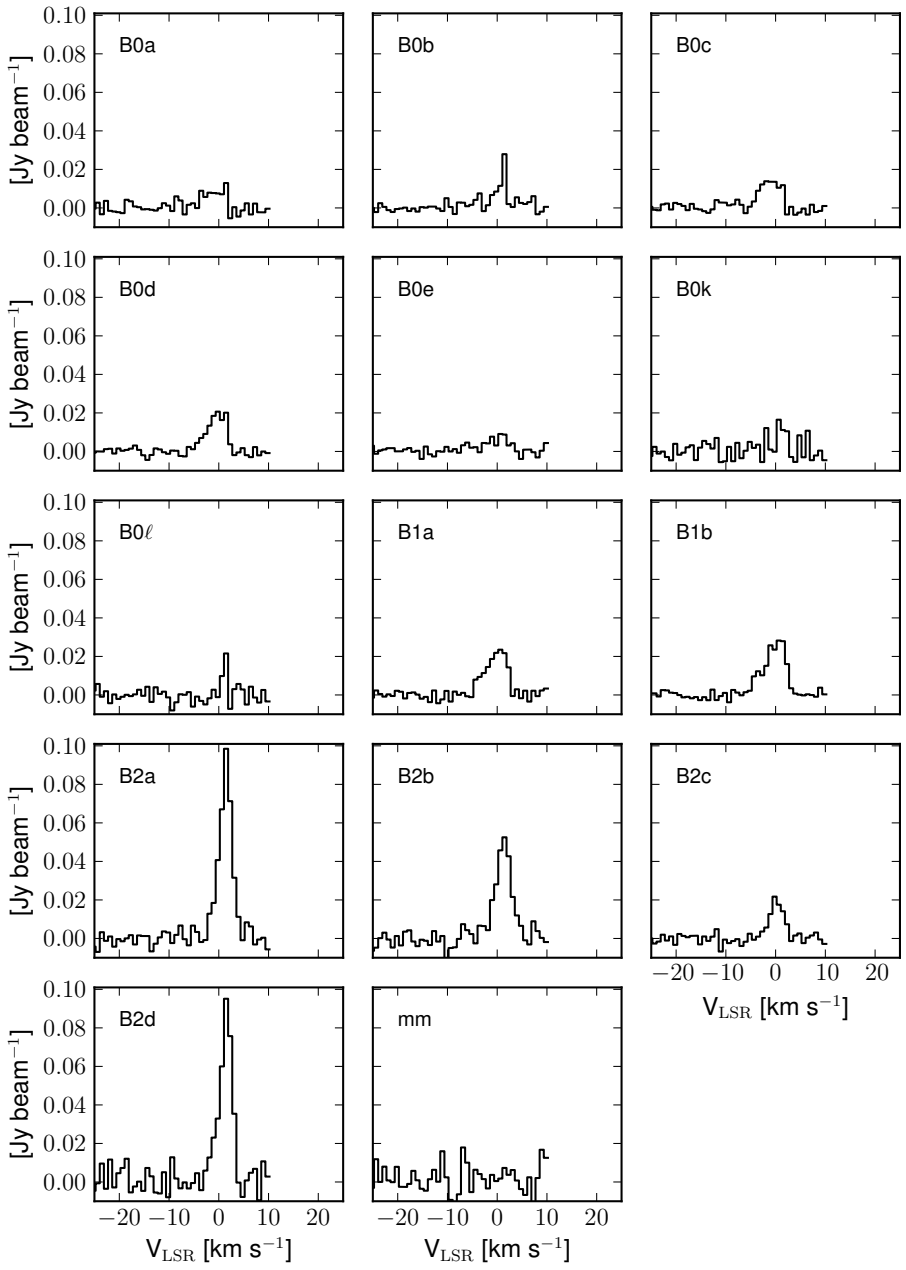

Figure 5.10: Extracted spectra of all regions in Table 5.2 for HNCO emission from the CARMA observations.

5.8 Tables of Spectral Fits for All Molecules and Regions

For each of the species observed with CARMA (see Table 5.1), the parameters of the Gaussian fits of the spectra are tabulated below for all of the defined regions in Table 5.2. Gaussian profiles were generated utilizing a modified version of the line fitting code described in Corby et al. (52). The fourth column in Tables 5.4 and 5.5 and third column in Table 5.6 shows the LSR velocity of the line peak. For HCN, the unknown feature seen in B2 is listed as the "4^{th} component."

Table 5.4: CH_3OH Spectral Fits

Region	Transition	Peak (K)	v_{LSR} (km s^{-1})	Line Width (km s^{-1})
B0a	$2_{-1,2} - 1_{-1,1}$	2.92	1.30	3.63
	$2_{0,2} - 1_{0,1}$++	4.25	1.02	6.26
	$2_{0,2} - 1_{0,1}$	0.91	0.81	7.03
	$2_{1,1} - 1_{1,0}$	0.24	0.00	5.48
B0b	$2_{-1,2} - 1_{-1,1}$	2.37	1.70	3.32
	$2_{0,2} - 1_{0,1}$++	3.20	1.30	6.82
	$2_{0,2} - 1_{0,1}$	0.42	0.59	5.05
	$2_{1,1} - 1_{1,0}$	0.08	0.28	5.86
B0c	$2_{-1,2} - 1_{-1,1}$	4.13	0.46	3.94
	$2_{0,2} - 1_{0,1}$++	5.60	0.28	5.58
	$2_{0,2} - 1_{0,1}$	1.31	-0.15	5.14
	$2_{1,1} - 1_{1,0}$	0.38	-0.46	4.59
B0d	$2_{-1,2} - 1_{-1,1}$	4.58	0.62	4.12
	$2_{0,2} - 1_{0,1}$++	5.93	0.40	5.33
	$2_{0,2} - 1_{0,1}$	1.44	0.06	4.25
	$2_{1,1} - 1_{1,0}$	0.36	0.06	4.37
B0e	$2_{-1,2} - 1_{-1,1}$	2.03	1.36	3.59
	$2_{0,2} - 1_{0,1}$++	3.08	1.21	6.23
	$2_{0,2} - 1_{0,1}$	0.66	1.46	9.48
	$2_{1,1} - 1_{1,0}$	0.18	0.34	4.65
B0k	$2_{-1,2} - 1_{-1,1}$	1.76	0.96	3.59
	$2_{0,2} - 1_{0,1}$++	2.32	0.87	4.77
	$2_{0,2} - 1_{0,1}$	0.27	1.58	6.69
	$2_{1,1} - 1_{1,0}$	0.05	0.19	3.81
B0ℓ	$2_{-1,2} - 1_{-1,1}$	1.77	0.53	4.80
	$2_{0,2} - 1_{0,1}$++	2.51	0.56	3.59
	$2_{0,2} - 1_{0,1}$	0.31	0.96	3.66
	$2_{1,1} - 1_{1,0}$	-	-	-
B1a	$2_{-1,2} - 1_{-1,1}$	4.78	1.39	3.38
	$2_{0,2} - 1_{0,1}$++	6.68	1.05	7.00
	$2_{0,2} - 1_{0,1}$	1.45	0.40	6.35
	$2_{1,1} - 1_{1,0}$	0.38	0.31	5.36
B1b	$2_{-1,2} - 1_{-1,1}$	5.16	1.24	3.41
	$2_{0,2} - 1_{0,1}$++	6.79	0.81	7.44
	$2_{0,2} - 1_{0,1}$	1.63	-0.34	6.10
	$2_{1,1} - 1_{1,0}$	0.47	-0.28	5.98
B2a	$2_{-1,2} - 1_{-1,1}$	9.04	1.86	3.53
	$2_{0,2} - 1_{0,1}$++	10.80	1.83	4.18
	$2_{0,2} - 1_{0,1}$	2.57	1.89	3.41
	$2_{1,1} - 1_{1,0}$	0.72	1.98	3.04
B2b	$2_{-1,2} - 1_{-1,1}$	5.56	2.01	3.63
	$2_{0,2} - 1_{0,1}$++	6.66	1.98	4.49
	$2_{0,2} - 1_{0,1}$	1.38	2.05	3.66
	$2_{1,1} - 1_{1,0}$	0.32	1.98	3.66

Table 5.4: CH_3OH Spectral Fits Continued

Region	Transition	Peak (K)	v_{LSR} (km s^{-1})	Line Width (km s^{-1})
B2c	$2_{-1,2} - 1_{-1,1}$	3.76	0.87	3.63
	$2_{0,2} - 1_{0,1}$++	4.79	0.87	3.78
	$2_{0,2} - 1_{0,1}$	0.71	0.74	3.75
	$2_{1,1} - 1_{1,0}$	0.15	0.74	3.59
B2d	$2_{-1,2} - 1_{-1,1}$	7.67	2.11	3.38
	$2_{0,2} - 1_{0,1}$++	9.21	2.08	3.87
	$2_{0,2} - 1_{0,1}$	2.24	2.14	3.04
	$2_{1,1} - 1_{1,0}$	0.63	2.14	2.91
mm	$2_{-1,2} - 1_{-1,1}$	0.22	3.10	2.88
	$2_{0,2} - 1_{0,1}$++	0.41	3.01	2.51
	$2_{0,2} - 1_{0,1}$	-	-	-
	$2_{1,1} - 1_{1,0}$	-	-	-

Table 5.5: HCN Spectral Fits

Region	Transition	Peak (K)	$v_{\rm LSR}$ (km s^{-1})	Line Width (km s^{-1})
B0a	$J = 1 - 0, F = 1 - 1$	4.19	0.81	3.50
	$J = 1 - 0, F = 2 - 1$	6.11	0.10	5.90
	$J = 1 - 0, F = 0 - 1$	3.05	0.85	8.00
B0b	$J = 1 - 0, F = 1 - 1$	1.30	1.29	2.10
	$J = 1 - 0, F = 2 - 1$	2.74	1.12	2.30
	$J = 1 - 0, F = 0 - 1$	0.54	4.90	2.80
B0c	$J = 1 - 0, F = 1 - 1$	2.42	0.68	3.50
	$J = 1 - 0, F = 2 - 1$	4.34	-0.47	5.70
	$J = 1 - 0, F = 0 - 1$	1.69	-0.27	7.50
B0d	$J = 1 - 0, F = 1 - 1$	1.74	0.71	3.70
	$J = 1 - 0, F = 2 - 1$	2.36	-0.20	5.50
	$J = 1 - 0, F = 0 - 1$	0.79	0.54	5.60
B0e	$J = 1 - 0, F = 1 - 1$	2.79	0.74	3.70
	$J = 1 - 0, F = 2 - 1$	4.04	0.17	6.50
	$J = 1 - 0, F = 0 - 1$	2.49	2.16	8.00
B0k	$J = 1 - 0, F = 1 - 1$	0.98	1.32	2.20
	$J = 1 - 0, F = 2 - 1$	1.62	1.25	2.20
	$J = 1 - 0, F = 0 - 1$	0.38	1.52	1.20
B0ℓ	$J = 1 - 0, F = 1 - 1$	1.64	1.22	2.10
	$J = 1 - 0, F = 2 - 1$	2.79	1.32	2.10
	$J = 1 - 0, F = 0 - 1$	0.46	1.45	1.30
B1a	$J = 1 - 0, F = 1 - 1$	6.02	0.81	3.40
	$J = 1 - 0, F = 2 - 1$	6.56	0.03	6.10
	$J = 1 - 0, F = 0 - 1$	3.14	0.41	7.80
B1b	$J = 1 - 0, F = 1 - 1$	3.56	0.71	3.40
	$J = 1 - 0, F = 2 - 1$	3.54	-0.41	5.90
	$J = 1 - 0, F = 0 - 1$	1.97	0.07	7.50
B2a	$4^{\rm th}$ component	5.25	4.50	1.60
	$J = 1 - 0, F = 1 - 1$	5.95	0.88	3.50
	$J = 1 - 0, F = 2 - 1$	6.32	0.17	5.70
	$J = 1 - 0, F = 0 - 1$	3.42	0.88	4.70
B2b	$4^{\rm th}$ component	3.57	4.43	1.80
	$J = 1 - 0, F = 1 - 1$	4.27	0.85	3.50
	$J = 1 - 0, F = 2 - 1$	4.49	0.54	5.50
	$J = 1 - 0, F = 0 - 1$	2.08	1.89	5.00
B2c	$J = 1 - 0, F = 1 - 1$	3.94	0.85	3.30
	$J = 1 - 0, F = 2 - 1$	5.61	0.47	4.00
	$J = 1 - 0, F = 0 - 1$	2.08	0.71	3.90
B2d	$4^{\rm th}$ component	3.53	4.23	1.70
	$J = 1 - 0, F = 1 - 1$	4.76	0.88	3.70
	$J = 1 - 0, F = 2 - 1$	5.48	0.30	5.00
	$J = 1 - 0, F = 0 - 1$	2.73	1.01	4.50
mm	$J = 1 - 0, F = 1 - 1$	1.17	2.44	1.52
	$J = 1 - 0, F = 2 - 1$	1.79	2.33	1.35
	$J = 1 - 0, F = 0 - 1$	0.72	2.54	1.25

Table 5.6: HNCO Spectral Fits

Region	Peak (K)	$v_{\rm LSR}$ (km s^{-1})	Line Width (km s^{-1})
B0a	0.13	-0.68	4.88
B0b	0.38	1.74	1.30
B0c	0.21	-0.75	4.47
B0d	0.29	0.03	4.30
B0e	0.10	0.58	4.91
B0k	0.22	1.60	1.94
B0ℓ	0.36	1.60	0.89
B1a	0.32	0.27	4.91
B1b	0.38	0.38	4.94
B2a	1.26	1.81	2.93
B2b	0.70	1.70	3.65
B2c	0.28	0.61	3.17
B2d	1.26	1.91	2.76
mm	-	-	-

CHAPTER 6

MODELING SHOCK CHEMISTRY IN ISOLATED MOLECULAR OUTFLOWS

Shocks are a crucial probe to understanding the ongoing chemistry within ices on interstellar dust grains, where many complex organic molecules (COMs) are believed to be formed. However, previous work has been limited to the initial liberation into the gas-phase through non-thermal desorption processes such as sputtering. Here, we present results from the adapted three-phase gas-grain chemical network code NAUTILUS, with the inclusion of additional high-temperature reactions, non-thermal desorption, collisional dust heating, and shock-physics parameters. Here, we are able to reproduce many of the predictions found through observations of the prototypical shocked-outflow L1157 by Burkhardt et al. (33). In addition, we find that, among others, NH_2CHO, $HCOOCH_3$, CH_3CHO have a significant post-shock chemistry formation routes, differing from many other COMs observed in shocks. Finally, a number of selected species and phenomena are studied here with respect to their usefulness as a shock tracer in various astrophysical sources.

6.1 Introduction

With the advent of modern observatories such as the Atacama Large Millimeter/ submillimeter Array (ALMA), there has been an explosion in high resolution and sensitivity observations of the star and planet-forming regions, with an emphasis on the role of chemical inventories on this evolution (13; 120). This is highlighted by a surge of interest in the interaction of gas and ice chemistry, including the condensation fronts (snow lines) within protoplanetary disks (22; 183; 232) and the thermal warm-ups in hot cores and corinos (13; 120). In particular, it is believed many complex organic molecules (COMs) are efficiently formed primarily in interstellar ices (77; 104). However, because these frozen molecules cannot be observed through radio rotational spectroscopy, our knowledge of interstellar ice chemistry remains highly unconstrained. Due to these difficulties to deduce the molecular composition of ices directly means that we must rely on, to date, incomplete astrochemical models to make inferences. Refinement of these models is therefore critical to unlock the potential of modern astrochemistry observations. One way this can be accomplished is to indirectly observe ice abundances in regions where the ice is actively being liberated and compare the models using those observations. In these types of sources, it is crucial that additional chemical processing does not dominate the desorption process.

Low-velocity shocks, which liberate molecules off of the ice and into the gas phase without destroying most molecular bonds (e.g. sputtering), provide this indirect probe (192). Because shocks are ubiquitous, but transient, features throughout the interstellar medium, it is crucial to understand the physico-chemical evolution of these phenomena.

One of the most promising locations to study shocks is the low-mass protostellar outflow L1157, an isolated, nearby (∼250 pc (142)) bipolar outflow where the ejection events have shocked the pristine, chemically-rich ice in the surrounding dark cloud (7; 16; 33; 138). Here, we can study the effects that shocks have on a material in relative isolation of other competing processing (e.g. thermal processing common in hot cores). Prior observations by Burkhardt et al. (33) have shown that the chemical inventory affected by the shock could be divided into three classes: those directly sputtered from grains (e.g. CH_3OH), those already in the gas but enhanced by the shock (e.g. HCO^+), and those that were sputtered and subsequently enhanced by gas-phase chemistry (e.g. HNCO). To date, only a small number of these species and a few more complex molecules have been targeted by interferometric observations (see, e.g., (16; 49; 133)). However, single-dish surveys have revealed that this molecular outflow is extremely chemically rich, with the detection of many highly complex molecules including NH_2CHO, CH_3CHO, CH_3OCH_3, $HCOOCH_3$, C_2H_5OH, and CH_3CN (7; 138).

6.2 Model

In order to study the competitive effects sputtering and post-shock chemistry in these types of sources, we adapted the three-phase gas-grain chemical network code NAUTILUS (199). This model calculates the molecular abundances as a function of time through a rate-equation approach. The measured and computed kinetic rate coefficients for the chemical reactions and the use of the OSU-KIDA network (230), with additional reactions added in, as discussed in Section 6.2.3. The physical parameters of the model were computed to accurately simulate the conditions within astrophysical C-shocks, as discussion in Section 6.2.1

6.2.1 Structure of Model

As described in Figure 6.1, the model was run for 10^6 years in the conditions mostly consistent with what is used to model dark cloud chemistry, such as TMC-1 (106; 141; 161; mcg). Specifically, the constant physical conditions in time scale are:

$$T_{\mathrm{gas},0} = T_{\mathrm{dust},0} = 10\ \mathrm{K} \tag{6.1}$$

$$n_{\mathrm{H_2},0} = 5 \times 10^4\ \mathrm{cm}^{-3} \tag{6.2}$$

$$A_{V,0} = 10 \tag{6.3}$$

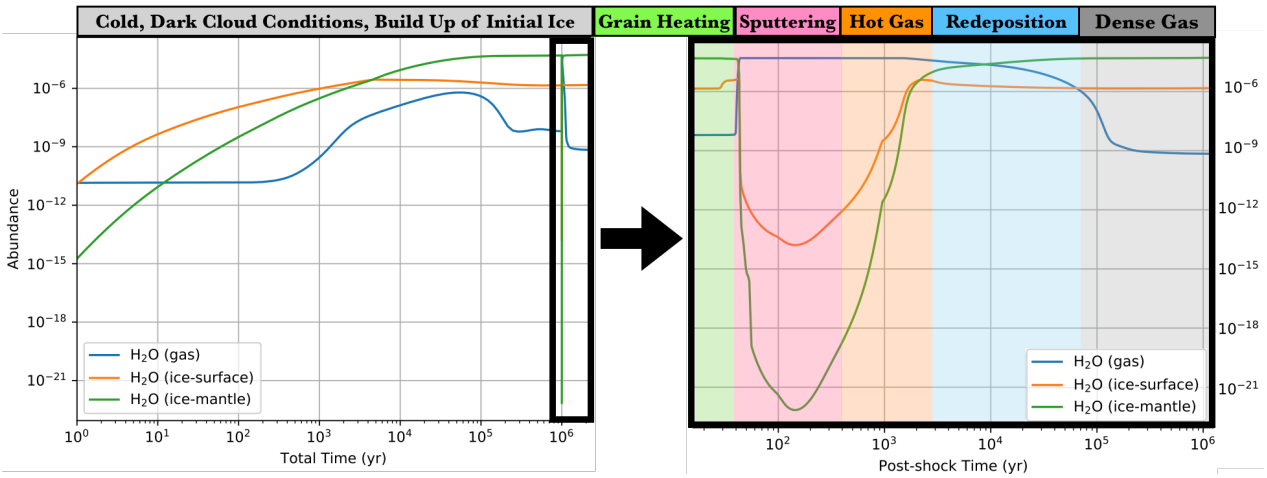

Figure 6.1: *Left* The temporal three-phase abundances of H_2O relative to hydrogen with respect to total time within the model. *Right* The temporal three-phase abundances of H_2O relative to hydrogen with respect to the time following the shock. Here, t=0 corresponds to 10^6 years after the start of the left figure, with a rescaling of the logarithm in the abscissa, zooming in on the shock event. On the top, the general time regimes of differing physical processing are labeled and colored.

Through this, the model is able to build up a sufficiently-thick ice mantle that is representative of a cold core prior to a shock event and the majority of the gas and solid-phase abundances have relatively stable value. Due to the difficulties of astronomical observations of interstellar ices, these values are highly unconstrained and limited to only the most abundant species with identified infrared absorption features (27). As such, the subsequent analysis of abundances following the liberation from the ice will be biased by this. If one assumes that the vast majority of the solid-phase abundance is lifted into the gas-phase and that the abundances of these species experience little gas-phase modification during the shock, then the initial ice abundance will be a 1:1 tracer of the post-shock gas-phase abundance enhancement. However, it is likely that many species will additionally undergo some form of chemistry during or after the shock, constraining the effects of this competing processes will allow us to disentangle the source of molecular enhancements or diminishment. Due to the uncertainties mentioned above in the ice chemistry, though, we will generally focus on the overall temporal evolution of the abundances and the regimes in which significant enhancements occur.

Following the initial build up of ice for 10^6 years, we introduce a shock event into the model, as described in Section 6.2.2. Here, in lieu of direct abundance comparisons, we focus on the general enhancements of the species from the pre-shock abundances to the post-shock abundances. Because the sputtering occurs much faster than the post-shock chemistry, it is possible for some species to easily differentiate which process significantly dominates the enhancements. The evolution of the shock event takes roughly 10^5 years, depending on the velocity of the shock and initial conditions of the cloud.

After material cools back down to the dark cloud conditions, we then continue to run the model until approximately 10^6 years after the shock event. This facilitates the study of the after-effects on the chemistry, long after the shock has passed. Any significant trends seen here may point to important signatures that would indicate if the material was recently shocked, compared to what was seen in the preshock conditions. This will be discussed in detail in Section 6.3.

6.2.2 Adaptation of NAUTILUS for Shock-Chemistry

To accurately simulate the chemistry within shocked media, the NAUTILUS code needed to have a number of additional processes and reactions. This includes the inclusion of additional high-temperature reactions from Harada et al. (95) and Garrod (77), the physical structure and sputtering processes as described by Jiménez-Serra et al. (117), and the evolution of the dust temperature as described by Miura et al. (168), of which will all be described in detail in the subsequent sections. Due to the high degree of chemical complexity in our network, including a robust ice network, our network is able to simulate the chemistry of much larger COMs than previous models (46; 66; 139).

Physical Structure within C-Shocks

As extensively studied previously, the physical conditions within shocks and turbulent sources are found to have a significant impact on the subsequent chemistry (33; 46; 92; 138). While several studies looked into these effects by coupling a chemical network to magnetohydronamics simulations (108), the chemical networks used were often limited in scope in order to maintain a reasonable computation time. Because, here, we wish to leverage the full gas-grain chemical network of OSU.KIDA within NAUTILUS, the physical conditions will be simplified to a single, 1-D slab. To do this, we adopted a system of parametric equations developed by Jiménez-Serra et al. (117) that have been fit to match the simulated physical conditions by the MHD shock-structure calculated by Flower and Pineau des Forêts (70); Kaufman and Neufeld (126). By using these parametric equations, we are able to accurately reproduce these physical conditions while at the same time treating the chemistry in more detail than in previous studies.

Here, we consider a plane-parallel C-shock where accelerated material interacts with a cold, quiescent cloud. Because these equations were fit to data from the numerical simulations, the dependent variable is the spatial location within a snapshot of the shock, z. Since the pre-shocked material is assumed to be homogeneous, these physical locations can be translated to corresponding times it would take to propagate through the shock to achieve the spatial coordinate given by assuming a single velocity to describe the aggregate speed of shock (i.e. the shock velocity, v_s). It should be noted that the time described here refers to the post-shock time (i.e. beginning on Figure 6.1 *Right*). Across this shock, the magnetic fields within the source will accelerate the charged particles. Because the dust grains tend to be charged in these sources, this causes the predominantly neutral gas to temporarily decouple from the dust within the shock. These velocities of the gas and grains can be

described in the frame of reference of the downstream material as

$$v_{\text{gas/grains}} = (v_s - v_0)\left(1 - \frac{1}{\cosh\left[(z - z_0)/z_{\text{gas/grains}}\right]}\right) \tag{6.4}$$

where v_0 is the post-shock velocity of both the gas and dust in the co-moving shock frame of reference (i.e. the difference between the peak drift velocity and the overall shock velocity), v_s is the shock velocity, z_0 is the distance where the decoupling begins, and the relative values of z_{gas} and z_{grains} describe the degree to which the velocities will decouple. The relative velocities between these two populations, referred to the drift velocity, is then simply

$$v_d \equiv |v_{\text{gas}} - v_{\text{grains}}|. \tag{6.5}$$

With these velocities, we can covert to the flow of time a gas particle experiences as the shock propagates through it as

$$t_{\text{postshock}} = \int \frac{1}{v_s - v_{\text{gas}}}\,\mathrm{d}z \tag{6.6}$$

From the subsequent time-dependent velocity profile and an initial gas density, n_0, initial gas temperature, $T_{\text{gas},0}$, we can develop the temporal evolution of the density and gas temperature. By assuming a conservation of mass between the preshock conditions and at any given time step (i.e. the shock jump condition for mass), one can describe the density as a function of the velocity (and thus time) such that

$$n_{\text{gas}}(t_{\text{postshock}}) = \frac{v_s}{v_s - v_{\text{gas}}} n_0. \tag{6.7}$$

Since the extinction, A_V, can be estimated to be proportional to the gas density (19), it can be similarly scaled from an initial extinction value $A_{V,0}$.

For the purposes of matching the MHD simulations, the gas temperature is described as a "Planck-like" function such that

$$T_{\text{gas}} = T_{\text{gas},0} + \frac{a_T (z - z_0)^{b_T}}{e^{(z - z_0)/z_T} - 1} \tag{6.8}$$

where a_T and z_T are fitting parameters to the location and value of the peak gas temperature and b_T is an integer fitting the temperature's sensitivity to shock location.

For the purposes of this paper, we seek to model the prototypical shocked-outflow L1157. Therefore, while this model is capable of simulating a range of shock velocities and gas densities, we will focus on a detailed analysis of the physical conditions based on derived values from Burkhardt et al. (33). And so, we assume a v_s of 20 km s^{-1} and n_0 of $5{\times}10^4$ cm^{-3}. Assuming standard dark cloud conditions in the preshock gas, our initial gas and dust temperatures were both 10 K (107). From Table 4 from Jiménez-Serra et al. (117), these initial conditions correspond to fitted values of $z_{\text{gas}} = 1.4{\times}10^{16}$ cm, $z_{\text{grains}} = 3.2{\times}10^{15}$ cm, $z_{\text{T}} = 5.0{\times}10^{15}$ cm, and $a_{\text{T}} = 2.9{\times}10^{16}$ cm, assuming z_0 =0 cm.

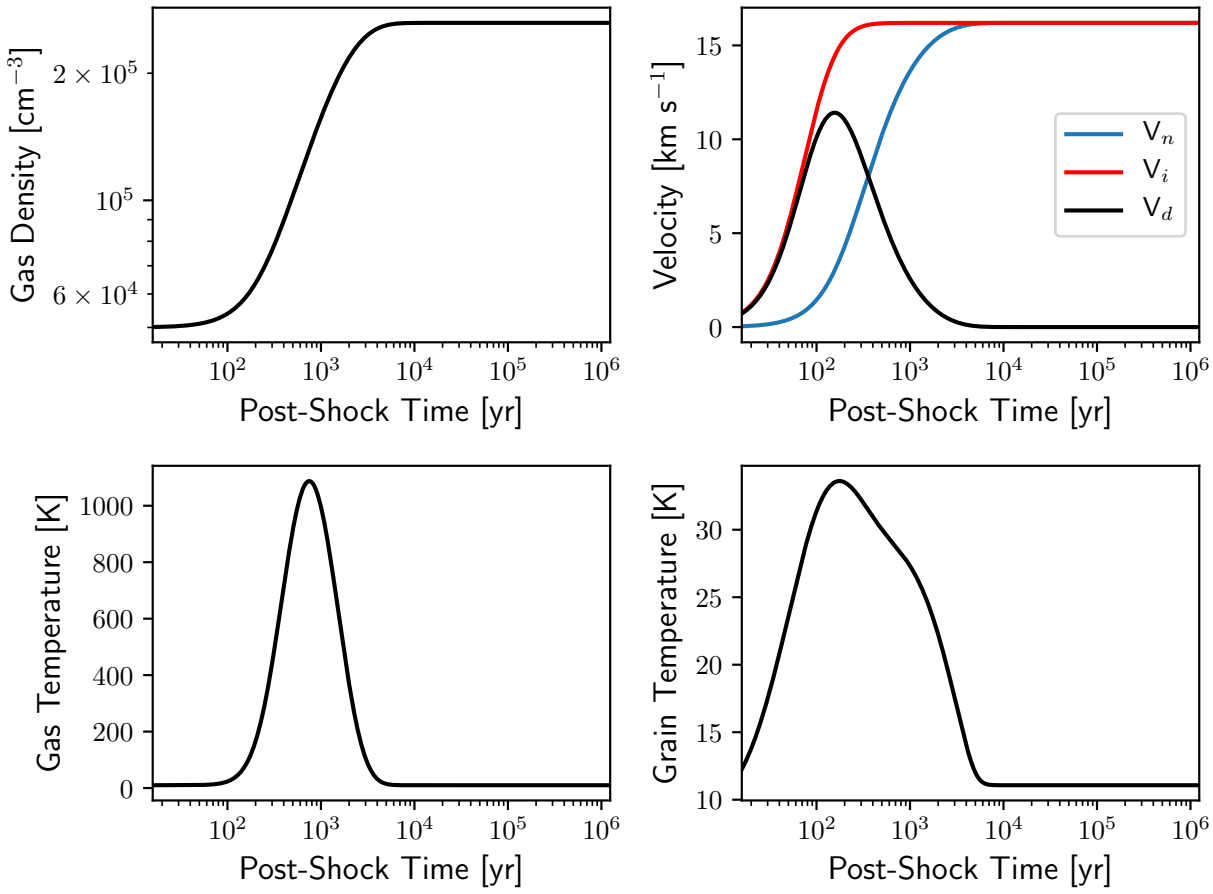

Figure 6.2: Physical evolution within the shock (i.e. $t_{\text{postshock}}$=0 years corresponds to total time in model of t_{total}=10^6 years) for the gas density, transverse velocities, gas temperature, and grain temperature, as described in Section 6.2.2.

Using this formalism, the physical conditions within the shock modeled here can be seen in Figure 6.2. It should be noted that there is a distinct delay in the heating of the gas temperature relative to the peak drift velocity and dust temperature (whose calculation will be described in Section 6.2.2) by roughly an order of magnitude in time. The impacts of this will be discussed in Section 6.3.

Dynamic Dust Heating

In order to accurately asses the significance of enhancement through desorption versus chemical processing in shocks, it is crucial to consider the effects of the dust temperature has on the system. Therefore, we adopted the formalism from Miura et al. (168), which is based on Aota et al. (5). Here, they consider the effects from the adiabatic heating of high-velocity particle collisions and the conductive heating from the dust residing in hot

gas.

To start, we adopt the formalism used for gas-grain energy transfer in the free flow approximation (128; 182). Here, they describe the evolution of the dust temperature as a balance between the radiative cooling, collisional heating, and radiative heating.

The temperature of the dust, T_{dust}, can be thus described as

$$\frac{4}{3}\pi a_{\text{dust}}^2 \rho_{\text{mat}} \frac{\mathrm{d}T_{\text{dust}}}{\mathrm{d}t} = 4\pi a_{\text{dust}}^2 \left(\Gamma - \epsilon_{\text{em}} \sigma_{\text{SB}} T_{\text{dust}}^4\right) \tag{6.9}$$

where a_{dust} is the average dust radius, ρ_{mat} is the mass density within a dust grain, c_{dust} is the specific heat of the dust, ϵ_{em} is the emission coefficient for the dust given as

$$\epsilon_{em} = A a_{\text{dust}} T_{\text{dust}}^2, \tag{6.10}$$

(where A is the dust emissivity given by Draine and Lee (62) as A=0.122 cm^{-1} K^{-2}), σ_{SB} is the Stefan-Boltzmann constant, and Γ is the function describing the rate that energy is transfered from the gas to the dust per unit area (i.e. energy flux between gas and dust). Here, Γ is given by

$$\Gamma = \rho_{\text{gas}} v_{\text{drift}} \left(T_{\text{recovery}} - T_{\text{dust}}\right) C_{\text{H}} \tag{6.11}$$

where T_{recovery} is the recovery temperature, or adiabatic equilibrium temperature, defined in Kitamura (128); Probstein and Shorenstein (182) as

$$T_{\text{recovery}} = \frac{2}{\gamma+1}\left(\gamma + (\gamma-1)s_a^2 - \frac{\gamma-1}{1+2s_a^2 + \frac{s_a}{\sqrt{\pi}e^{s_a^2}\text{erf}(s_a)}}\right) \tag{6.12}$$

and C_{H} is the heat transfer function defined as

$$C_{\text{H}} = \frac{\gamma+1}{\gamma-1}\frac{k_{\text{B}}}{8\mu m_{\text{H}} s_a^2}\left[\frac{s_a}{\sqrt{\pi}e^{s_a^2}} + \left(\frac{1}{2}+s_a^2\right)\text{erf}(s_a)\right]. \tag{6.13}$$

In these equations, γ is the specific heat-ratio, k_{B} is the Boltzmann constant, μ is the mean molecular weight of a gas particle, m_{H} is the mass of a hydrogen atom, and s_a is a ratio of the drift velocity and the thermal gas velocity defined as

$$s_a = \frac{v_d}{\sqrt{2k_{\text{B}}T_{\text{gas}}/\mu m_H}}. \tag{6.14}$$

Equation 6.9 can be solved for the dust temperature by which the heating of the dust by the gas is in equilibrium with the radiative cooling,

$$\Gamma - 4\epsilon_{\text{em}}\sigma_{\text{SB}}T_{\text{dust}}^4 = 0. \tag{6.15}$$

This equation can be further rewritten as

$$C_1 v_d^3 \alpha_1(s_a)\alpha_2(s_a) - C_2 T_{\text{dust}} v_d \alpha_2(s_a) - C_3 T_{\text{dust}}^6 = 0 \tag{6.16}$$

$$T_{\text{dust}}^6 + \frac{C_2}{C_3} v_d \alpha_2 T_{\text{dust}} - \frac{C_1}{C_3} v_d^3 \alpha_1 \alpha_2 = 0 \tag{6.17}$$

where C values are constants with respect to s_a defined as

$$C_1 = \frac{1}{8}\rho_{\text{gas,0}} \tag{6.18}$$

$$C_2 = \frac{1}{8}\frac{\gamma+1}{\gamma-1}\frac{k_{\text{B}}}{\mu m_{\text{H}}}\rho_{\text{gas,0}} \tag{6.19}$$

$$C_3 = A\sigma_{\text{SB}}a_{\text{dust}} \tag{6.20}$$

and α values are functions of s_a defined as

$$\alpha_1(s_a) = 1 + \frac{\gamma}{\gamma-1}s_a^{-2} - \frac{1}{1+2s_a^{-2}+2\frac{s_a}{\sqrt{\pi}e^{s_a^2}\text{erf}(s_a)}} \tag{6.21}$$

$$\alpha_2(s_a) = \left(1+\frac{1}{2s_a^2}\right)\text{erf}(s_a) + \frac{1}{\sqrt{\pi}s_a e^{s_a^2}} \tag{6.22}$$

With this reduction of the equation, Equation 6.17 is solved for T_{dust} using the MINPACK's HYBRD and HYBRJ routines with the modified Powell method. For the purposes of guiding the algorithm, initial guesses were computed by

$$T_{\text{dust,guess}} = T_{\text{dust,0}} + \frac{v_d}{v_s}\left(10\text{ K}\right). \tag{6.23}$$

Applying the temporal evolution of the gas temperature, density, and drift velocity determined in the previous section, we are able to compute the dust temperature across the evolution of the shock. In the pre-shock gas, the gas and dust are assumed to be in thermal equilibrium, or $T_{\text{dust}} = T_{\text{gas}}$.

In addition, we deviate from the formalism used in Jiménez-Serra et al. (117), by setting an additional constraint of the velocity when used to calculate the rate of dust heating. Specifically, we assume that as the gas and grains begin to recouple, the drift velocity will eventually fall below the random thermal velocities of the gas. In the hot-gas regime, this thermal velocity may be non trivial. As such, the velocity of collisions may be more accurately described for these purposes as:

$$v = \max\left[v_d, \sqrt{\frac{2k_B T_{\text{gas}}}{\mu m_{\text{H}}}}\right], \tag{6.24}$$

As can be seen in Figure 6.2, the dust temperature is found to initially track with the velocity structure within the shock, peaking at the same corresponding time as the peak velocity due to adiabatic heating. However, as the gas continues to heat up after this, the dust temperature undergoes a secondary heating regime due to the conductive heating from the hot gas. As such, while the sputtering rate will fall off rather rapidly, the ability for species to redeposit onto the grains is delayed until the gas can cool sufficiently.

Sputtering

One major physical process that is common in astrophysical shocks is the non-thermal desorption of molecules from the ice into the gas-phase through the collision of moderately-fast gas-phase particles with the dust grains (e.g. sputtering). Here, this process is a key mechanism for lifting complex molecules into the gas phase non-destructively. For typical C-shocks velocities (e.g. 10-40 km s^{-1}), the sputtering is significant enough to desorb most species from the ice mantle without destroying them or having significant grain core erosion, both of which are common in high-velocity J-shocks (192).

In order to include these processes, the sputtering yields must be computed for each species on the ice, which is dependent on the conditions of the shock, the nature of the incident particle, and the binding properties of the target molecule. Utilizing the procedure discussed in Caselli et al. (36) and Jiménez-Serra et al. (117), with the initial formalism introduced in Draine and Salpeter (64), we can compute the rate in which some ice species, J, is sputtered off the surface by some incident particle, P, such that

$$\left[\frac{\mathrm{d}n_{\mathrm{J}}}{\mathrm{d}t}\right] = \frac{\pi a_{\mathrm{dust}}^2 n_P}{2s_P}\sqrt{\frac{8k_B T_{\mathrm{gas}}}{\pi m_P}}\int_{x_{\mathrm{th}}}^{\infty} x^2\left(e^{-(x-s_P)^2} - e^{-(x+s_P)^2}\right)\langle Y(E_P)\rangle\ \mathrm{d}x \tag{6.25}$$

where a_{dust} is the average dust grain radius, n_P is the gas-phase density of the projectile, k_B is the Boltzmann-constant, T_{gas} is the gas temperature, m_P is the mass of the projectile. s_P is the ratio between the kinetic energy of a particle traveling at the current drift velocity and the thermal energy of the gas, or

$$s_P^2 \equiv \frac{m_P v_d^2}{2k_B T_{\mathrm{gas}}}. \tag{6.26}$$

Similarly, x is the ratio between the kinetic energy of a projectile at some specific velocity, v_x, and the thermal energy of the gas. This is related to the impact energy of the project, E_P as

$$E_P = x^2 k_B T_{\mathrm{gas}}. \tag{6.27}$$

The integral, therefore, is equivalent to the total contribution from projectiles at all velocities corresponding to an x value higher than x_{th}, which is defined as

$$x_{\mathrm{th}} = \sqrt{\frac{\epsilon_0 U_0}{\eta k_B T_{\mathrm{gas}}}} \tag{6.28}$$

where U_0 is the binding energy of the species to be sputtered off and ϵ_0 is defined as

$$\epsilon_0 = \max[1, 4\eta]. \tag{6.29}$$

Here, η is a ratio describing the relative masses of the projectile (m_P) and the target species (m_T)

$$\eta = 4\xi\frac{m_P m_T}{(m_P + m_T)^{-2}} \tag{6.30}$$

where ξ is a material-specific efficiency factored assumed to be 0.8 for ices (64). The angle-averaged value for the sputtering yield, Y, which is approximately equal to double the perpendicular yield value, is described in Draine and Salpeter (64) such that

$$\langle Y \rangle_\theta \approx 2Y(\theta = 0) = A \frac{(\epsilon - \epsilon_0)^2}{1 + \left(\frac{\epsilon}{30}\right)^{4/3}} \text{ for } \epsilon > \epsilon_0 \tag{6.31}$$

where A ≈8.3×10^{-4} and ϵ is defined as

$$\epsilon = \frac{E_P}{U_0}\eta \tag{6.32}$$

For the purposes of calculating these sputtering yields, the binding energies, U_0, need to be known for each species, which are already given within NAUTILUS as part of the OSU.KIDA network. It should be noted that value for many of these species are theoretically estimated and have not been explicitly experimentally measured.

For each grain species in the network, a sputtering reaction was added for the following gas-phase projectiles: H_2, He, C, O, Si, Fe, and CO. To compute n_P, the gas-phase abundance within the model at that time step for each projectile was multiplied by the overall gas density (i.e. n_{H_2}). In the NAUTILUS three-phase model, sputtering can only occur for species on the surface of the ice (i.e. the top few monolayers), similar to the vast majority of other desorption mechanisms (199). The integral over x was computed with the DQAGS routine in the QUADPACK package. It should be noted that computing this indefinite integral numerically was found to be highly sensitive to the sampling rate of the integrating routine, as much of the range in which the integral is evaluated over is trivially small. As such, to increase the efficiency of the computation of the integral, we converted the integral to be definite by approximating the upper and lower bounds such that:

- If $x_{\text{th}} > s_P + 20$, then the vast majority of the projectiles at this drift velocity are traveling at too low of a velocity to be an effective sputterer. In this case, we assume the integral will evaluate to zero.
- If $x_{\text{th}} < s_P - 10$, then the vast majority of the projectiles at this drift velocity are potentially good projectiles for efficient sputtering. In this case, we reset the lower bound of the integral to $s_P - 10$ and the upper bound to $s_P + 20$.
- Otherwise, x_{th} is reasonably close to s_P and will not cause any significant issues integrating as a lower bound. In this case, we only reset the upper bound to $s_P + 20$ for computational efficiency instead of evaluating an indefinite integral.

6.2.3 High Temperature Chemical Network

One major motivation for the use of the latest version of the OSU.KIDA network is the inclusion of the high-temperature reactions developed by Harada et al. (95), as the gas-phase temperatures in the post-shock regimes can reach 1000 K at even v_s ∼20 km s^{-1}.

Table 6.1: Reactions added to network from Tsang (223); Tsang and Herron (224).

Reactions	α [$cm^3\ s^{-1}$]	β	γ [K]	Temperature Range [K]
H_2+OCN→HNCO+H	6.54×10^{-14}	2.58	2720	300-3300
H_2O+OCN→HNCO+OH	9.13×10^{-14}	2.17	3050	500-2500
HCN+OH→HNCO+H	4.18×10^{-18}	4.17	-247.8	298-2840
HCN+OH→HOCN+H	6.11×10^{-14}	2.45	6100	298-2840
OH+OCN→HNCO+O	5.38×10^{-14}	2.27	496.7	500-2500

Since many gas-grain chemical networks are optimized to reproduce the chemistry of dark clouds (106; 141; 161; 205; mcg) and hot cores(77; 107), this high temperature regime remains less robustly studied and warrants further study. By considering both the dark cloud and high-temperature regimes in the same model, we can evaluate how effective the network is to a large dynamic range of conditions.

In addition, we also added several gas and grain reactions for species related to the common observational shock-tracer, HNCO. The HNCO-isomers and related ions developed by Quan et al. (184) were included in order to fully account for the potential multiple formation routes, especially in colder conditions. Moreover, in order to test the effectiveness of unique chemistry occur in the high-temperature regime, we added several reactions, listed in Table 6.1, with significant barriers and a strong temperature dependence taken from previous combustion chemistry studies (223; 224).

6.3 Results

6.3.1 Overview of shock-chemistry regimes

From the physical structure described in Section 6.2.2.1, six major regimes of chemistry in the shock can be seen in the molecular abundances within the model. First, the pre-shock chemistry locks in the initial gas and ice abundances after the first 10^6 years, representing how the chemistry would proceed in the region in the absence of a shock. Second, the drift velocity begins to rise. Before the sputtering becomes highly efficient in sublimating the ice mantle, the lower-velocity projectile particles are only capable of heating the dust. As such, the mobility of species in the ice rapidly increases, promoting the rapid formation of complex chemistry on the ice for ∼50 years, after which the peak amount of sputtering, which occurs up until about 100 years after the shock, lifts essentially the ice-residing molecules into the gas phase. Following this, the gas, which is heated slower than the dust, reaches a peak temperature of ∼1000 K around 10^3 years after the onset of the shock. At the same time, the dust heating becomes dominated by conductive heating over adiabatic heating as the drift velocity decreases. At this point, the hot gas-phase chemistry becomes much more significant. We here refer to the regime as "post-shock chemistry."

After the environment cools back down to dark cloud temperatures, fully returning around 10^4 post-shock years, the species in the gas phase redeposit back onto the grain and reform the ice. Hypothetically, then the structure and composition of ice in the post-shock

regime might be distinct from ice formed under quiescent cold-core conditions. Thus, it is possible that there will be permanent relics of a shock occurring in ice. This newly enriched ice also may result in a increased rate of reactive desorption, or where a reaction on the ice surface is energetic enough to lift the products into the gas-phase. This will be discussed in detail in Section 6.4.2. Following this, we continue to run the model until 10^6 years where any physical, non-chemical relics of the shock should be no longer relevant.

6.3.2 Bulk motion of the ice

To follow the overall motion of the ice, it is useful to look at one of its primary constituents of the ice: H_2O. As seen in the left plot in Figure 6.1, the first 10^6 years actively builds up a thick ice (typically $\sim$70 monolayers) in the dark cloud conditions prior to the shock. The second 10^6 years (i.e. right plot) in Figure 6.1 is entirely where the shock occurs. Due to difficulties in viewing data in log-space, we will henceforth exclusively display the abundance evolution from the post-shock time and not the initial time of the model. For the purposes of viewing the results of the pre-shock chemistry, we will only consider the abundance at $t_{\text{postshock}} = 0$ or t_{total}=10^6 years. In general, most species tend to reach steady state abundances during the initial cold core phase.

Initially, as the drift velocity increases, increased mobility on the heated dust can induce temporary enhancements in the ice abundance for certain species. In the peak sputtering regime, the ice-surface and ice-mantle abundances are seen to drop to trivial levels, with a slight enhancement of the gas-phase abundance of CO. Once the drift velocity decreases to levels that make sputtering inefficient, the ice abundances stop decreasing. However, because the dust is conductively heated by the hot gas in this later regime, the recently sputtered species are unable to redeposit back onto the surface of the ice and must undergo additional post-shock gas-phase chemistry if efficient routes exist. While this regime does not appear to impact the abundance of gas-phase H_2O in Figure 6.1, specifically, the regime is still relevant for the motion of the ice and to less abundant, and generally more complex, molecules.

Following the redeposition, the higher post-shock density slightly enhances the abundance of some species, but overall should return to initial physical conditions. As will be discussed, some species undergo an enhancement of ice abundances long after the shock passes, despite a gas-phase abundance that is consistent with the pre-shock values. For other species, the ice abundance, with no significant formation routes in dark clouds, will drop down to pre-shock conditions, but only on the timescales of 10^6 years after the shock event.

6.3.3 Classification of Species

In this work, we will focus on a collection of molecules that have are either classic shock-tracing molecules, key probes of a certain physical process, or molecules that have been detected in L1157 or other similar molecular outflows (33; 46; 138). While over 500 species

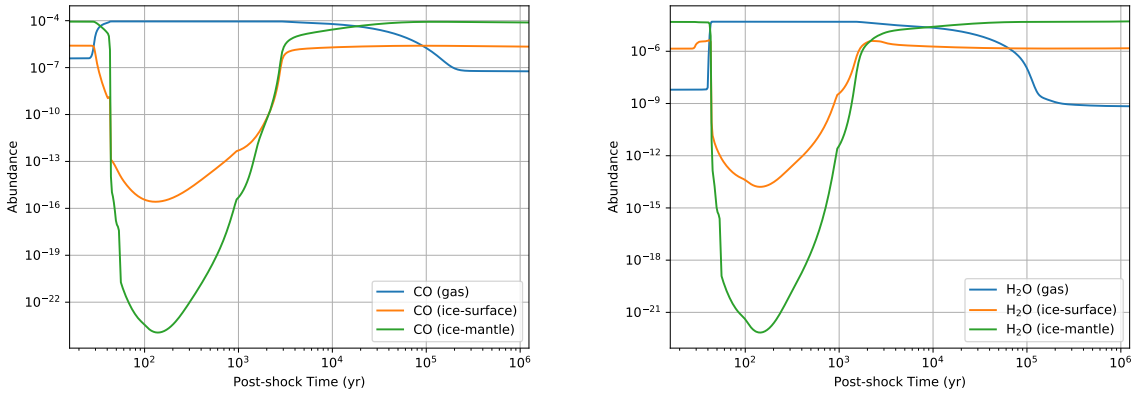

(a) CO (b) H_2O

Figure 6.3: Simulated three-phase abundances of studied species over the time period in which the shock passes through in the model (i.e. $t_{\text{postshock}}$=0 corresponds to t_{total}=10^6 years) for species with little post-shock chemistry and whose abundance traces the bulk motion of the ice.

are simulated in the model, this collection will provide sufficient range of formation routes to effectively probe the chemistry within the shocks. The three-phase abundances of each of these species over time are shown in Figures 6.3-6.11, which have been grouped with a species of similar chemistry, as discussed at the end of this section. Here, we will discuss each regime in detail, discussing collections of molecules that have related profiles and dominate reaction types.

Pre-Sputtering Peak Dust Warm Up ($\lesssim 50$ years)

For the first $\sim$100 years following the shock, the collisions between the gas and grains begin to increase in frequency and impact energy, but the drift velocity has yet to reach its peak value. While the velocities are too low to induce sputtering, it is sufficient to begin heating the dust grain ($\Delta T_{\text{dust}} \lesssim 15$ K). This can have a number of effects, the foremost being the increased mobility of species to diffuse within the ice. Similar to what is seen in chemical models of hot cores, this warmup phase can, in turn, rapidly accelerate the formation of complex molecules. This phase is, however, much shorter than the normal timescales for thermal desorption (77), which is found to be mostly inefficient in this regime. In this regime, we classify species into one of three types:

1. Those for which gas and ice abundance profiles are constant over time, implying that the dominant ice and gas-phase reactions were already efficient prior to this increase in dust temperature. These species tend to be relatively simple (e.g. CO, H_2O, NH_3, CH_3OH), and thus would have relatively low binding energies and could already easily diffuse.

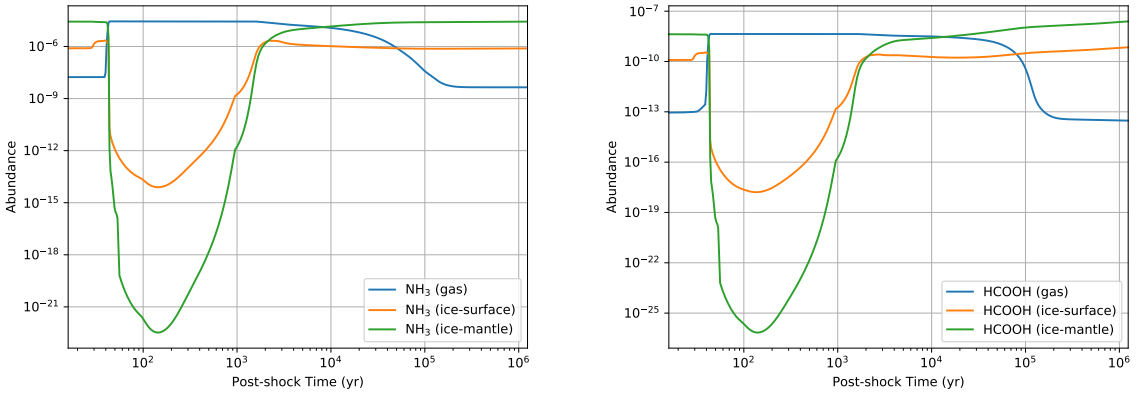

(a) NH_3 (b) HCN

Figure 6.4: Simulated three-phase abundances of studied species over the time period in which the shock passes through in the model (i.e. $t_{\text{postshock}}$=0 corresponds to t_{total}=10^6 years) for species with little post-shock chemistry and whose abundance traces the bulk motion of the ice.

2. Those for which ice abundance rapidly increases in this short time period and the gas-phase abundance becomes enhanced due to non-thermal desorption from exothermic reactions (76). These species (e.g. CH_3CHO, OCN, CN, SO_2) tend to have fairly low ice-abundances compared to what might be expected through observational constraints, which is likely due to the fact that these species were unable to efficiently diffuse in the dark cloud conditions. The primary formation routes for the molecules were most efficient in the gas-phase, and thus were far too abundant for the ice enhancements to alter it significantly. For some species, like OH, the molecule is enhanced on the ice through the dissociation of species, such as HOCO, which also forms CO that reacts with N to form OCN. In the event that the ice-chemistry for these species are found to be more efficient (e.g. comparable or more efficient than the gas-phase chemistry), then it possible that these reactions may induce additional gas-phase enhancements in the peak-sputtering regime.

3. Finally, some species also appear to have an enhancement in the ice due to the heating of the dust. However, it only starts occurring once the sputtering is also efficient. This behavior manifests a small increase in the ice-surface abundance prior to the rapid depletion in the next regime. These species tend to be the more complex species in the network, such as $HCOOCH_3$, NH_2CHO, and HCOOH, since these require additionally high dust temperatures to effectively diffuse, or were enhanced by the initial production of the ice-species in the previous group.

While a large number of species here display some sort of ice enhancement in this short time period, the enhancements only significantly impact any subsequent ice-chemistry

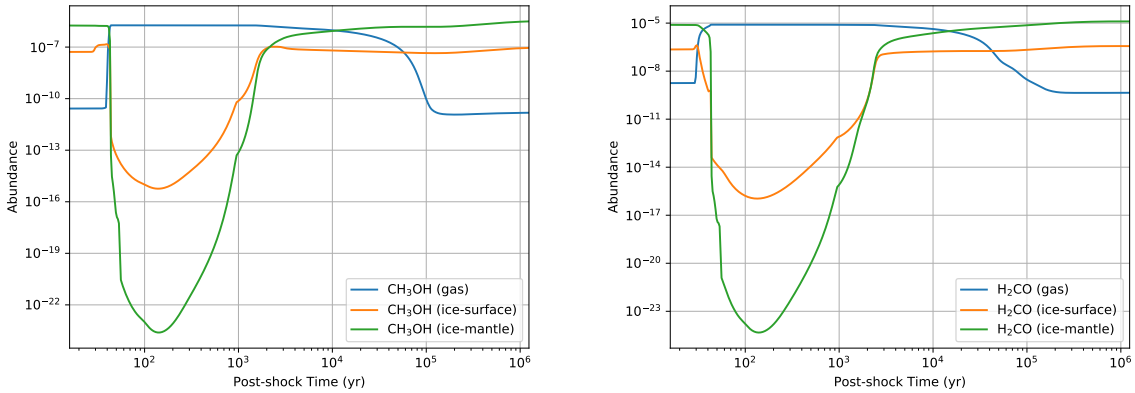

(a) CH_3OH (b) H_2CO

Figure 6.5: Simulated three-phase abundances of studied species over the time period in which the shock passes through in the model (i.e. $t_{\text{postshock}}$=0 corresponds to t_{total}=10^6 years) for species with little post-shock chemistry and whose abundance traces the bulk motion of the ice.

for a select number of species which are primarily dominated by gas-phase chemistry. This implies that in the astrophysical shocks, the secondary chemical effects prior to the peak sputtering are relatively minimal. And to this extent, low-velocity shocks can act as a useful tool into constraining the underlying ice-chemistry without having to consider additional physical processes.

Peak-sputtering (∼50-200 years)

Here, the drift velocity, and thus the sputtering rate reaches its peak value. At this point, the species in the ice surface and mantle are rapidly lifted into the gas phase, leaving only negligible abundances on the grain (i.e. less than 1 monolayer). Indeed, this process is seen to be much more efficient that both thermal and reactive desorption within shocks. Again, here, we describe the major groups of species in this regime:

1. For highly abundant gas-phase species, such as OH, CS, and CN, the ice abundance was only a small fraction of the total reservoir of those molecules due to gas-phase formation routes being much more efficient. As such, the liberation of the ice population did not appreciably enhance the gas-phase abundance of these molecules.

2. For other species, the new gas-phase abundances are nearly equivalent to the pre-shock ice abundance with a near-instantaneous transition. While some of these species may have initially formed in the gas-phase and froze out, the primary reservoir of these species, such as H_2O, NH_3, and HCOOH, prior to the shock was in these ices. So, the enhancements in the gas-phase abundances are exclusively due to sputter-

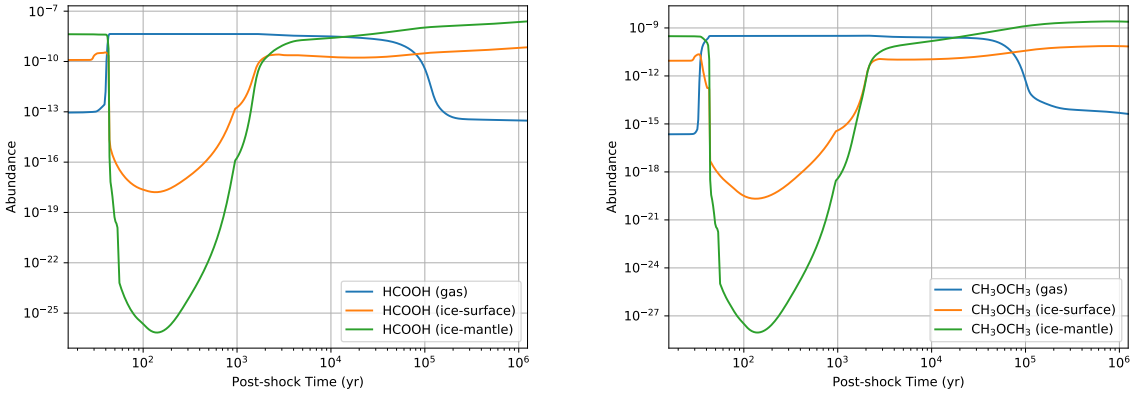

(a) HCOOH (b) CH_3OCH_3

Figure 6.5: Simulated three-phase abundances of studied species over the time period in which the shock passes through in the model (i.e. $t_{\text{postshock}}$=0 corresponds to t_{total}=10^6 years) for species with little post-shock chemistry and whose abundance traces the bulk motion of the ice.

ing and not post-shock chemistry. Thus, these species are excellent molecules for constraining their initial ice abundances.

3. For many species in the model, such as CH_3OH, H_2CO, and HNCO, while the post-sputtering gas-phase abundances are equivalent to pre-sputtering ice abundances, the change is not as rapid as for the previous group and the gas-phase enhancement of the molecules begins prior to the majority of the non-thermal desorption brought on by the sputtering. This can be due to either the species efficiently sputtering off before the peak sputtering velocities or additional induced reactions by the increased mobility on the grain and additional enhancements of related species. Observationally, this would mean that the shock-enhanced abundances would correspond to times earlier than when it is seen for the previously mentioned class of molecules.

4. Finally, some molecules have gas-phase significant enhancements on top of the sputtering that produce abundances far larger than the pre-sputtering peak solid-phase abundances. Some of these species tend to be the same species that, during the pre-sputtering peak dust heating, would have ice enhancements without the corresponding gas-phase bump (e.g. OCN and CH_3CHO) or were secondary products from the enhancements of other species (e.g. H_2CCO). Many of these species are enhanced by the initial liberations into the gas-phase of species typically locked in the ice or the slightly-heated gas temperatures.

The major relic of this phase is clearly the desorption of essentially the entire ice surface and mantle into the gas phase. While some species lift into the gas-phase without addi-

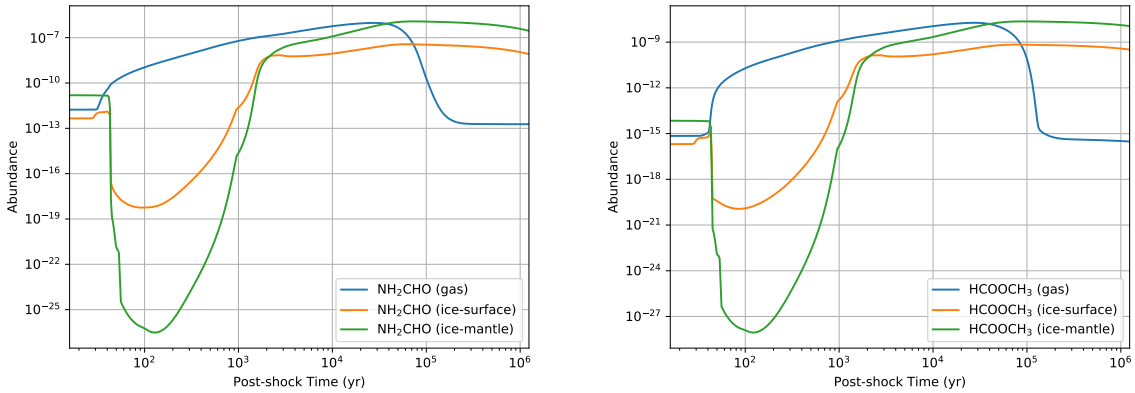

(c) NH_2CHO (d) $HCOOCH_3$

Figure 6.6: Simulated three-phase abundances of studied species over the time period in which the shock passes through in the model (i.e. $t_{\text{postshock}}$=0 corresponds to t_{total}=10^6 years) for species that display continuous gas-phase enhancement through post-shock chemistry.

tional simultaneous chemical processing, some species are significantly enhanced with the introduction of newly, abundant gas-phase species. From these findings, it is clear that this non-thermal desorption is both highly efficient and produces a unique chemical make up of the gas in the shock relative to other forms of desorption. Furthermore, for a shock velocity of $\sim$20 km s^{-1}, this phase would hypothetically occur over roughly at $\sim$500 AU physical scale. And, for nearby molecular outflows such as L1157, $\sim$250 pc away(142), this interior structure within the bow shock would be potentially resolvable with an observation with better than 2″ resolution, which is easily achievable with modern interferometers.

Hot Gas Phase Chemistry ($\sim$200-3$\times10^3$ years)

Here, with the ice-surface and mantle now residing in the gas-phase, the gas temperature reaches its peak temperature. With the chemically-enriched gas in a heated environment, new chemistry can proceed that would have been highly inefficient. Due to the extremely low abundances of solid-phase species, the overall profiles of the non-gas-phase abundances will not be discussed here in detail. In general, for a given species the gas-phase abundances will display one of the following trends:

1. For some, no appreciable change in the gas-phase abundance occurs in the high temperature regime. Many of the species that were significantly enhanced by the sputtering in the previous regime, such as CO, H_2O, and NH_3, maintain a stable gas-phase abundance such that there are no significant additional production. This is also true for species that experienced additional enhancements during the peak sputtering, such as SO and SO_2. In particular, HNCO does not see any significant post-shock

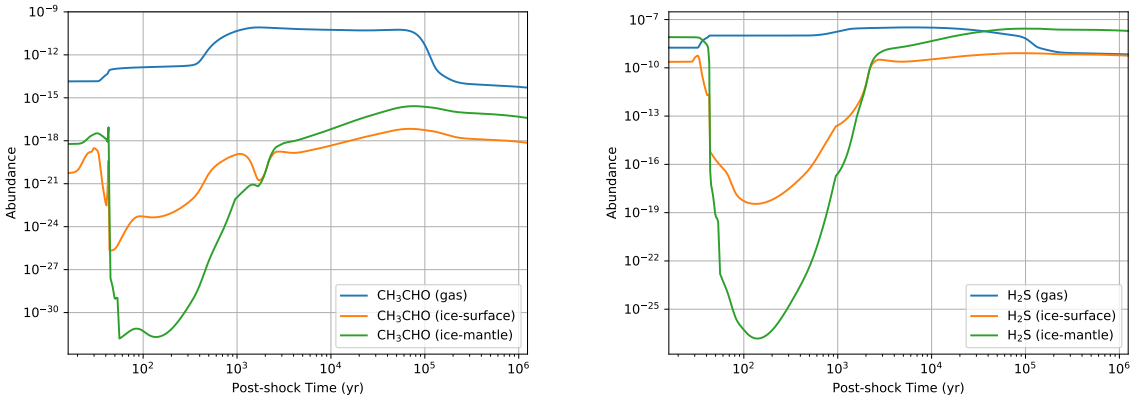

(a) CH_3CHO (b) H_2S

Figure 6.7: Simulated three-phase abundances of studied species over the time period in which the shock passes through in the model (i.e. $t_{\text{postshock}}$=0 corresponds to t_{total}=10^6 years) for species that display discrete gas-phase enhancement through post-shock chemistry.

gas-phase enhancements in this regime, which may be due to inefficiencies in the ice-chemistry of the model and will be discussed in a later section.

2. Other gas-phase abundances are enhanced during the high-temperature regime for species. For some, like NH_2CHO, CH_3CHO, and $HCOOCH_3$, this is due to an increase of its precursor species due to the sputtering in the previous phase and certain reactions with large barriers or strong temperature-dependencies now being accessible. For others, this enhancement is due to the dissociation of other, more complex species, such as OH from the processing of recently enhanced H_2CO.

3. The gas-phase abundances were also depleted for some species, including OH, CN, and OCN. For these, the post-shock chemistry that is enhancing other species is likely depleting these species that were predominantly in the ice prior to this.

In the shocked outflow L1157, we are able to sample different age shocks by comparing B1 and B2, which differ by about 2×10^3 years (86). Thus, the comparison between these two shocks should probe the hot-gas phase of our shock chemistry model. This will be discussed in detail in Section 6.4.1.

Redeposition Phase ($\sim3\times10^3$-10^5 years)

Here, the drift velocity and temperatures have fallen back down to the initial pre-shock conditions. Also at this point, the density has finally reached its final value, which is roughly a factor of 5 larger than the pre-shock conditions. Also, the reservoir of molecules

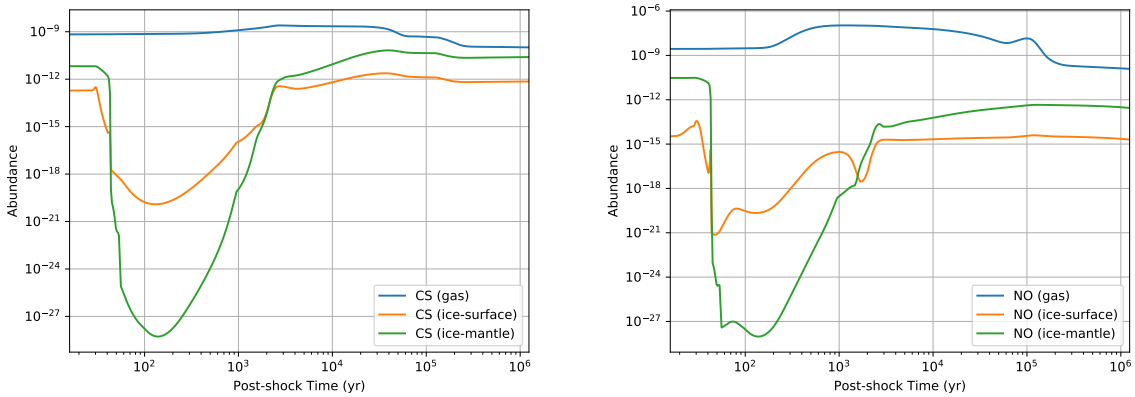

(a) CS (b) NO

Figure 6.8: Simulated three-phase abundances of studied species over the time period in which the shock passes through in the model (i.e. $t_{\text{postshock}}$=0 corresponds to t_{total}=10^6 years) for species that display reasonably-strong gas-phase enhancements during the post-shock phase.

on the ice can return to roughly what it was in the initial cold core phase. While the abundances on the grain did increase in the previous regime, it is likely due to the reduction of drift velocity, and thus the repressing sputtering rather than adsorption. Here, we see:

1. Many species have the ice abundances surpass the gas-phase abundances. In addition, over the time-scale in which the ice abundance became larger the gas-phase abundance varied. In many cases, the majority of the gas-phase population is redeposited onto the ice with little additional processing, such as with CH_3OH, NH_3, and H_2O, and occurred very close to 10^4 years after the shock. Other species, such as HNCO and NH_2CHO, undergo additional gas-phase enhancements, as their precursors have not yet undergone dissociation or adsorption. As such, the ice-abundances of these species tend to not surpass the gas-phase until closer to 5×10^4 years. For many of these species, the ice abundance is either comparable (e.g. H_2O and NH_3) or greater than the values prior to the shock (e.g. NH_2CHO, CH_3CHO, and $HCOOCH_3$).

2. Other species, such as OH, OCN and SO_2, also had their solid-phase abundances significantly enhanced, but not enough to become close to the gas-phase abundances. Many of these species were predominantly gas-phase species in the preshock conditions. And, as such, it is to be expected that the gas-phase reactions would come to dominate again. Meanwhile, some molecules such as SO were found to have comparable ice and gas-phase abundances, again due to significant gas-phase production routes in addition to the redeposition.

Overall, essentially every species had significant rebuilding of the ice mantle. However, the timescale in which species fall back onto the grain was found to vary from species to

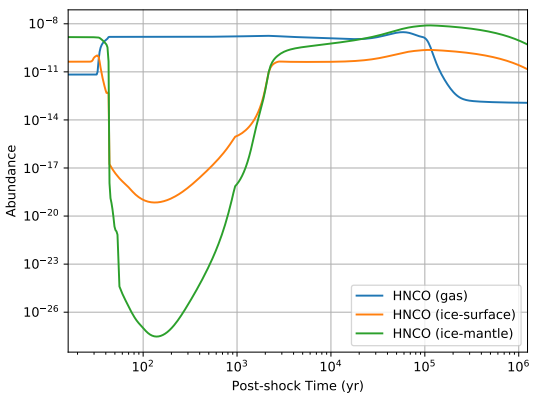

(a) HNCO

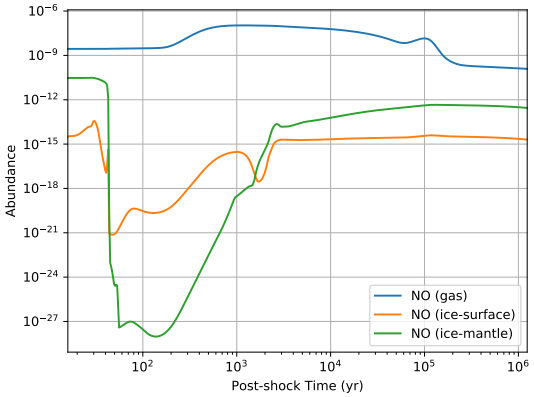

(b) CH_3COCH_3

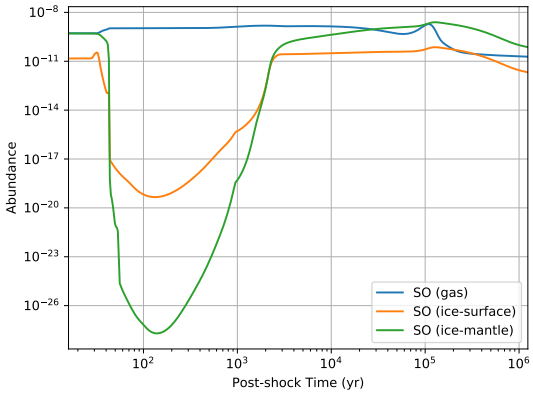

(c) SO

Figure 6.9: Simulated three-phase abundances of studied species over the time period in which the shock passes through in the model for species that display enhancements during the sputtering, hot gas, and redeposition regimes.

species, which could be possible to observationally probe for additional post-shock enhancement. While the species with earlier redeposition times and no additional gas-phase production in this regime were found to have comparable ice abundances prior to the peak sputtering, many of the other species had the ice abundances resulting being strongly enhanced (e.g. $HCOOCH_3$ and NH_2CHO). As will be discussed in Section 6.4.2, this shock-enhancement of the ice may prove to a useful probe for studying the physical and chemical history of these sources.

Post-shock Dense Gas Phase ($\sim 10^5$+ years)

Beyond 10^5 years, the physical conditions do not change over time and represent the effects on the chemistry long after the shock has passed. Excluding the change in density and

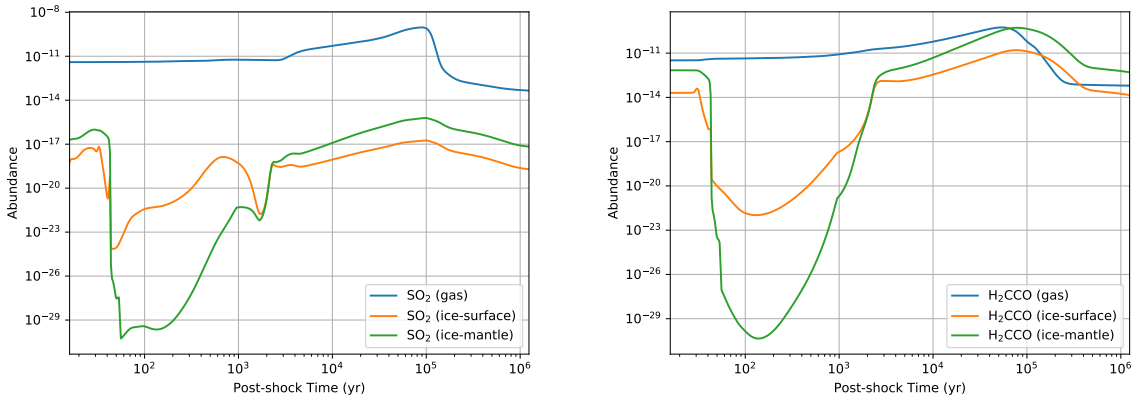

(a) SO_2 (b) H_2CCO

Figure 6.10: Simulated three-phase abundances of studied species over the time period in which the shock passes through in the model (i.e. $t_{\text{postshock}}$=0 corresponds to $t_{\text{total}}=10^6$ years) for species that display strong gas-phase enhancements during the redeposition phase.

extinction, the physical conditions are consistent with the pre-shock conditions. As such, we should be able to determine whether any changes from prior conditions are due to this change in physical conditions or the after-effects of the shock.

1. Many species, at this point, have reached a stable abundance for both the gas phase and ice mantle. This includes the abundant gas-phase species (e.g. CO and HCN) as well as the main constituents of the ice (e.g. H_2O and NH_3). As would be expected, the abundance trends discussed in the previous for these species remain consistent.

2. For many of the most complex species, such as $HCOOCH_3$ and CH_3CHO, the ice abundances decrease due to the cold grain's lack of efficient formation mechanisms, as was seen in the pre-shock conditions. This can also been seen by the increase in ice abundance of CH_3OH and HCOOH. Meanwhile, the gas-phase species also decrease due to processing and additional redeposition, but eventually stabilize at an abundance that can be maintained by the gas-phase production routes the species may have.

3. Finally, for species such as OCN and many of the sulfur-bearing species, both the gas-phase and ice abundances drop like the previous group of molecules. But, because these lighter species are less reliant on the accelerated diffusion on warm grains to form, they eventually stabilize to a final abundance like the first group.

Here, we can see for many of the species that had significant ice-phase enhancements in the first regime of the model, there exists a temporary surge in ice-chemistry that lasts for a few times 10^4 years, which is longer than many of the gas-phase enhancements commonly seen in these shocks. For a select number of species, their ice-abundances are permanently

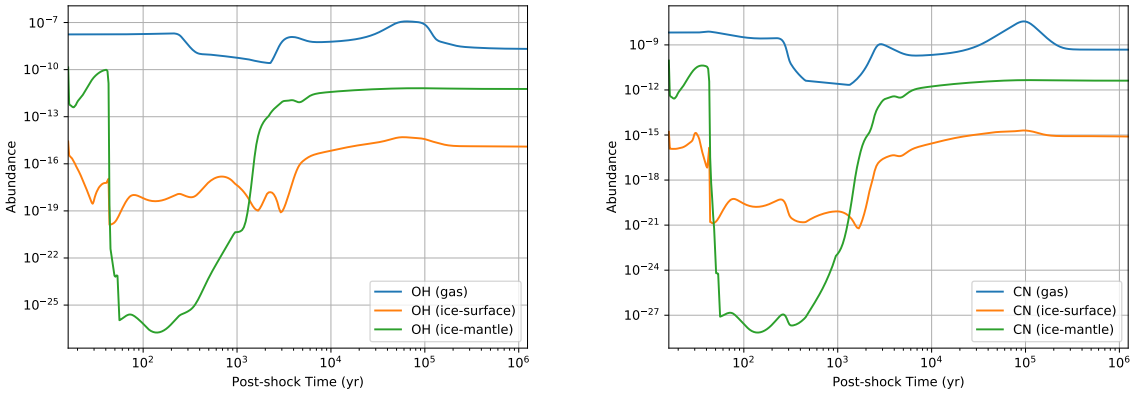

(a) OH (b) CN

Figure 6.11: Simulated three-phase abundances of studied species over the time period in which the shock passes through in the model (i.e. $t_{\text{postshock}}$=0 corresponds to t_{total}=10^6 years) for species with significant gas-phase depletion during the hot-gas regime.

enhanced, which appear to generally be the species that underwent significant post-shock chemistry, like CH_3CHO and NH_2CHO or species that were already highly abundant in the ice, but increased in abundance at the end of the model, such as CH_3OH, CH_3OCH_3, and HCOOH. More generally, the entire post-shock regime may be characterized by having ices that have a higher ratio of complex organics relative to H_2O.

Overall Species Classification

In addition, we found that certain cluster of species tended to, generally, proceed similar within the shock, even if they are not directly chemically related. Many species tended to follow the general bulk motion of the ice and did not display any significant post-shock gas-phase chemistry, including CO, H_2O, NH_3, H_2CO, CH_3OH, HCN, HCOOH, and CH_3OCH_3. On the other hand, many species did, in fact, display additional enhancements in the gas-phase during the shock events, and many had similar profiles. CH_3CHO and H_2S showed two discrete phases of enhancements, while $HCOOCH_3$ and NH_2CHO showed strong, continual enhancements from the start of sputtering to redeposition. CS and NO both saw reasonable enhancements in the post-shock phase. For SO_2 and H_2CCO, the abundances were relatively stable until they were enhanced in the redeposition phase. Gas-phase species that tended to be highly reactive, such as OH, CN, and OCN, saw significant changes overtime, especially characterized by a drop in abundance during the hot gas regime. Finally, HNCO, CH_3COCH_3, and SO were found to show very slight enhancements in the gas-phase due to post-shock chemistry, but were both strongly enhanced during the sputtering and redeposition regimes. As all these species will be enhanced at different discrete stages in the model, these enhancements should be theoretically repro-

ducible by comparing similar-velocity shocks of different ages or the internal structure of single bow shocks.

6.4 Discussion

6.4.1 Time-Sensitive Tracers and Testing Shock-Chemistry Predictions

In Burkhardt et al. (33), several predictions were made on the nature of the chemistry within L1157 and molecular outflows. Here, we will discuss these predictions, and a few other predictions, in the context of the results presented here.

CH_3OH

Methanol has long been used as a classical indicator of "complex" chemistry, as the six-member species is thought to be efficiently formed on the ice through successive hydrogenation of the highly abundant CO (103). As such, for the purposes of studying the chemistry in shocks, CH_3OH can be a useful species to study the lifting of the ice into the gas-phase. Through deep CARMA observations of L1157, Burkhardt et al. (33) found that the consistent abundance enhancement throughout the shock event of CH_3OH indicates that its primary source is from the liberation of grains during the shock.

Similarly, we see that the strongest source of enhancement of gas-phase CH_3OH is, in fact, the sputtering event with no other significant gas-phase enhancements. On the order of 10^3's of years after the shock, as probed by the two shock fronts in L1157, the abundance falls off rather smoothly in a relatively log-linear nature between the peak sputtering and the hot gas phase. And so, on the timescales discussed, it would appear to be a proper tracer to compare the relative shock-enhancements. From the analysis of the full network, other species that may also serve as good tracers of overall shock enhancements are additional complex species like H_2CO, HCOOH, and CH_3OCH_3, and the major constituent species, such as CO, H_2O, NH_3, as these species display similar falloff profiles and are all species that should fairly exclusively be produced on the grain in terms of post-shock enhancements.

While we refrain from discussing species abundances in this model due to the lack of strong constraints on the ice-chemistry, it should be noted that the peak phase abundance of CH_3OH is in agreement with what is typically seen in astrophysical shocks (10^{-6}) (33; 159).

HNCO

Due to the substantial abundance enhancements of HNCO in the L1157 bow shocks, especially comparing the B1 shock front to the older B2 shock front (Δt $\sim$2000 years), it has been proposed that HNCO may be enhanced by post-shock gas-phase chemistry in addition to the initial release from sputtering (33; 196). Specifically, HNCO was seen to have

a factor of two enhancement in the abundance over this time scale. At 2×10^3 years after the shock (i.e. during the hot-gas regime), by comparing the abundances between the beginning of this phase ($\sim$200 years) and at the peak ($\sim2.1\times10^3$ years), one can see that this enhancement is only $\sim$20%. While we do not reproduce this peak, it is likely due to the fact that the dominant reactions to produce HNCO in this phase require CH_2 or OCN, both of which were depleted prior to the peak of HNCO.

6.4.2 Other useful shock-probes

Through observations of the internal structure of the B1 shock front, Codella et al. (46, 47) probed the shock-chemistry of HDCO, CH_3CHO, and NH_2CHO by studying the morphology of the enhanced abundances within a single bow-shock, suggesting that the abundance of shock-tracers may be segmented by different phases of chemistry. While HDCO was found to be primarily enhanced at the very head of the bow shock, NH_2CHO and CH_3CHO peaked at a location slightly behind the shock front that suggested that their shock-enhancements were temporally delayed relative to the initial shock event (i.e. post-shock, gas-phase chemistry). Here, we see that the distribution of CH_3CHO, NH_2CHO, and additionally $HCOOCH_3$, are continually enhanced in the shock through gas-phase reactions. Here, NH_2CHO and $HCOOCH_3$ additionally show enhancements due to the sputtering event, but additional gas-phase processes are clearly efficient simultaneously to the sputtering around 100 years after the shock begins. As such, it would a useful test to see if $HCOOCH_3$ or its isomers display any similar distributions to that of NH_2CHO and CH_3CHO.

As discussed before, the redeposition phase of the species also may prove to be a useful indicator of post-shock chemistry as well. Because many of the ice-tracing species were found to redeposit faster than the species with post-shock enhancements by several 10^4 years, assuming a conservative shock velocity of 20 km s^{-1}, this timescale could be easily resolvable in astrophysical sources out to 40 kpc away with an observatory capable of only 1″ resolution.

Furthermore, the shock-induced enhancement of the ice abundances, both permanent (e.g. CH_3OH, H_2CO, and HCOOH) and temporary (e.g. NH_2CHO and HNCO) could prove to be very useful to provide evidence for prior shock events in a given source. With the upcoming launch of the James Webb Space Telescope (127), infrared absorption observations of ice features may be capable of differentiating between the shock-enhanced ices and ices with a relatively quiescent history. Because these ice enhancements remain far longer than the gas-phase enhancements and after the shock as passed, this could also provide evidence for the frequency in which shocks occur in the interstellar medium and whether a star forming region was triggered by shocks or general gravitational collapse.

6.4.3 Application for Protoplanetary Disks

In protoplanetary disks, the drift velocities observed in shocks tend to be lower than in molecular outflows (115). Thus, sputtering may not be as efficient as a source for non-thermally desorbing grain species in these regions. However, as we showed, additional ice chemistry can be induced through shocks by the heating of the dust grains, thus increasing thermal diffusive chemistry, with some fraction of the products of these exothermic reactions undergoing reactive desorption.

6.4.4 Comparison of Initial Ice Abundances to Literature

In contrast to many chemical models used to study shocks, we explicitly compute the build up of ice based on the current knowledge of solid-phase chemical networks instead of assuming an initial ice abundance. A thorough analysis of the build of this ice in dark cloud conditions using the NAUTILUS code was previously discussed in Ruaud et al. (199). A detailed study of the effects this pre-shock ice abundance has on the post-shock chemistry is to soon follow (Burkhardt et al. *in Prep*).

6.4.5 Future Directions

Many of the shock-induced enhancements can be observationally tested through interferometric or infrared ice absorption techniques. As such, dedicated studies to gather a rigorous sample of shock conditions and ages would allow this model to be fully constrained and improved.

In addition, more robust treatments of several processes could be relatively easily implemented to expand the power of the model's predictions. This includes the dust grain itself as a fourth chemical phase to be eroded during high-velocity shocks, which allow us to also consider the effect shock-chemistry has on the prototypical shock tracer, SiO (90). Also, we can include a more robust treatment of the dust size distribution and how that is impacted by the shock and the erosion of the ice mantle. The sputtering yields for many of these species have yet to be definitely and robustly studied. And, additional experimental and robust molecular dynamics calculations would provide greater insights into the underlying ice chemistry. Furthermore, high temperature chemistry can be included, including chemisorption on bare grains and additional hot gas-phase reactions with barriers, to better study the effects of the post-shock gas-phase chemistry.

Cosmic ray chemistry has also been found to be highly efficient at enhancing the chemistry in dark clouds (204). The inclusion of these processes may more accurately reproduce observed ice abundances in our pre-shock ice build up. Furthermore, the abundance of cosmic rays within astrophysical shocks will likely also impact the abundances of many species, both with inducing additional chemistry and through cosmic ray sputtering.

6.5 Conclusion

To conclude, through inclusion of sputtering, shock-physics parameters, high temperature reactions, and shock-induced dust heating into the three-phase gas-grain chemical network code NAUTILUS, we are able to reproduce many of the predictions made by Burkhardt et al. (33) (i.e. Chapter 5). In general, we find that some species will uniquely trace the overall motion of the ice in general and have minimal post-shock gas-phase chemistry. Others, display significant enhancements between the regimes of peak sputtering, hot gas-phase, and the redeposition onto the ice. And still other species already exist in the gas, but interactions with the shocks can impact their temporal abundance evolution. From this, we discuss how methanol, among other studied species, can serve to be a useful probe of the underlying ice chemistry. In addition, the temporary gas-phase enhancements can be easily tested observationally by modern observatories at the necessary angular resolution to correspond to the timescales discussed here. Finally, we find that the ice abundance can become permanently altered long after the shock, which may be possible to observe with the James Webb Space Telescope.

6.6 Acknowledgments

A.M.B. is a Grote Reber Fellow, and support for this work was provided by the NSF through the Grote Reber Fellowship Program administered by Associated Universities, Inc./National Radio Astronomy Observatory and the Virginia Space Grant Consortium.

Part IV

Conclusions

CHAPTER 7

CONCLUSIONS

WE have investigated two isolated astrophysical sources in order to constrain the chemistry that feeds into the later stages of star formation. Specifically, we studied how gas-phase chemistry can lead to the build up of large carbon-dominated chemistry through a deep spectral survey of TMC-1 with the GBT. In addition, we studied how shock chemistry can be used as a probe to the relatively unconstrained reservoir of molecules frozen on interstellar dust grains through interferometric observations and detailed gas-grain chemical modeling.

7.1 Chapter Two

We report the new detections of DC_7N, six of the seven ^{13}C-bearing isotopologues of HC_7N, and $HC_5{}^{15}N$ toward TMC-1 with a deep set of observations with the GBT. Through the determination of the column densities for each of isotopomer, we were able to compare the isotopic ratios for across the different cyanopolyynes. From this, we determine that:

- We do not observe any significant $^{12}C/^{13}C$ depletion for the N-adjacent carbon position among the isotopomers of both HC_5N and HC_7N, implying that CN may not be the primary precursor for their interstellar production.
- Through a comparison of overall isotopologue ratios, we found that while the values still agree within our uncertainties, HC_5N is found to have systematically less rare isotopes relative to HC_3N and HC_7N. Given the agreement between both the ^{13}C and ^{15}N isotopic ratios of HC_3N and HC_7N, it would appear that the primary precursor to cyanopolyynes may not be the next-smallest molecule in the family, $HC_{n-2}N$
- From this, we suggest the only remaining significant formation route for the larger cyanopolyynes is hydrocarbon neutrals and ions reactions with nitrogen ions and atoms.

.

7.2 Chapter Three

In this chapter, we report the discovery of benzonitrile (c-C_6H_5CN), the first aromatic molecule discovered using radio astronomy and rotational spectroscopy, toward the dark

cloud TMC-1. This detection was further enhanced through new, more accurate laboratory measurements of the rotational spectra of benzonitrile, including the resolution of the hyperfine splitting. Through the addition of several new relevant reactions into the gas-grain chemical network code NAUTILUS, we are able to reproduce the observed abundance of this molecule, along with the related cyanopolyyne family. This detection of benzonitrile in TMC-1 opens the door to the radioastronomical study of an important class of molecules. These species may be either direct contributors to the long-mysterious UIR bands or the immediate precursors to the carriers themselves. The distinct chemical environment of cold cores, and their relatively simple and homogeneous physical conditions, makes these sources ideal for exploring the chemical formation and destruction mechanisms that are operative there.

7.3 Chapter Four

Next, we discuss the detection of a new molecular family through the discovery of the HC_5O radical through four well-resolved hyperfine components a deep spectral survey of the dark cloud, TMC-1 performed with the Green Bank Telescope. A search for other HC_nO radicals ($n = 3 - 7$) resulted in mostly non-detections, with a tentative detection of HC_7O discussed. Through the use of the gas-grain chemical network code NAUTILUS, we are able to reproduce column densities that are consistent with the observed column density of HC_5O and with the upper limits inferred for HC_3O, HC_6O, and HC_7O. HC_4O, however, is significantly over-produced in the model, likely indicating that additional reaction pathways not considered here contribute significantly to that chemistry. This chemistry is found to vary significantly from the log-linear abundance versus molecule size trend observed in the analogous cyanopolyyne family.

7.4 Chapter Five

Here, we present the new CARMA interferometric maps of CH_3OH, HCN, HCO^+, and HNCO emission toward the southern, blue-shifted shocked outflow of L1157. We use the non-LTE code RADEX to compute the column densities and relative enhancements of these shock-relevant molecules. From this, we find:

- CH_3OH abundance enhancement is relatively consistent across the various clumps in the shocked outflow. From this, we conclude that this enhancement is primarily produced by the shock causing significant sputtering of the ice.
- The velocity profiles of the pairs HCN/HCO^+ and CH_3OH/HNCO suggest that they may originate from the similar physical regions.
- The east/west chemical differentiation observed in B0 and B1 could be explained by the recent history of each sides of the lobe. While the east side is shocking into cold,

dense, and quiescent material, the west side may be interacting with warm, diffuse, and previously-shocked material, as evidenced by the the abundance enhancements and high-velocity spectral components

- Through the first interferometric maps of HNCO, enhanced abundances are seen toward B2 relative to B1, which may be explained by post-shock gas-phase chemistry.

7.5 Chapter Six

Finally, we incorporate several shock-relevant physical and chemical processes into the gas-grain chemical network code NAUTILUS, including sputtering, temporal evolution of the physical conditions typical of shocks, high temperature reactions, and shock-induced dust heating. From this, we are able to reproduce many of the predictions in the previous chapter. In general, we find that:

- Some species will have minimal post-shock gas-phase chemistry (e.g. CH_3OH), implying they strongly follow the bulk motion of the ice. These species may be useful for constraining the abundances and trends in solid-phase interstellar chemistry through observations of these species in shocks.

- Others molecules, instead, undergo significant enhancements between the regimes of peak sputtering, hot gas-phase, and the redeposition onto the ice. The timescales over which these enhancements may occur should be possible to observationally test through comparisons of sources of different shock ages or the internal structure of individual bow shocks.

- There exist additional species that already exist in the gas, but interactions with the shocks can impact their temporal abundance evolution, which still may provide additional time-dependent probes.

- Finally, we find that the ice abundance can become permanently altered long after the shock, which may be possible to observe through infrared ice absorption with the James Webb Space Telescope.

7.6 Summary of Major Conclusions

From this work, we can conclude that this method is indeed possible and insightful towards understanding the formation of the complex chemistry seen in the hot core phase and beyond. As we continually improve our ability to probe the most complex sources with the tools of astrochemistry, it is crucial that we continue to refine and improve the foundation in which the complex chemistry observed is built on. As such, further spectral and interferometric surveys of, as well as refinement of astrochemical models for, the types

of sources of studied here will continue to supply substantial benefits to the greater field of astrochemistry.

Bibliography

[mcg]

[Sci] Materials and methods are available as supplementary materials on *Science* Online.

[1] Abplanalp, M. J.; Gozem, S.; Krylov, A. I.; Shingledecker, C. N.; Herbst, E.; Kaiser, R. I. *Proceedings of the National Academy of Sciences* **2016**, *113*, 7727–7732.

[2] Adams, N. G.; Smith, D.; Giles, K.; Herbst, E. *Astronomy & Astrophysics* **1989**, *220*, 269–271.

[3] Akabane, K.; Morimoto, M.; Kaifu, N.; Ishiguro, M. *Sky and Telescope* **1983**, *66*.

[4] Altwegg, K. et al. *Science Advances* **2016**, *2*, e1600285.

[5] Aota, T.; Inoue, T.; Aikawa, Y. *ApJ* **2015**, *799*, 141.

[6] Araki, M.; Takano, S.; Sakai, N.; Yamamoto, S.; Oyama, T.; Kuze, N.; Tsukiyama, K. *Astrophysical Journal* **2016**, *833*, 291.

[7] Arce, H. G.; Santiago-García, J.; Jørgensen, J. K.; Tafalla, M.; Bachiller, R. *The Astrophysical Journal Letters* **2008**, *681*, L21–L24.

[8] Bachiller, R.; Gutiérrez, M. P. *The Astrophysical Journal Letters* **1997**, *487*, L93.

[9] Bachiller, R.; Pérez Gutiérrez, M.; Kumar, M. S. N.; Tafalla, M. *A&A* **2001**, *372*, 899–912.

[10] Balle, T. J.; Flygare, W. H. *Review of Scientific Instruments* **1981**, *52*, 33–45.

[11] Bell, M. B.; Feldman, P. A.; Travers, M. J.; McCarthy, M. C.; Gottlieb, C. A.; Thaddeus, P. *The Astrophysical Journal Letters* **1997**, *483*, L61.

[12] Bell, M. B.; Avery, L. W.; MacLeod, J. M.; Matthews, H. E. *Astrophysical Journal* **1992**, *400*, 551–555.

[13] Belloche, A.; Müller, H. S. P.; Garrod, R. T.; Menten, K. M. *Astronomy & Astrophysics* **2016**, *587*, A91–66.

[14] Benedettini, M.; Busquet, G.; Lefloch, B.; Codella, C.; Cabrit, S.; Ceccarelli, C.; Giannini, T.; Nisini, B.; Vasta, M.; Cernicharo, J.; Lorenzani, A.; di Giorgio, A. M.; the CHESS team, *A&A* **2012**, *539*, L3.

[15] Benedettini, M.; Viti, S.; Codella, C.; Bachiller, R.; Gueth, F.; Beltrán, M. T.; Dutrey, A.; Guilloteau, S. *MNRAS* **2007**, *381*, 1127–1136.

[16] Benedettini, M.; Viti, S.; Codella, C.; Gueth, F.; Gómez-Ruiz, A. I.; Bachiller, R.; Beltrán, M. T.; Busquet, G.; Ceccarelli, C.; Lefloch, B. *MNRAS* **2013**, *436*, 179–190.

[17] Benson, P. J.; Myers, P. C. *Astrophysical Journal, Supplement* **1989**, *71*, 89–108.

[18] Bergin, E. A. Astrobiology: An astronomer's perspective. American Institute of Physics Conference Series. 2014; pp 5–34.

[19] Bergin, E. A.; Melnick, G. J.; Neufeld, D. A. *ApJ* **1998**, *499*, 777–792.

[20] Bergin, E. A. et al. *Astronomy and Astrophysics* **2010**, *521*, L20.

[21] Bergin, E. A.; Tafalla, M. *Annual Review of Astron and Astrophys* **2007**, *45*, 339–396.

[22] Bergner, J. B.; Ãberg, K. I.; Rajappan, M. *The Astrophysical Journal* **2017**, *845*, 29.

[23] Berné, O.; Montillaud, J.; Joblin, C. *Astronomy & Astrophysics* **2015**, *577*, A133–9.

[24] Bizzocchi, L.; Degli Esposti, C.; Botschwina, P. *Journal of Molecular Spectroscopy* **2004**, *225*, 145–151.

[25] Boersma, C.; Bauschlicher Jr., C. W.; Ricca, A.; Mattioda, A. L.; Cami, J.; Peeters, E.; de Armas, F. S.; Saborido, G. P.; Hudgins, D. M.; Allamandola, L. J. *Astrophysical Journal Supplement Series* **2014**, *211*, 8–12.

[26] Bolatto, A. D.; Wolfire, M.; Leroy, A. K. *Annual Review of Astronomy and Astrophysics* **2013**, *51*, 207–268.

[27] Boogert, A. C. A.; Gerakines, P. A.; Whittet, D. C. B. *Annual Review of Astronomy and Astrophysics* **2015**, *53*, 541–581.

[28] Botschwina, P.; Horn, M.; Markey, K.; Oswald, R. *Molecular Physics* **1997**, *92*, 381–392.

[29] Broten, N. W.; Oka, T.; Avery, L. W.; MacLeod, J. M.; Kroto, H. W. *Astrophysical Journal, Letters* **1978**, *223*, L105–L107.

[30] Brown, R. D.; Dyall, K. G.; Elmes, P. S.; Godfrey, P. D.; McNaughton, D. *Journal of the American Chemical Society* **1988**, *110*, 789–792.

[31] Bujarrabal, V.; Guelin, M.; Morris, M.; Thaddeus, P. *Astronomy and Astrophysics* **1981**, *99*, 239–247.

[32] Burkhardt, A. M.; Herbst, E.; Kalenskii, S. V.; McCarthy, M. C.; Remijan, A. J.; McGuire, B. A. *Monthly Notices of the RAS* **2018**, *474*, 5068–5075.

[33] Burkhardt, A. M.; Dollhopf, N. M.; Corby, J. F.; Carroll, P. B.; Shingledecker, C. N.; Loomis, R. A.; Booth, S. T.; Blake, G. A.; Herbst, E.; Remijan, A. J.; McGuire, B. A. *Astrophysical Journal* **2016**, *827*, 21.

[34] Busquet, G.; Lefloch, B.; Benedettini, M.; Ceccarelli, C.; Codella, C.; Cabrit, S.; Nisini, B.; Viti, S.; Gómez-Ruiz, A. I.; Gusdorf, A.; di Giorgio, A. M.; Wiesenfeld, L. *Astronomy and Astrophysics* **2014**, *561*, A120.

[35] Campbell, E. K.; Holz, M.; Gerlich, D.; Maier, J. P. *Nature* **2015**, *523*, 322–323.

[36] Caselli, P.; Hartquist, T. W.; Havnes, O. *Astronomy and Astrophysics* **1997**, *322*, 296–301.

[37] Cernicharo, J.; Heras, A. M.; Tielens, A. G. G. M.; Pardo, J. R.; Herpin, F.; Guélin, M.; Waters, L. B. F. M. *Astrophysical Journal, Letters* **2001**, *546*, L123–L126.

[38] Charnley, S. B.; Kress, M. E.; Tielens, A. G. G. M.; Millar, T. J. *Astrophysical Journal v.448* **1995**, *448*, 232–239.

[39] Charnley, S. B.; Markwick, A. J. *Astronomy and Astrophysics* **2003**, *399*, 583–587.

[40] Chen, W.; Novick, S. E.; McCarthy, M. C. *The Astrophysical Journal* **1996**, *462*, 561.

[41] Chenu, J.-Y.; Navarrini, A.; Bortolotti, Y.; Butin, G.; Fontana, A. L.; Mahieu, S.; Maier, D.; Mattiocco, F.; Serres, P.; Berton, M.; Garnier, O.; Moutote, Q.; Parioleau, M.; Pissard, B.; Reverdy, J. *IEEE Transactions on Terahertz Science and Technology* **2016**, *6*, 223–237.

[42] Cheung, A. C.; Rank, D. M.; Townes, C. H.; Thornton, D. D.; Welch, W. J. *Physical Review Letters* **1968**, *21*, 1701–1705.

[43] Cheung, A. C.; Rank, D. M.; Townes, C. H.; Thornton, D. D.; Welch, W. J. *Nature* **1969**, *221*, 626–628.

[44] Chiar, J. E.; Tielens, A. G. G. M.; Adamson, A. J.; Ricca, A. *The Astrophysical Journal* **2013**, *770*, 78–13.

[45] Choi, M.; Panis, J.-F.; Evans, I., Neal J. *The Astrophysical Journal Supplement Series* **1999**, *122*, 519–556.

[46] Codella, C. et al. *Astronomy & Astrophysics* **2017**, *605*, L3–7.

[47] Codella, C.; Fontani, F.; Ceccarelli, C.; Podio, L.; Viti, S.; Bachiller, R.; Benedettini, M.; Lefloch, B. *Monthly Notices of the Royal Astronomical Society: Letters* **2015**, *449*, L11–L15.

[48] Codella, C.; Benedettini, M.; Beltrán, M. T.; Gueth, F.; Viti, S.; Bachiller, R.; Tafalla, M.; Cabrit, S.; Fuente, A.; Lefloch, B. *Astronomy and Astrophysics* **2009**, *507*, L25–L28.

[49] Codella, C. et al. *A&A* **2017**, *605*, L3.

[50] Cooksy, A. L.; Tao, F. M.; Klemperer, W. *The Journal of Physical Chemistry* **1995**, *99*, 11095–11100.

[51] Cooksy, A. L.; Watson, J. K. G.; Gottlieb, C. A.; Thaddeus, P. *Journal of Molecular Spectroscopy* **1992**, *153*, 610–626.

[52] Corby, J. F.; Jones, P. A.; Cunningham, M. R.; Menten, K. M.; Belloche, A.; Schwab, F. R.; Walsh, A. J.; Balnozan, E.; Bronfman, L.; Lo, N.; Remijan, A. J. *Monthly Notices of the Royal Astronomical Society* **2015**, *452*, 3969–3993.

[53] Crockett, N. R.; Bergin, E. A.; Neill, J. L.; Black, J. H.; Blake, G. A.; Kleshcheva, M. *The Astrophysical Journal* **2014**, *781*, 114.

[54] Crutcher, R. M.; Churchwell, E.; Ziurys, L. M. *The Astrophysical Journal* **1984**, *283*, 668.

[55] Császár, A. G.; Fogarasi, G. *Spectrochimica Acta A* **1989**, *45*, 845–854.

[56] Cuppen, H. M.; Herbst, E. *The Astrophysical Journal* **2007**, *668*, 294.

[57] Cuppen, H. M.; Walsh, C.; Lamberts, T.; Semenov, D.; Garrod, R. T.; Penteado, E. M.; Ioppolo, S. *Space Science Reviews* **2017**,

[58] Cyburt, R. H.; Fields, B. D.; Olive, K. A.; Yeh, T.-H. *Reviews of Modern Physics* **2016**, *88*, 015004.

[59] Draine, B. T. *The Astrophysical Journal* **2016**, *831*, 1–19.

[60] Draine, B. T. *Astrophysical Journal* **1980**, *241*, 1021–1038.

[61] Draine, B. T. *Physics of the Interstellar and Intergalactic Medium by Bruce T. Draine. Princeton University Press, 2011. ISBN: 978-0-691-12214-4*; 2011.

[62] Draine, B. T.; Lee, H. M. *Astrophysical Journal* **1984**, *285*, 89–108.

[63] Draine, B. T.; McKee, C. F. *Annual Review of Astron and Astrophys* **1993**, *31*, 373–432.

[64] Draine, B. T.; Salpeter, E. E. *Astrophysical Journal* **1979**, *231*, 77–94.

[65] Dunham, T., Jr. *Publications of the Astronomical Society of the Pacific* **1937**, *49*, 26–28.

[66] Dzyurkevich, N.; Commerçon, B.; Lesaffre, P.; Semenov, D. *Astronomy and Astrophysics* **2017**, *603*, A105.

[67] Ehrenfreund, P.; Charnley, S. B. *Annual Review of Astron and Astrophys* **2000**, *38*, 427–483.

[68] Engel, M. H.; Macko, S. A.; Silfer, J. A. *Nature* **1990**, *348*, 47.

[69] Field, F. H. *The Journal of Physical Chemistry* **1964**, *68*, 1039–1047.

[70] Flower, D. R.; Pineau des Forêts, G. *Monthly Notices of the RAS* **2003**, *343*, 390–400.

[71] Fontani, F.; Codella, C.; Ceccarelli, C.; Lefloch, B.; Viti, S.; Benedettini, M. *Astrophysical Journal* **2014**, *788*, L43.

[72] Fukuzawa, K.; Osamura, Y.; Schaefer, H. F., III *Astrophysical Journal* **1998**, *505*, 278–285.

[73] García-Hernández, D. A.; García-Lario, P.; Cernicharo, J.; Engels, D.; Perea-Calderón, J. V. *Journal of Physics Conference Series* **2016**, *728*, 052003.

[74] Garozzo, M.; Fulvio, D.; Kanuchova, Z.; Palumbo, M. E.; Strazzulla, G. *Astronomy and Astrophysics* **2010**, *509*, A67.

[75] Garrod, R. T.; Herbst, E. *Astronomy and Astrophysics* **2006**, *457*, 927–936.

[76] Garrod, R. T.; Wakelam, V.; Herbst, E. *Astronomy and Astrophysics* **2007**, *467*, 1103–1115.

[77] Garrod, R. T. *The Astrophysical Journal* **2013**, *765*, 60.

[78] Garrod, R. T.; Weaver, S. L. W.; Herbst, E. *The Astrophysical Journal* **2008**, *682*, 283.

[79] Garrod, R. T.; Widicus Weaver, S. L. *Chemical Reviews* **2013**, *113*, 8939–8960.

[80] Georgievskii, Y.; A.Â Miller, J.; J.Â Klippenstein, S. *Physical Chemistry Chemical Physics* **2007**, *9*, 4259–4268.

[81] Gordy, W.; Cook, R. L. *Microwave Molecular Spectra*, 3rd ed.; Wiley: New York, 1984.

[82] Graedel, T. E.; Langer, W. D.; Frerking, M. A. *The Astrophysical Journal Supplement Series* **1982**, *48*, 321–368.

[83] Gratier, P.; Majumdar, L.; Ohishi, M.; Roueff, E.; Loison, J. C.; Hickson, K. M.; Wakelam, V. *The Astrophysical Journal Supplement Series* **2016**, *225*, 1–10.

[84] Green, J.; Harrison, D. J. *Spectrochimica Acta A* **1976**, *32*, 1279–1286.

[85] Greve, A.; Bremer, M.; Penalver, J.; Raffin, P.; Morris, D. *IEEE Transactions on Antennas and Propagation* **2005**, *53*, 851–860.

[86] Gueth, F.; Guilloteau, S.; Bachiller, R. *Astronomy and . . .* **1996**,

[87] Gueth, F.; Guilloteau, S.; Bachiller, R. *Astronomy and Astrophysics* **1998**, *333*, 287–297.

[88] Gueth, F.; Guilloteau, S.; Dutrey, A.; Bachiller, R. *Astronomy and Astrophysics* **1997**, *323*, 943–952.

[89] Guilloteau, S. et al. *Astronomy and Astrophysics* **1992**, *262*, 624–633.

[90] Gusdorf, A.; Cabrit, S.; Flower, D. R.; Pineau des Forêts, G. *Astronomy & Astrophysics* **2008**, *482*, 809–829.

[91] Gusdorf, A.; Pineau des Forêts, G.; Cabrit, S.; Flower, D. R. *Astronomy & Astrophysics* **2008**, *490*, 695–706.

[92] Gusdorf, A.; Riquelme, D.; Anderl, S.; Eislöffel, J.; Codella, C.; Gómez-Ruiz, A. I.; Graf, U. U.; Kristensen, L. E.; Leurini, S.; Parise, B.; Requena-Torres, M. A.; Ricken, O.; Güsten, R. *Astronomy & Astrophysics* **2015**, *575*, A98–14.

[93] Guzman-Ramirez, L.; Zijlstra, A. A.; Níchuimín, R.; Gesicki, K.; Lagadec, E.; Millar, T. J.; Woods, P. M. *Monthly Notices of the RAS* **2011**, *414*, 1667–1678.

[94] Gómez-Ruiz, A. I.; Hirano, N.; Leurini, S.; Liu, S.-Y. *Astronomy & Astrophysics* **2013**, *558*, A94–10.

[95] Harada, N.; Herbst, E.; Wakelam, V. *Astrophysical Journal* **2010**, *721*, 1570–1578.

[96] Hasegawa, T. I.; Herbst, E.; Leung, C. M. *Astrophysical Journal, Supplement* **1992**, *82*, 167–195.

[97] Herbst, E. *Astrophysical Journal, Supplement* **1983**, *53*, 41–53.

[98] Herbst, E.; Millar, T. In *The chemistry of cold interstellar cloud cores, in low temperatures and cold molecules*; Smith, I. W. M., Ed.; Imperial College Press: London, England, 2008.

[99] Herbst, E.; van Dishoeck, E. F. *Annual Review of Astronomy and Astrophysics* **2009**, *47*, 427–480.

[100] Herbst, E.; Adams, N. G.; Smith, D. *Astrophysical Journal* **1984**, *285*, 618–621.

[101] Herbst, E.; Leung, C. M. *Astronomy and Astrophysics* **1990**, *233*, 177–180.

[102] Herbst, E.; Klemperer, W. *The Astrophysical Journal* **1973**, *185*, 505.

[103] Herbst, E.; Millar, T. J. In *Low Temperatures and Cold Molecules*; Smith, I. W. M., Ed.; Imperial College Press: London, 2008.

[104] Herbst, E.; van Dishoeck, E. F. *Annual Reviews of Astronomy and Astrophysics* **2009**, *47*, 427–480.

[105] Hily-Blant, P.; Bonal, L.; Faure, A.; Quirico, E. *Icarus* **2013**, *223*, 582–590.

[106] Hincelin, U.; Wakelam, V.; Hersant, F.; Guilloteau, S.; Loison, J. C.; Honvault, P.; Troe, J. *Astronomy & Astrophysics* **2011**, *530*, A61–6.

[107] Hincelin, U.; Chang, Q.; Herbst, E. *Astronomy & Astrophysics* **2015**, *574*, A24.

[108] Hincelin, U.; Wakelam, V.; CommerÃğon, B.; Hersant, F.; Guilloteau, S. *The Astrophysical Journal* **2013**, *775*, 44.

[109] Hincelin, U.; Wakelam, V.; Hersant, F.; Guilloteau, S.; Loison, J. C.; Honvault, P.; Troe, J. *Astronomy & Astrophysics* **2011**, *530*, A61.

[110] Hollis, J. M.; Jewell, P. R.; Lovas, F. J.; Remijan, A. *The Astrophysical Journal* **2004**, *613*, L45–L48.

[111] Howe, D. A.; Millar, T. J.; Schilke, P.; Walmsley, C. M. *Monthly Notices of the RAS* **1994**, *267*, 59.

[112] Hudgins, D. M.; Bauschlicher Jr., C. W. *The Astrophysical Journal* **2005**, *632*, 316–332.

[113] Huntress, W. T., Jr. *Astrophysical Journal, Supplement* **1977**, *33*, 495–514.

[114] Ikeda, M.; Hirota, T.; Yamamoto, S. *Astrophysical Journal* **2002**, *575*, 250–256.

[115] Ilee, J. D.; Forgan, D. H.; Evans, M. G.; Hall, C.; Booth, R.; Clarke, C. J.; Rice, W. K. M.; Boley, A. C.; Caselli, P.; Hartquist, T. W.; Rawlings, J. M. C. *Monthly Notices of the RAS* **2017**, *472*, 189–204.

[116] Irvine, W. M.; Hoglund, B.; Friberg, P.; Askne, J.; Ellder, J. *Astrophysical Journal, Letters* **1981**, *248*, L113–L117.

[117] Jiménez-Serra, I.; Caselli, P.; Martín-Pintado, J.; Hartquist, T. W. *A&A* **2008**, *482*, 549–559.

[118] Jochims, H. W.; Baumgartel, H.; Leach, S. *The Astrophysical Journal* **1999**, *512*, 500–510.

[119] Jones, B. M.; Zhang, F.; Kaiser, R. I.; Jamal, A.; Mebel, A. M.; Cordiner, M. A.; Charnley, S. B. *Proceedings of the National Academy of Sciences* **2011**, *108*, 452–457.

[120] Jørgensen, J. K. et al. *Astronomy & Astrophysics* **2016**, *595*, A117.

[121] Kaifu, N.; Ohishi, M.; Kawaguchi, K.; Saito, S.; Yamamoto, S.; Miyaji, T.; Miyazawa, K.; Ishikawa, S.-I.; Noumaru, C.; Harasawa, S. *Publications of the Astronomical Society of Japan* **2004**, *56*, 69–173.

[122] Kaiser, R. I.; Parker, D. S. N.; Mebel, A. M. *Annual Review of Physical Chemistry* **2015**, *66*, 43–67.

[123] Kaiser, R. I. *Chemical Reviews* **2002**, *102*, 1309–1358.

[124] Kalenskii, S. V.; Johansson, L. E. B. *Astronomy Reports* **2010**, *54*, 295–316.

[125] Kalenskii, S. V. *ArXiv e-prints* **2017**,

[126] Kaufman, M. J.; Neufeld, D. A. *Astrophysical Journal* **1996**, *456*, 250.

[127] Kirkpatrick, A.; Alberts, S.; Pope, A.; Barro, G.; Bonato, M.; Kocevski, D. D.; Perez-Gonzalez, P.; Rieke, G. H.; Rodriguez-Munoz, L.; Sajina, A.; Grogin, N. A.; Mantha, K. B.; Pandya, V.; Pforr, J.; Santini, P. *ArXiv e-prints* **2017**,

[128] Kitamura, Y. *Icarus* **1986**, *66*, 241–257.

[129] Knight, J. S.; Freeman, C. G.; McEwan, M. J.; Smith, S. C.; Adams, N. G. *Monthly Notices of the RAS* **1986**, *219*, 89–94.

[130] Kofman, V.; Sarre, P. J.; Hibbins, R. E.; ten Kate, I. L.; Linnartz, H. *Molecular Astrophysics* **2017**, *7*, 19–26.

[131] Kohguchi, H.; Ohshima, Y.; Endo, Y. *The Journal of Chemical Physics* **1994**, *101*, 6463–6469.

[132] Kraemer, K. E.; Sloan, G. C.; Bernard-Salas, J.; Price, S. D.; Egan, M. P.; Wood, P. R. *The Astrophysical Journal* **2006**, *652*, L25–L28.

[133] Kwon, W.; Fernández-López, M.; Stephens, I. W.; Looney, L. W. *ApJ* **2015**, *814*, 43.

[134] Landau, L. D.; Lifshitz, E. M. *Course of theoretical physics, Oxford: Pergamon Press, 1959*; 1959.

[135] Langston, G.; Turner, B. *Astrophysical Journal* **2007**, *658*, 455–461.

[136] Lefloch, B.; Cabrit, S.; Busquet, G.; Codella, C.; Ceccarelli, C.; Cernicharo, J.; Pardo, J. R.; Benedettini, M.; Lis, D. C.; Nisini, B. *The Astrophysical Journal* **2012**, *757*, L25–5.

[137] Lefloch, B.; Ceccarelli, C.; Codella, C. *arxiv.v* **2017**, 1–5.

[138] Lefloch, B.; Ceccarelli, C.; Codella, C.; Favre, C.; Podio, L.; Vastel, C.; Viti, S.; Bachiller, R. *MNRAS* **2017**, *469*, L73–L77.

[139] Lesaffre, P.; Pineau des Forêts, G.; Godard, B.; Guillard, P.; Boulanger, F.; Falgarone, E. *Astronomy and Astrophysics* **2013**, *550*, A106.

[140] Loomis, R. A.; McGuire, B. A.; Shingledecker, C.; Johnson, C. H.; Blair, S.; Robertson, A.; Remijan, A. J. *The Astrophysical Journal* **2015**, *799*, 34–8.

[141] Loomis, R. A.; Shingledecker, C. N.; Langston, G.; McGuire, B. A.; Dollhopf, N. M.; Burkhardt, A. M.; Corby, J.; Booth, S. T.; Carroll, P. B.; Turner, B.; Remijan, A. J. *Monthly Notices of the Royal Astronomical Society* **2016**, *463*, 4175–4183.

[142] Looney, L. W.; Tobin, J. J.; Kwon, W. *ApJL* **2007**, *670*, L131–L134.

[143] Lovas, F. J.; McMahon, R. J.; Grabow, J.-U.; Schnell, M.; Mack, J.; Scott, L. T.; Kuczkowski, R. L. *Journal of the American Chemical Society* **2005**, *127*, 4345–4349.

[144] Low, F. J.; Young, E.; Beintema, D. A.; Gautier, T. N.; Beichman, C. A.; Aumann, H. H.; Gillett, F. C.; Neugebauer, G.; Boggess, N.; Emerson, J. P. *Astrophysical Journal* **1984**, *278*, L19–L22.

[145] MacLeod, J. M.; Avery, L. W.; Broten, N. W. *Astrophysical Journal, Letters* **1981**, *251*, L33–L36.

[146] Majumdar, L.; Gratier, P.; Ruaud, M.; Wakelam, V.; Vastel, C.; Sipilä, O.; Hersant, F.; Dutrey, A.; Guilloteau, S. *Monthly Notices of the Royal Astronomical Society* **2016**, *466*, 4470.

[147] Majumdar, L.; Gratier, P.; Ruaud, M.; Wakelam, V.; Vastel, C.; Sipilä, O.; Hersant, F.; Dutrey, A.; Guilloteau, S. *Monthly Notices of the RAS* **2017**, *466*, 4470–4479.

[148] Malek, S. E.; Cami, J.; Bernard-Salas, J. *The Astrophysical Journal* **2011**, *744*, 16–8.

[149] Mangum, J. G.; Shirley, Y. L. *Publications of the Astronomical Society of the Pacific* **2015**, *127*, 266–298.

[150] Marty, B.; Chaussidon, M.; Wiens, R. C.; Jurewicz, A. J. G.; Burnett, D. S. *Science* **2011**, *332*, 1533.

[151] Mauersberger, R.; Henkel, C.; Sage, L. J. *Astronomy and Astrophysics* **1990**, *236*, 63–68.

[152] McCarthy, M. C.; Gottlieb, C. A.; Gupta, H.; Thaddeus, P. *The Astrophysical Journal* **2006**, *652*, L141.

[153] McCarthy, M. C.; Levine, E. S.; Apponi, A. J.; Thaddeus, P. *Journal of Molecular Spectroscopy* **2000**, *203*, 75–81.

[154] McCarthy, M. C.; Travers, M. J.; Kovács, A.; Gottlieb, C. A.; Thaddeus, P. *The Astrophysical Journal Supplement Series* **1997**, *113*, 105.

[155] McElroy, D.; Walsh, C.; Markwick, A. J.; Cordiner, M. A.; Smith, K.; Millar, T. J. *Astronomy and Astrophysics* **2013**, *550*, A36.

[156] McEwan, M. J.; Scott, G. B. I.; Adams, N. G.; Babcock, L. M.; Terzieva, R.; Herbst, E. *The Astrophysical Journal* **1999**, *513*, 287–293.

[157] McGuire, B. A.; Burkhardt, A. M.; Shingledecker, C. N.; Kalenskii, S. V.; Herbst, E.; Remijan, A. J.; McCarthy, M. C. *Astrophysical Journal, Letters* **2017**, *843*, L28.

[158] McGuire, B. A.; Carroll, P. B. *Physics Today* **2016**, *69*, 86–87.

[159] McGuire, B. A.; Carroll, P. B.; Dollhopf, N. M.; Crockett, N. R.; Corby, J. F.; Loomis, R. A.; Burkhardt, A. M.; Shingledecker, C.; Blake, G. A.; Remijan, A. J. *The Astrophysical Journal* **2015**, *812*, 1–9.

[160] McGuire, B. A.; Carroll, P. B.; Loomis, R. A.; Finneran, I. A.; Jewell, P. R.; Remijan, A. J.; Blake, G. A. *Science* **2016**, *352*, 1449–1452.

[161] McGuire, B. A.; Burkhardt, A. M.; Kalenskii, S.; Shingledecker, C. N.; Remijan, A. J.; Herbst, E.; McCarthy, M. C. *Science* **2018**, *359*, 202–205.

[162] McKee, C. F.; Ostriker, E. C. *Annual Review of Astron and Astrophys* **2007**, *45*, 565–687.

[163] McKellar, A. *Publications of the Astronomical Society of the Pacific* **1940**, *52*, 187.

[164] Meibom, A.; Krot, A. N.; Robert, F.; Mostefaoui, S.; Russell, S. S.; Petaev, M. I.; Gounelle, M. *Astrophysical Journal, Letters* **2007**, *656*, L33–L36.

[165] Mendoza, E.; Lefloch, B.; Lopez-Sepulcre, A.; Ceccarelli, C.; Codella, C.; Boechat-Roberty, H. M.; Bachiller, R. *Monthly Notices of the Royal Astronomical Society* **2014**, *445*, 151–161.

[166] Milam, S. N.; Savage, C.; Brewster, M. A.; Ziurys, L. M.; Wyckoff, S. *Astrophysical Journal* **2005**, *634*, 1126–1132.

[167] Miller, R. E. **1998**, *3271*, 151.

[168] Miura, H.; Yamamoto, T.; Nomura, H.; Nakamoto, T.; Tanaka, K. K.; Tanaka, H.; Nagasawa, M. *ApJ* **2017**, *839*, 47.

[169] Mohamed, S.; McCarthy, M. C.; Cooksy, A. L.; Hinton, C.; Thaddeus, P. *The Journal of Chemical Physics* **2005**, *123*, 234301–9.

[170] Morgan, M.; White, S.; Lockman, J.; Bryerton, E.; Saini, K.; Norrod, R.; Simon, B.; Srikanth, S.; Anderson, G.; Pisano, D. A K-band spectroscopic focal plane array for the Robert C. Byrd Green Bank radio telescope. Union Radio Scientifique Internationale XXIX General Assembly, 7-16 August 2008, Chicago, USA, id. J02p1. 2008; p J02p1.

[171] Mullins, A. M.; Loughnane, R. M.; Redman, M. P.; Wiles, B.; Guegan, N.; Barrett, J.; Keto, E. R. *Monthly Notices of the RAS* **2016**, *459*, 2882–2892.

[172] Müller, H. S. P.; Schlöder, F.; Stutzki, J.; Winnewisser, G. *Journal of Molecular Structure* **2005**, *742*, 215–227.

[173] Neill, J. L. et al. *The Astrophysical Journal* **2014**, *789*, 8.

[174] Neill, J. L.; Harris, B. J.; Steber, A. L.; Douglass, K. O.; Plusquellic, D. F.; Pate, B. H. *Opt. Express* **2013**, *21*, 19743.

[175] Ohishi, M.; Kaifu, N. *Faraday Discussions* **1998**, *109*, 205.

[176] Palumbo, M. E. *The Journal of Physical Chemistry A* **1997**, *101*, 4298–4301.

[177] Perley, R. A.; Chandler, C. J.; Butler, B. J.; Wrobel, J. M. *Astrophysical Journal, Letters* **2011**, *739*, L1.

[178] Pickett, H. M.; Poynter, R. L.; Cohen, E. A.; Delitsky, M. L.; Pearson, J. C.; Muller, H. *Journal of Quantitative Spectroscopy and Radiative Transfer* **1998**, *60*, 883–890.

[179] Pickles, J. B.; Williams, D. A. *Astrophysics and Space Science* **1977**, *52*, 443–452.

[180] Pilleri, P.; Herberth, D.; Giesen, T. F.; Gerin, M.; Joblin, C.; Mulas, G.; Malloci, G.; Grabow, J. U.; Brünken, S.; Surin, L.; Steinberg, B. D.; Curtis, K. R.; Scott, L. T. *Monthly Notices of the Royal Astronomical Society* **2009**, *397*, 1053–1060.

[181] Prestage, R. M.; Constantikes, K. T.; Hunter, T. R.; King, L. J.; Lacasse, R. J.; Lockman, F. J.; Norrod, R. D. *IEEE Proceedings* **2009**, *97*, 1382–1390.

[182] Probstein, R. F.; Shorenstein, M. L. *AIAA Journal* **1968**, *6*, 1898–1906.

[183] Qi, C.; Öberg, K. I.; Wilner, D. J.; D'Alessio, P.; Bergin, E.; Andrews, S. M.; Blake, G. A.; Hogerheijde, M. R.; van Dishoeck, E. F. *Science* **2013**, *341*, 630–632.

[184] Quan, D.; Herbst, E.; Osamura, Y.; Roueff, E. *The Astrophysical Journal* **2010**, *725*, 2101–2109.

[185] Rawlings, J. M. C.; Redman, M. P.; Keto, E.; Williams, D. A. *Monthly Notices of the RAS* **2004**, *351*, 1054–1062.

[186] Rawlings, J. M. C.; Williams, D. A.; Viti, S.; Cecchi- Pestellini, C.; Duley, W. W. *Monthly Notices of the RAS* **2013**, *430*, 264–273.

[187] Regan, M. W. et al. *The Astrophysical Journal Supplement Series* **2004**, *154*, 204–210.

[188] Remijan, A. J.; Markwick-Kemper, A.; ALMA Working Group on Spectral Line Frequencies, Splatalogue: Database for Astronomical Spectroscopy. American Astronomical Society Meeting Abstracts. 2007; p #132.11.

[189] Remijan, A. J.; Hollis, J. M.; Snyder, L. E.; Jewell, P. R.; Lovas, F. J. *ApJL* **2006**, *643*, L37–L40.

[190] Remijan, A. J.; Wyrowski, F.; Friedel, D. N.; Meier, D. S.; Snyder, L. E. *Astrophysical Journal* **2005**, *626*, 233–244.

[191] Remijan, A. J.; Friedel, D. N.; de Pater, I.; Hogerheijde, M. R.; Snyder, L. E.; A'Hearn, M. F.; Blake, G. A.; Dickel, H. R.; Forster, J. R.; Kraybill, C.; Looney, L. W.; Palmer, P.; Wright, M. C. H. *The Astrophysical Journal* **2006**, *643*, 567–572.

[192] Requena-Torres, M. A.; Martin-Pintado, J.; Rodríguez-Franco, A.; Martín, S.; Rodríguez-Fernández, N. J.; De Vicente, P. *A&A* **2006**, *455*, 971–985.

[193] Ribeiro, F. d. A.; Almeida, G. C.; Garcia-Basabe, Y.; Wolff, W.; Boechat-Roberty, H. M.; Rocco, M. L. M. *Physical Chemistry Chemical Physics (Incorporating Faraday Transactions)* **2015**, *17*, 27473–27480.

[194] Riess, A. G. et al. *Astronomical Journal* **1998**, *116*, 1009–1038.

[195] Ritchey, A. M.; Federman, S. R.; Lambert, D. L. *Astrophysical Journal, Letters* **2015**, *804*, L3.

[196] Rodríguez-Fernández, N. J.; Tafalla, M.; Gueth, F.; Bachiller, R. *Astronomy & Astrophysics* **2010**, *516*, A98–8.

[197] Roshi, D. A. et al. *ArXiv e-prints* **2012**,

[198] Roueff, E.; Loison, J. C.; Hickson, K. M. *Astronomy and Astrophysics* **2015**, *576*, A99.

[199] Ruaud, M.; Wakelam, V.; Hersant, F. *Monthly Notices of the Royal Astronomical Society* **2016**, *459*, 3756–3767.

[200] Ruffle, D. P.; Herbst, E. *Monthly Notices of the Royal Astronomical Society* **2001**, *322*, 770–778.

[201] Sault, R. J.; Teuben, P. J.; Wright, M. C. H. A Retrospective View of MIRIAD. Astronomical Data Analysis Software and Systems IV, ASP Conference Series, Vol. 77, 1995, R.A. Shaw, H.E. Payne, and J.J.E. Hayes, eds., p. 433. 1995; p 433.

[202] Schiff, H. I.; Bohme, D. K. *Astrophysical Journal* **1979**, *232*, 740–746.

[203] Schloerb, F. P.; Snell, R. L.; Langer, W. D.; Young, J. S. *Astrophysical Journal, Letters* **1981**, *251*, L37–L41.

[204] Shingledecker, C. N.; Tennis, J. D.; Le Gal, R. *The Astrophysical Journal* **2018**,

[205] Shingledecker, C. N.; Herbst, E. *Physical Chemistry Chemical Physics* **2018**, *20*, 5359–5367.

[206] Snyder, L. E.; Hollis, J. M.; Jewell, P. R.; Lovas, F. J.; Remijan, A. *Astrophysical Journal* **2006**, *647*, 412–417.

[207] Snyder, L. E.; Buhl, D.; Zuckerman, B.; Palmer, P. *Physical Review Letters* **1969**, *22*, 679–681.

[208] Struve, O.; Emberson, R. M.; Findlay, J. W. *Publications of the ASP* **1960**, *72*, 439.

[209] Suutarinen, A. N.; Kristensen, L. E.; Mottram, J. C.; Fraser, H. J.; van Dishoeck, E. F. *Monthly Notices of the RAS* **2014**, *440*, 1844–1855.

[210] Swings, P.; Rosenfeld, L. *The Astrophysical Journal* **1937**, *86*, 483–486.

[211] Tafalla, M.; Santiago-García, J.; Hacar, A.; Bachiller, R. *Astronomy & Astrophysics* **2010**, *522*, A91–19.

[212] Tafalla, M.; Bachiller, R. *Astrophysical Journal* **1995**, *443*, L37.

[213] Takami, M.; Karr, J. L.; Koh, H.; Chen, H.-H.; Lee, H.-T. *Astrophysical Journal* **2010**, *720*, 155–172.

[214] Takano, S.; Masuda, A.; Hirahara, Y.; Suzuki, H.; Ohishi, M.; Ishikawa, S.-I.; Kaifu, N.; Kasai, Y.; Kawaguchi, K.; Wilson, T. L. *Astronomy and Astrophysics* **1998**, *329*, 1156–1169.

[215] Taniguchi, K.; Ozeki, H.; Saito, M. *Astrophysical Journal* **2017**, *846*, 46.

[216] Taniguchi, K.; Ozeki, H.; Saito, M.; Sakai, N.; Nakamura, F.; Kameno, S.; Takano, S.; Yamamoto, S. *Astrophysical Journal* **2016**, *817*, 147.

[217] Taniguchi, K.; Saito, M. *Publications of the ASJ* **2017**, *69*, L7.

[218] Taniguchi, K.; Saito, M.; Ozeki, H. *Astrophysical Journal* **2016**, *830*, 106.

[219] Thorwirth, S.; Theule, P.; Gottlieb, C. A.; McCarthy, M. C.; Thaddeus, P. *The Astrophysical Journal* **2007**, *662*, 1309–1314.

[220] Tielens, A. G. G. M. *Annual Review of Astronomy and Astrophysics* **2008**, *46*, 289–337.

[221] Tielens, A. G. G. M.; Hagen, W. *Astronomy and Astrophysics* **1982**, *114*, 245–260.

[222] Trevitt, A. J.; Goulay, F.; Taatjes, C. A.; Osborn, D. L.; Leone, S. R. *The Journal of Physical Chemistry A* **2010**, *114*, 1749–1755.

[223] Tsang, W. *Journal of Physical and Chemical Reference Data* **1992**, *21*, 753–791.

[224] Tsang, W.; Herron, J. T. *Journal of Physical and Chemical Reference Data* **1991**, *20*, 609–663.

[225] Turner, B. E. *Astrophysical Journal, Supplement* **2001**, *136*, 579–629.

[226] Ulich, B. L.; Haas, R. W. *Astrophysical Journal, Supplement* **1976**, *30*, 247–258.

[227] Van Loo, S.; Ashmore, I.; Caselli, P.; Falle, S. A. E. G.; Hartquist, T. W. *Monthly Notices of the RAS* **2013**, *428*, 381–388.

[228] Viti, S.; Collings, M. P.; Dever, J. W.; McCoustra, M. R. S.; Williams, D. A. *Monthly Notices of the Royal Astronomical Society* **2004**, *354*, 1141–1145.

[229] Wakelam, V.; Herbst, E. *The Astrophysical Journal* **2008**, *680*, 371–383.

[230] Wakelam, V. et al. *The Astrophysical Journal Supplement Series* **2012**, *199*, 21.

[231] Wakelam, V. et al. *The Astrophysical Journal Supplement Series* **2015**, *217*, 1–7.

[232] Walsh, C.; Millar, T. J.; Nomura, H.; Herbst, E.; Weaver, S. W.; Aikawa, Y.; Laas, J. C.; Vasyunin, A. I. *Astronomy & Astrophysics* **2014**, *563*, A33.

[233] Ward, P.; Brownlee, D. *Rare earth : why complex life is uncommon in the universe / Peter Ward, Donald Brownlee. New York : Copernicus, c2000.*; 2000.

[234] Watson, W. D.; Anicich, V. G.; Huntress, W. T., Jr. *Astrophysical Journal, Letters* **1976**, *205*, L165–L168.

[235] Wilson, R. W.; Jefferts, K. B.; Penzias, A. A. *The Astrophysical Journal Letters* **1970**, *161*, L43.

[236] Winnewisser, G.; Walmsley, C. M. *Astrophysics and Space Science* **1979**, *65*, 83–93.

[237] Wishart, J. F. In *Photochemistry and radiation chemistry*; Wishart, J. F., Nocera, D. G., Eds.; Advances in Chemistry Series 254; ACS Publications, 1998; pp 1–4.

[238] Wohlfart, K.; Schnell, M.; Grabow, J.-U.; Küpper, J. *Journal of Molecular Spectroscopy* **2008**, *247*, 119–121.

[239] Woon, D. E. *Chemical Physics* **2006**, *331*, 67–76.

[240] Woon, D. E.; Herbst, E. *Astrophysical Journal Supplement Series* **2009**, *185*, 273–288.

[241] Wootten, A.; Thompson, A. R. *IEEE Proceedings* **2009**, *97*, 1463–1471.

[242] Yamaguchi, T.; Takano, S.; Watanabe, Y.; Sakai, N.; Sakai, T.; Liu, S.-Y.; Su, Y.-N.; Hirano, N.; Takakuwa, S.; Aikawa, Y.; Nomura, H.; Yamamoto, S. *PASJ* **2012**, *64*, 105.

[243] Zhou, L.; Zheng, W.; Kaiser, R. I.; Landera, A.; Mebel, A. M.; Liang, M.-C.; Yung, Y. L. *The Astrophysical Journal* **2010**, *718*, 1243–1251.

[244] van der Tak, F. F. S.; Black, J. H.; Schöier, F. L.; Jansen, D. J.; van Dishoeck, E. F. *Astronomy & Astrophysics* **2007**, *468*, 627–635.

[245] Primiani, R. A.; Young, K. H.; Young, A.; Patel, N.; Wilson, R. W.; Vertatschitsch, L.; Chitwood, B. B.; Srinivasan, R.; MacMahon, D.; Weintroub, J. *Journal of Astronomical Instrumentation* **2016**, *5*, 1641006–810.

[246] Öberg, K. I.; Guzmán, V. V.; Furuya, K.; Qi, C.; Aikawa, Y.; Andrews, S. M.; Loomis, R.; Wilner, D. J. *Nature* **2015**, *520*, 198–201.